RELATIVISTIC VISCOUS HYDRODYNAMICS FOR NUCLEAR COLLISIONS AND APPLICATIONS TO THERMALIZING COLOR GLASS

A Dissertation

by

SIDHARTH SOMANATHAN

Submitted to the Office of Graduate and Professional Studies of
Texas A&M University
in partial fulfillment of the requirements for the degree of

DOCTOR OF PHILOSOPHY

Chair of Committee,	Rainer J. Fries
Committee Members,	Carl A. Gagliardi
	Joseph B. Natowitz
	Che-Ming Ko
Head of Department,	George R. Welch

August 2016

Major Subject: Physics

ABSTRACT

Heavy ion collisions such as those taking place at the Relativistic Heavy Ion Collider (RHIC) at Brookhaven National Laboratory and Large Hadron Collider (LHC) at CERN provide us with an opportunity to study dense and hot nuclear matter. This matter, called Quark Gluon Plasma (QGP), is believed to have existed in the early universe. Now we can create this material in heavy ion collisions and study its properties. There have been early theoretical arguments that collisions of nuclei at large energies can be described by relativistic hydrodynamics. The experimental heavy ion programs at RHIC and LHC have finally provided strong evidence that quark gluon plasma in those collisions indeed cools and expands hydrodynamically. In recent years precision hydrodynamic calculations have become tools that are also necessary ingredients for successful calculations of hard probes, heavy quarks, electromagnetic probes etc., in heavy ion collisions.

Here we develop, implement and test a viscous $3+1$ D hydrodynamic code. It contains both shear and bulk viscous corrections and is able to deal with shocks and steep gradients. In our approach we used finite volume schemes with a fifth order accuracy in space and up to third order in time. We benchmarked our code with several analytical tests which tested our code rigorously for accuracy in all the spatial and temporal directions. The shear viscous part of our code was also analytically compared with results from the evolution of Gubser initial conditions. We also conducted numerical tests for the accuracy of the implementation of bulk stress and a variety of standard tests including shock wave and fluctuating initial conditions.

We finally apply this code to initial conditions based on color glass condensate

(CGC) theory to trace key observables from very early times to freeze-out. Despite the high viscous corrections in our CGC initial conditions and its surprising similarity in structure to the Navier Stokes values (but with higher magnitudes in general), our code was able to run successfully for several impact parameters and we were able to extract key physical parameters of interest like energy momentum tensor and angular momentum. With this we intend to tune to data from RHIC and LHC.

To my mother,

for your love and unceasing support

and

in loving memory of my father.

ACKNOWLEDGEMENTS

First and foremost, I would like to thank my adviser Prof. Rainer Fries, without whose guidance and support I would not have been able to finish my doctorate. Dr. Fries has been of the utmost help - he has always been accessible and encouraged me to think in the right direction. Most of all, I am thankful to Dr. Fries for being an exceptionally kind adviser and individual during the arduous periods most graduate students face. I wish to express my gratitude to Prof. Carl Gagliardi, Prof. Che-Ming Ko and Prof. Joseph Natowitz for serving in my dissertation committee. I also wish to thank Dr. Jayan M. V., a professor at my undergraduate institution, for his encouragement when I was preparing for graduate education in physics.

There are many friends without whom life would have been dull during graduate school. But, most importantly, I am thankful for the friendship of Vishnu Venugopal. Without the technical insight and encouragement I received from discussions with him, it would have been extremely difficult to finish the degree. I am also very grateful to Vishnu's family (especially his Mother) with whom I stayed for the last seven months of my PhD career and they provided me an environment where I could focus on writing and finishing my thesis. I am grateful to my friend Joseph Cyrus for going out of the way and being a very kind help several times. I am thankful to Nithin Thomas for his friendship and the many hours we spent playing badminton and sharing our common interest in tennis. I also want to thank Dr. Guangyao Chen and Steven Rose for collaboration and discussions.

I would like to thank my immediate family: uncle Cdr. Venugopal, aunt Usha, and cousins Karthik and Vidya who are, in actuality, like siblings to me. Their good wishes and encouragement are invaluable to me. Several times throughout my

graduate career, my aunt and uncle, Surya and Vinith Poduval, welcomed me to their loving home for long relaxing breaks, and for that I am truly grateful to them.

Lastly, I am indebted to my mother and grandmother, whose unflagging love and support has always motivated me to do well in life. Their inner strength and tenacity in adverse circumstances continues to inspire me.

TABLE OF CONTENTS

Page

LIST OF FIGURES

FIGURE Page

LIST OF TABLES

TABLE Page

1. INTRODUCTION

1.1 Quantum Chromodynamics (QCD) and Quark Gluon Plasma (QGP)

The strong interaction of nuclear matter (quarks and gluons) is described by the theory of QCD. Quarks and gluons, as we witness in our every day life of low temperatures and density, only exist in bound states of hadrons (baryons and mesons). This is the color *confinement* property, which prevents quarks from being isolated individually.

If we try to separate a quark-antiquark pair, the interaction will get stronger as we get them further apart. A string tube of colored gluon fields form between the quarks. It breaks if pulled apart further and a new quark-antiquark pair is created from the vacuum.

Opposite to *confinement*, we have the property of *asymptotic freedom* [7, 8, 9] which says that the interaction between quarks decreases as energy increases or distance decreases. One interesting property that has been predicted, in light of *asymptotic freedom*, is that at very high temperatures and density it might be possible to have a de-confined state of quarks and gluons. For this we would need to bring together hadrons like protons and neutrons, at high density and very high temperature, until the strength of the strong interaction is reduced enough, for confinement to cease. Such a state has been called the Quark Gluon Plasma.

Asymptotic freedom implies, that a phase transition of color neutral hadrons to the deconfined plasma state of QGP is possible. But where or when could such a state of matter exist? It is believed that in the early universe and up to 10^{-4} seconds after the *Big Bang*, the universe was in a QGP state. It might also be found at the center of neutron and quark stars. The other scenario of producing QGP would

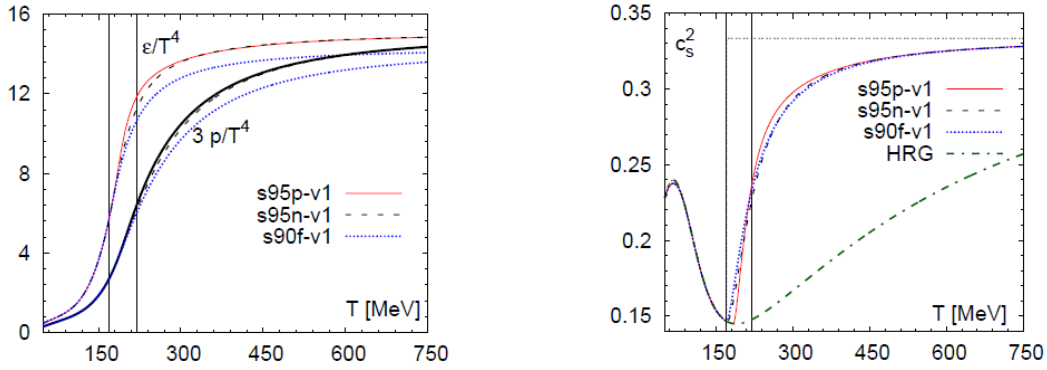

Figure 1.1: Lattice QCD plots of equation of state and speed of sound. **Left Panel:** Energy density ϵ/T^4 and $3P/T^4$ plotted with respect to temperature T. **Right Panel:** Speed of sound squared $c_s^2 = \partial P/\partial\epsilon$ plotted with respect to temperature T. In the QGP phase these curves are fits to lattice QCD results with various assumptions. Plots taken with permission from [1].

be to do our own *small-scale Big Bang*, achieved by colliding heavy nuclei, after accelerating them close to the speed of light. The STAR and PHENIX experiments at the Relativistic Heavy Ion Collider (RHIC) and the ALICE, CMS and ATLAS groups at the Large Hadron Collider (LHC), are exploring this latter option.

1.1.1 Equation of State

In the study of relativistic hydrodynamics of the QGP state, it is essential we know the equation of state. The equation must come from the underlying physics of nuclear matter which is the theory of QCD. In QGP state the strong interaction works over large distance, a regime where perturbative QCD fails to give analytical results.

The best theoretical approach to learn about the QCD phase transition is Lattice QCD where we computationally solve the equations on a finite space-time grid. Fig 1.1 shows the energy density ϵ scaled by T^4 vs temperature T from Lattice QCD [1]

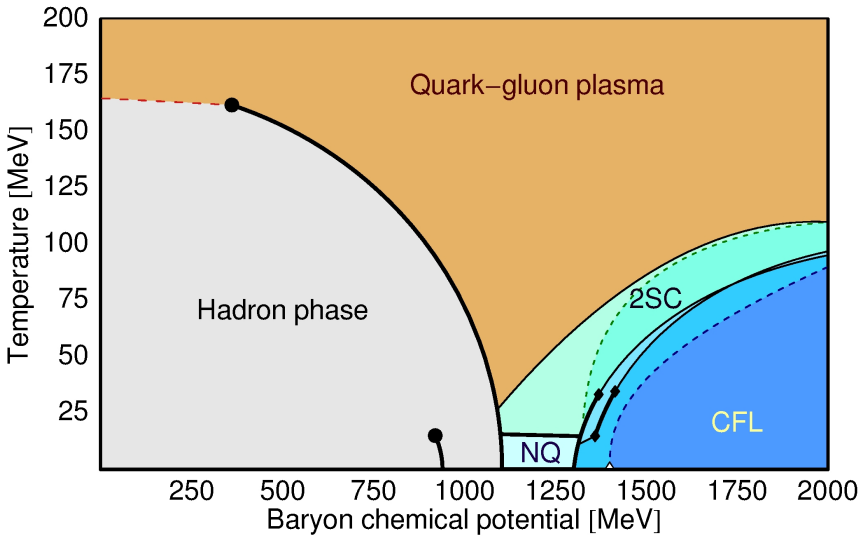

Figure 1.2: Conjectured QCD phase diagram. Plot taken with permission from [2].

results. Recall that for a free relativistic gas,

$$\epsilon = d \ \frac{3\pi^2}{90} \ T^4 \tag{1.1}$$

where d is the number of degrees of freedom. This is compatible with ϵ/T^4 at large T in Fig. 1.1 . We can see that between 150 and 200 MeV the number of degrees of freedom increases rather sharply. Even though it is not a sharp first-order transition, it is still indicative of a rapid crossover to the plasma state. Similarly, signatures of a crossover can also be seen from the speed of sound squared $c_s^2 = \partial P/\partial\epsilon$, (here P is the pressure) for the plot on right side in Fig. 1.1.

The schematic QCD phase diagram in Fig. 1.2 summarizes many of the properties of QCD. At low baryon densities the crossover from the hadron phase to the deconfined QGP phase is a smooth transition (dotted red line) as predicted by Lattice QCD. There are theoretical motivations and models which predict the existence of a critical point, beyond which, at higher baryon chemical potentials the phase

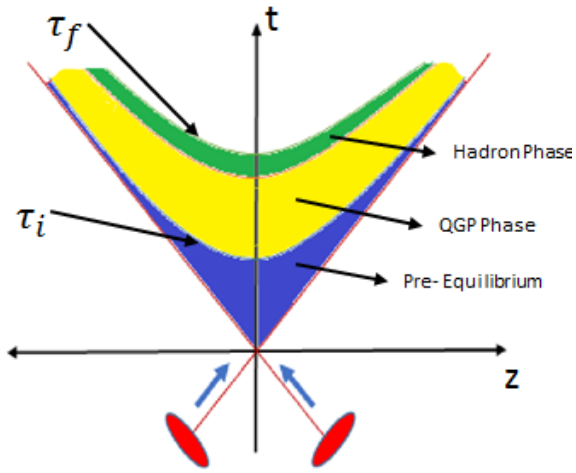

Figure 1.3: Time evolution of the nuclei with respect to z and t. The motion of the nuclei, almost along the light cone axes is visible.

transition should be of first order (bold black line). The experimental search for the critical point is actively being pursued [10, 11, 12]. At lower temperature and larger potentials exotic superconductor like phases of quark matter (Color-Flavor-Locked (CFL), Non-CFL (NQ) and the Two-Flavor Color Superconductor (2SC)) are also predicted [13, 14, 15].

1.2 Time Evolution of Heavy Ion Collisions (HIC)

Relativistic heavy ion collisions at RHIC located at Brookhaven National Labs (BNL), are being done at a center of mass energy up to $\sqrt{s_{NN}} = 200$ GeV per nucleon pair. More recently, heavy ion collisions at the Large Hadron Collider (LHC) ring at the European Organization for Nuclear Research (CERN) are capable of going as high as $\sqrt{s_{NN}} = 5.5$ TeV per nucleon pair. There is good evidence that the postulated QGP matter has been experimentally found at RHIC and LHC [16, 17, 18, 19, 20, 21, 22]

The various stages of a heavy ion collision are schematically given in Fig. 1.3.

The two heavy nuclei are moving along the Z-Axis in opposite directions and heading towards each other. Their motion is almost along the two light cone axes, because their speed is very close to c, the speed of light.

The collision takes place at $z = 0$ and $t = 0$. At RHIC the Lorentz factor γ is close to 100 and at LHC it is close to 3500. Such a high velocity causes Lorentz contraction by this factor γ and the nuclei appear as *thin pancakes* in the lab frame.

Immediately after the collision we have dense QCD matter which is not in equilibrium. These non-equilibrium processes are quite complex to understand. The Color Glass Condensate gives a good description of these initial stages which we will look into in Chapter 5 of this thesis.

Once near thermal equilibrium is achieved, then thermodynamic properties can be studied with the help of relativistic viscous hydrodynamics. In Fig. 1.3 this happens at proper time τ_i. Hydrodynamics is a universal description of the long wavelength limit of any system close enough to thermal equilibrium and in our time evolution it makes for a good model between τ_i and a freeze-out time τ_f. In between these times the QCD matter undergoes the phase transition and we again reach a stage were the entire matter is made up of hadrons which interact and are in thermal equilibrium with each other. Shortly after that the chemical freeze out occurs, which freezes the number of species of each kind of hadron. Even after the chemical freeze-out of hadrons, thermal equilibrium remains and hydrodynamics is still considered a valid description maybe with chemical potentials until thermal freeze-out happens at proper time τ_f. After thermal freeze-out the free streaming hadrons head towards the detectors.

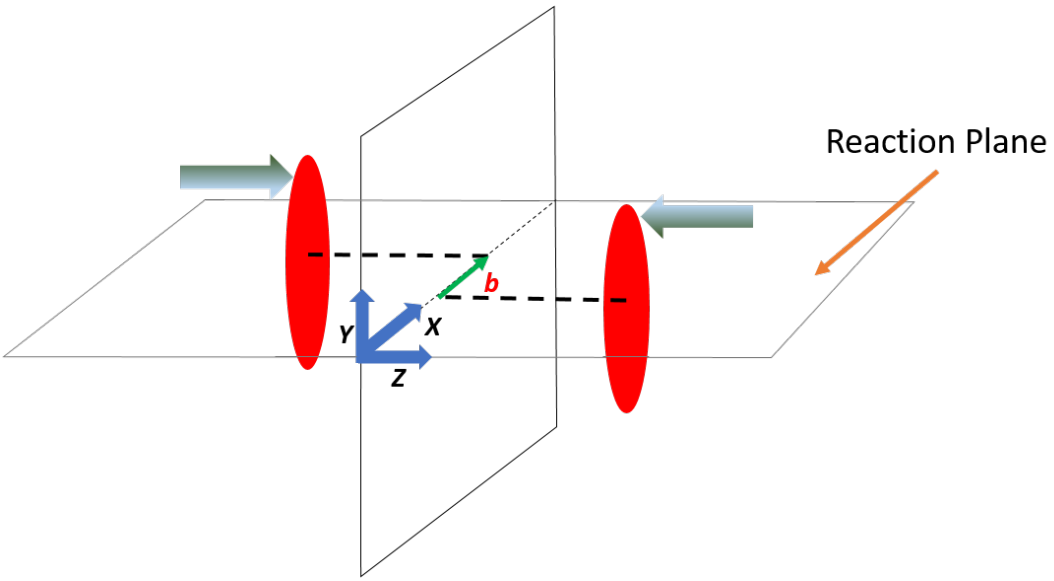

Figure 1.4: A spatial three dimensional view of the two heavy nuclei briefly before the collision.

1.3 Hydrodynamics in Heavy Ion Collisions

As we can see hydrodynamics has been used to describe a substantial part of the time evolution of a nuclear collision, from τ_i to τ_f. Ideal and viscous hydrodynamics have been used by many research groups for this purpose [23, 24, 25, 26, 27, 28, 29, 30, 31, 32, 33, 34, 35, 36, 37, 38, 39, 40, 41, 42, 43, 44, 45, 46]. Initially ideal $2+1$ dimensional hydrodynamics had great success in the early days of RHIC. Motivated by the interest in the shear viscosity of QGP $2+1$ dimensional viscous hydrodynamic packages have been developed and applied to RHIC and LHC [32, 33]. More recently, full blown $3+1$ dimensional viscous hydro packages [40, 45, 44] have come out which allow for longitudinal profiles. Some of these packages run event by event and also have parallelization of code to save run time of the hydro evolution.

1.3.1 Geometry and Initial Conditions

A spatial visualization of a typical collision is given in Fig. 1.4. The impact parameter of the collision is marked as b. In Fig. 1.5 we see the same event in the transverse plane. The QGP is formed in the overlap zone of the two nuclei. For computing initial conditions *e.g.* of the local energy density in the overlap zone, we first need to compute the nucleon density in the individual nuclei. We use the Wood-Saxon profile [47] for this purpose,

$$\rho(\vec{x}) = \frac{\rho_0}{1 + \exp\left(\frac{\sqrt{x^2+y^2+z^2}-R}{a}\right)} \ , \tag{1.2}$$

here R is the radius of the nucleus, a is the surface thickness measuring the diffusiveness of the nucleus and ρ_0 is a normalization factor such that after integration over space we get the number of nucleons A ($\equiv$ *mass number*) in the nucleus *i.e.*

$$\int \rho(\vec{x}) \, d^3x = A \ . \tag{1.3}$$

Starting from this profile one can estimate the initial energy density in the collision using different models and degrees of freedom. The two major models used are the Glauber Model [48] (nucleon-nucleon collision) and the Color Glass Condensate [49, 50] (classical gluon production) model. For either case we start with a Woods-Saxon profile for the nucleon density. Working with relativistic Lorentz contracted nuclei we can treat the density to be residing only in the transverse plane, for this we integrate the density over the z-axis and compute the nucleon density as a function of only transverse coordinates ,

$$T(\vec{x}_\perp) = \int_{-\infty}^{+\infty} \frac{\rho_0}{1 + \exp\left(\frac{\sqrt{x^2+y^2+z^2}-R}{a}\right)}\, dz\ . \tag{1.4}$$

This is called the thickness function of the nucleus. In the Glauber Model the density after collision is assumed to be a sum of contributions of the density of the participant nucleons n_{part} and the density of the binary collisions n_{coll} in the transverse plane. n_{part} or the wounded nucleon density for two nuclei with mass numbers A and B is given by

$$\begin{aligned} n_{part} = T_A\left(x + \frac{b}{2}, y\right)\left[1 - \left(1 - \frac{1 - \sigma\ T_B(x - \frac{b}{2})}{B}\right)^B\right] \\ + T_B\left(x - \frac{b}{2}, y\right)\left[1 - \left(1 - \frac{1 - \sigma\ T_A(x + \frac{b}{2})}{B}\right)^A\right], \end{aligned} \tag{1.5}$$

and the binary collision density n_{coll} is given by

$$n_{coll} = \sigma\ T_A\left(x + \frac{b}{2}, y\right) T_B\left(x - \frac{b}{2}, y\right)\ . \tag{1.6}$$

In equations (1.5) and (1.6), σ is the inelastic nucleon-nucleon cross-section, b is the impact parameter and T_A and T_B are the thickness functions for nuclei A and B respectively. Finally the energy density from Glauber Model is proptional to a linear sum of n_{part} and n_{coll}

$$\epsilon \propto\ \alpha\ n_{coll} + (1 - \alpha) n_{part}\ . \tag{1.7}$$

CGC based initial conditions will be main source of initial conditions for the hydro code in this thesis and we will discuss it in detail in chapter 5. We will use a

CGC model developed by Fries, Kapusta and Li [51, 52] and further refined by Chen [6]. Some other widely used CGC based initial conditions in our field are the KLN model [53, 54] and the nucleon fluctuation inclusive IP-Glasma model [55, 56].

1.3.2 Thermal Freeze-out

At the time τ_f, a thermal freeze-out procedure needs to convert fluid cells to particles so that one can calculate the particle spectra. The Cooper-Frye [57] procedure is used for this purpose. Instead of fixing τ_f globally a better approach is to determine a decoupling temperature T_{dec} and find the isothermal hypersurface Σ. Computationally this problem is geometrical in nature. The Cooper-Frye prescription for calculating the momentum spectrum for a particle species i is given by summing the momentum flux outflow through the hypersurface Σ.

$$E\frac{dN_i}{d^3p} = \int_\Sigma \frac{g_i \;\; p \cdot d^3\sigma}{(2\pi)^3\left(e^{\frac{p.u-\mu_i}{T_{dec}}} \pm 1\right)} \tag{1.8}$$

Here g_i is the degeneracy factor for particle species i, $d^3\sigma^\mu$ is the normal vector to the hypersurface, μ_i is the chemical potential for species i and T_{dec} is the decoupling temperature at which hypersurface resides. A sharp freeze-out corresponds to an instantaneous switch from very small (in the hydro phase) to very large mean free path. These could be improved by switching to a Boltzmann transport code like URQMD [58, 59] before freeze-out. In this work we will use a freeze-out code developed by S. Rose where needed.

1.4 A Selection of Important Observables

1.4.1 Transverse Anisotropies and Spectra

In Fig. 1.5 we can see the shaded red region were the collision takes place. In a typical collision at RHIC the temperature of the hot nuclear matter generated

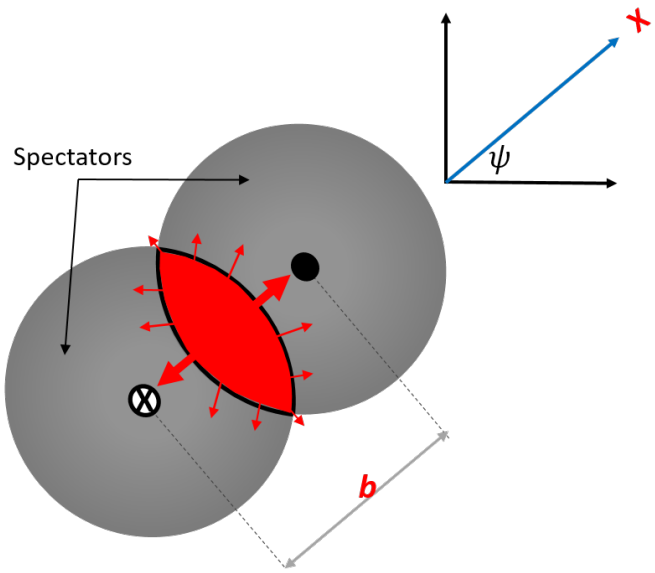

Figure 1.5: Collision geometry in transverse plane. The nucleus on the right is traveling in positive z direction (*or out of page*) and the nucleus on the left is going in the opposite direction. We will define the x-axis as being along the impact parameter and the $x-\eta$ plane is the reaction plane.

could be as high as 10^{12} K. For a off-center collision such as the one depicted in Fig. 1.5 we can see a spatial anisotropy is present. The hot QCD matter has a smaller length along the impact parameter, which results in a higher pressure gradients. This spatial anisotropy should result in a momentum anisotropy of the particles produced. To quantify this momentum anisotropy, we can perform a Fourier expansion of the transverse momentum spectra.

$$E\frac{d^3N_i}{dp^3}(b) = \frac{d^2N_i}{2\pi p_T dp_T dy}\left(1+\sum_{n=1}^{\infty} 2\ \ v_n(b,p_T)\cos\big(n(\phi-\psi)\big)+.....\right) \tag{1.9a}$$

$$v_n = \ \ <\cos\big(n(\phi-\psi)\big)> \tag{1.9b}$$

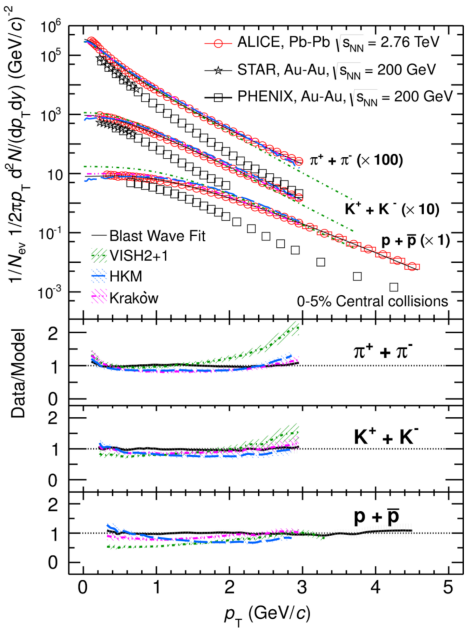

Figure 1.6: Particle spectra for pions, kaon and proton at PHENIX, STAR and ALICE. Plot taken with permission from [3].

where $\frac{d^2N_i}{2\pi p_T dp_T dy}$ is the particle distribution for species i, b is the impact parameter of the collision, ϕ is the azimuthal angle, ψ is a reference angle, p_T is the transverse momentum, p_L is the longitudinal momentum, i is the particle species and y is the rapidity defined as

$$y = \frac{1}{2}\log\left(\frac{E + p_L}{E - p_L}\right) \tag{1.10}$$

In Fig. 1.6 one can see the particle spectra for various species π^+, π^-, K^+, K^- etc at both RHIC (STAR and PHENIX) and LHC (ALICE). The v_2 parameter in equation (1.9), gives a measure of the elliptic flow in HIC. v_2 has been experimentally measured at RHIC and LHC [60, 61]. In Fig. 1.7 we see the elliptic flow results from the detectors at RHIC. Much recently, higher harmonics have been detected at LHC [62]. v_2 has been a very important quantity to verify the validity of hydrodynamic

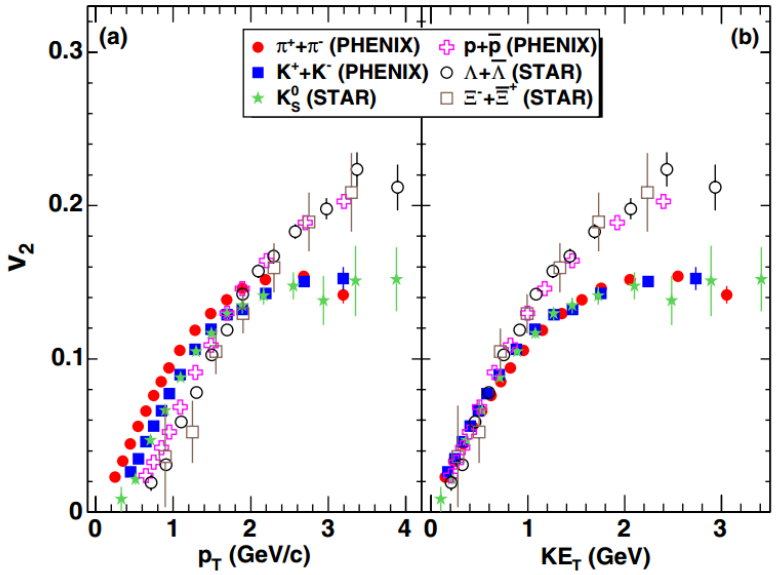

Figure 1.7: Plot for elliptic flow v_2 as a function of transverse momentum p_T and kinetic energy KE_T from the STAR and PHENIX collaborations at RHIC measured at $\sqrt{s_{NN}}$= 200 GeV. Plots taken with permission from [4].

apparatus.

1.4.2 HBT Radii

The shape and dimensions of the hot QCD matter would be a quantity which would be very interesting to measure. It is possible to use two particle interferometry (the Hanbury-Brown and Twiss Effect [63]) techniques to experimentally measure this information. For these measurements, we need the two particle correlations in momentum space, which can be extracted from the particle spectra.

$$C(p_1, p_2) = \frac{dN}{d^3p_1 d^3p_2} \Big/ \left(\frac{dN}{d^3p_1} . \frac{dN}{d^3p_2} \right) \tag{1.11}$$

Particles with similar momentum will have larger correlations. The correlation can be expressed in terms of q, K where $q = p_1 - p_2$ and $K = \frac{p_1+p_2}{2}$. They together

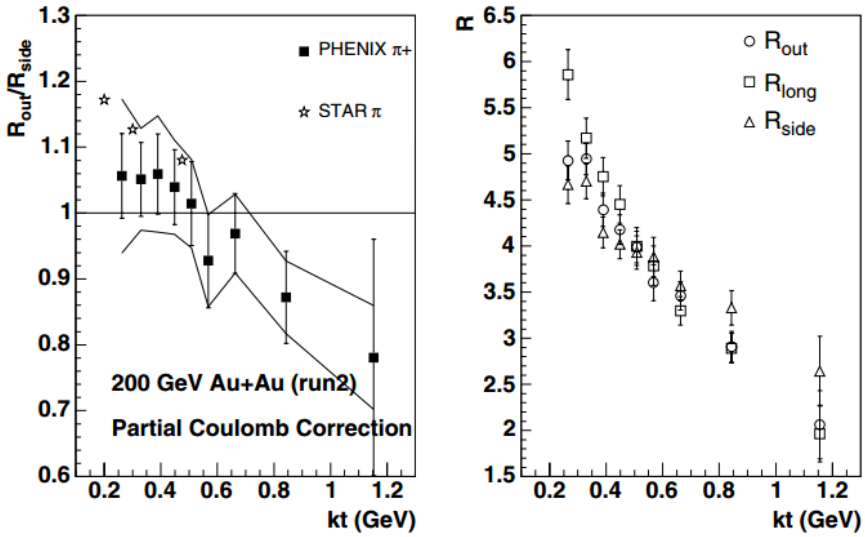

Figure 1.8: HBT radii plotted with respect to the transverse kinetic energy at the PHENIX and STAR experiments. **Left Panel:** Shows the results for R_{out}/R_{side} from both PHENIX and STAR experiments. **Right Panel:** Shows the results for R_{out}, R_{long} and R_{side} from the PHENIX experiment. Plots taken with permission from [5].

satisfy the orthogonality relation

$$K_\mu q^\mu = 0 \tag{1.12}$$

The correlation can now be expressed as [64, 65, 66]

$$C(q,K) = 1 + e^{-R_{side}^2 q_{side}^2 - R_{out}^2 q_{out}^2 - R_{long}^2 q_{long}^2} \tag{1.13}$$

Here *"long"* is the longitudinal or beam direction, *"out"* is the direction parallel to that component of K which is perpendicular to the beam direction, and *"side"* is orthogonal to the other two directions. R_{side}, R_{out} and R_{long} are called the HBT radii and they measure the dimensions of the emission regions. In Fig. 1.8 we can see the

experimentally measured HBT radii at RHIC. We can see that R_{out}/R_{side} stays close to 1.0 suggestive of a faster freeze out.

1.5 Objective and Outline of This Thesis

Our goal has been to develop a parallelized $3+1$ dimensional hydro package including vorticity effects, shear viscosity and bulk viscosity. In chapter 2, we will discuss the equations of relativistic hydrodynamics, specifically the Israel Stewart equations. We will derive the specific equations which we will be solving in our hydro code. In chapter 3, we will look into the details of the hydro algorithms and the computational parallelization we have used in our hydro. In chapter 4 we will look into some of the numerical results and benchmark tests we did with our hydro code. And in chapter 5, we will look into the specific CGC based initial conditions which we have run with our hydro code and present some results.

2. RELATIVISTIC HYDRODYNAMICS

2.1 Background

In this chapter we will develop the framework of relativistic viscous hydrodynamics. The first attempt at relativistic viscous hydrodynamics could be the relativistic version of the Navier-Stokes equations [67, 68], which are first order in a gradient expansion of the velocity field. However these equations gives us acausal results [69]. For quite some time now, the Israel Stewart equations [70] have been used to model causal dissipative hydrodynamics equations for heavy ion collisions. They include second order gradients of the velocity field. We will look into the various approaches to arrive at the Israel Stewart equations and also further simplify the specific equation which we will implement for our code.

2.1.1 Coordinate System and Metric

At this point we should clarify that the metric of choice for our hydro code in $(3+1)$ viscous and $(3+1)$ ideal case is $g^{\mu\nu} = diag\{1, -1, -1, -\frac{1}{\tau^2}\}$ for the $\{\tau, x, y, \eta\}$ coordinate system. Here, τ is the longitudinal proper time and η is the rapidity.

$$\tau = \sqrt{t^2 - z^2} \tag{2.1}$$

$$\eta = \frac{1}{2}\log\frac{1+\frac{z}{t}}{1-\frac{z}{t}} = \text{arctanh}(\frac{z}{t}) \tag{2.2}$$

This coordinate system is more convenient for a system expanding strongly in the z-direction. In particular boost invariance along the z-axis becomes a simple translational invariance along the η-axis. However, we have also formulated the hydro code in the simpler Minkowski metric $\{t, x, y, z\}$ with $g^{\mu\nu} = diag\{1, -1, -1, -1\}$,

especially to test some cases of interest in $(1+1)$ and $(2+1)$ dimensions. We will make a note of the difference in the formulation of equations in those two cases at various points in the thesis. But for the rest of the chapter we aim to simplify the equations for the hyperbolic $\{\tau, x, y, \eta\}$ coordinate system. Please see the appendix for more details on the hyperbolic coordinate system.

2.1.2 Ideal Relativistic Hydrodynamics

In the relativistic regime the Lorentz four velocity in Minkowski space is given by,

$$u^{\mu} = \frac{dX^{\mu}}{d\tau}. \tag{2.3}$$

Here the Greek indices run from 0 to 3 for the four dimensional space. The proper-time increment is given by

$$d\tau^2 = g_{\mu\nu} dx^{\mu} dx^{\nu}. \tag{2.4}$$

Now, in order to obtain energy-momentum conservation equations we need to derive the energy momentum tensor $T^{\mu\nu}$. Here we denote the ideal part of the energy momentum tensor as $T^{\mu\nu}_{id}$. Once we impose the restrictions on the energy momentum tensor to be symmetric, and Lorentz covariant, and we require that T^{00}_{id} represents the energy density ϵ in the local rest frame we get the following expression

$$T^{\mu\nu}_{id} = \epsilon\, u^{\mu} u^{\nu} - p\, \Delta^{\mu\nu}. \tag{2.5}$$

Here $\Delta^{\mu\nu} = g^{\mu\nu} - u^{\mu}u^{\nu}$ is a projection operator orthogonal to u^{μ} ($i.e\ \Delta^{\mu\nu}u_{\nu} = 0$), ϵ is the local rest frame energy density and p is the pressure given by the equation of state. And in absence of external sources the conservation equations for energy and

momentum are

$$\partial_\mu T^{\mu\nu}_{id} = 0. \tag{2.6}$$

2.1.3 Non-Relativistic Dissipative Hydrodynamics

Let us first take a brief look at the theory of non-relativistic hydrodynamics. For the ideal, inviscid fluid we have Euler's equations (conservation of momentum in three directions) [71]

$$\partial_t v^i + (\vec{v} \cdot \vec{\partial}) v^i = -\frac{1}{\rho} \partial_i p. \tag{2.7}$$

and the continuity equation (conservation of mass)

$$\partial_t \rho + \rho \, \vec{\partial} \cdot \vec{v} + (\vec{v} \cdot \vec{\partial}) \, \rho = 0. \tag{2.8}$$

These equations (2.7, 2.8) are the non-relativistic analog of equation (2.6). From equation (2.7) we can see that the flow fields are dictated by the gradient of the pressure. This would be more prominent initially if the flow is small or zero in the initial stages. For the viscous case we have the Navier-Stokes equations which amend equation (2.7) by an additional term

$$\partial_t v^i + (\vec{v} \cdot \vec{\partial}) v^i = -\frac{1}{\rho} \partial_i p - \frac{1}{\rho} \frac{\partial \Pi^{ki}}{\partial x^k} \tag{2.9}$$

and defines the stress tensor Π^{ki} through gradients of the velocity field.

$$\begin{aligned}\Pi^{ki} &= \pi^{ki} + \delta^{ki}\Pi \,. \\ \pi^{ki} &= -\eta\left(\frac{\partial v^i}{\partial x^k} + \frac{\partial v^k}{\partial x^i} - \frac{2}{3}\delta^{ki}\frac{\partial v^l}{\partial x^l}\right). \\ \Pi &= -\zeta\,\frac{\partial v^l}{\partial x^l}\,. \end{aligned} \tag{2.10}$$

Π^{ki} has both shear (π^{ki}) and bulk (Π) components, and here η is the shear viscosity and ζ is the bulk viscosity. The shear component (π^{ki}), as we can see from equation (2.10), is a measure of the resistance in fluid coming from gradients of velocity orthogonal to the flow direction. Even though this matrix may have diagonal components, the sum of all parallel to the flow contributions (*i.e.* the trace of the matrix) is zero by construction. Intuitively we can say the total effect of shear viscosity is a drag orthogonal to the flow direction. The bulk viscosity in contrast depends solely on gradients in velocity parallel/anti-parallel to the flow direction, this can be seen as a compression or expansion effect of viscosity in the system.

2.1.4 Energy Momentum Tensor in Hyperbolic Metric

Moving on to relativistic viscous hydrodynamics, we need to add the corresponding viscous corrections to the ideal energy momentum tensor. So we can represent the viscous energy momentum tensor and the conservation equation as

$$T^{\mu\nu} = T^{\mu\nu}_{id} + \Pi^{\mu\nu} \tag{2.11a}$$

$$\partial_{;\mu} T^{\mu\nu} = 0. \tag{2.11b}$$

As we saw earlier in non-relativistic viscous hydrodynamics, we will do the cus-

tomary thing of separating $\Pi^{\mu\nu}$ into a traceless shear part and the remnant as bulk viscous component. We decompose

$$\Pi^{\mu\nu} = \pi^{\mu\nu} + \Delta^{\mu\nu}\Pi \tag{2.12}$$

where $\pi^{\mu\nu}$ is the shear viscous tensor and Π is the bulk viscous coefficient. $\pi^{\mu\nu}$ is traceless and orthogonal to the flow field

$$\pi^{\mu\nu} g_{\mu\nu} = 0 \tag{2.13a}$$

$$\pi^{\mu\nu} u_{\nu} = 0 = u_{\mu}\pi^{\mu\nu} \tag{2.13b}$$

Notice that we wrote equation (2.11b) with covariant derivative because of the metric $g^{\mu\nu} = diag\{1, -1, -1, -\frac{1}{\tau^2}\}$. If we write this out explicitly we obtain equations that look like a conservation law in the usual metric, and additional terms that will be treated as source terms. Expanding into four separate equations we get

$$\partial_\tau T^{\tau\tau} + \partial_x T^{\tau x} + \partial_y T^{\tau y} + \partial_\eta T^{\tau\eta} = -\tau T^{\eta\eta} - \frac{1}{\tau} T^{\tau\tau}. \tag{2.14a}$$

$$\partial_\tau T^{x\tau} + \partial_x T^{xx} + \partial_y T^{xy} + \partial_\eta T^{x\eta} = -\frac{1}{\tau} T^{x\tau}. \tag{2.14b}$$

$$\partial_\tau T^{y\tau} + \partial_x T^{yx} + \partial_y T^{yy} + \partial_\eta T^{y\eta} = -\frac{1}{\tau} T^{y\tau}. \tag{2.14c}$$

$$\partial_\tau T^{\eta\tau} + \partial_x T^{\eta x} + \partial_y T^{\eta y} + \partial_\eta T^{\eta\eta} = -\frac{3}{\tau} T^{\eta\tau}. \tag{2.14d}$$

For a flux based finite volume numerical scheme the above equations are in appropriate conservative form with source terms as we will discuss in the next chapter. We can simplify two of these source terms by multiplying each of the four equations

with τ. The result is

$$\partial_\nu(\tau T^{\tau\nu}) = -\tau^2\, T^{\eta\eta} \tag{2.15a}$$

$$\partial_\nu(\tau T^{x\nu}) = 0. \tag{2.15b}$$

$$\partial_\nu(\tau T^{y\nu}) = 0. \tag{2.15c}$$

$$\partial_\nu(\tau T^{\eta\nu}) = -2\, T^{\eta\tau}. \tag{2.15d}$$

with only two source terms remaining and $\partial^\mu = \left(\frac{\partial}{\partial\tau}, \frac{\partial}{\partial x}, \frac{\partial}{\partial y}, \frac{\partial}{\partial\eta}\right)$. The multiplication with τ also changes our "conserved" variables to $\{\tau T^{\tau\tau}, \tau T^{x\tau}, \tau T^{y\tau}, \tau T^{\eta\tau}\}$. And these conserved variable will be governed by the above equation. Let's also note that equations (2.15a) through (2.15d) are true for both the dissipative and the inviscid case.

2.1.5 Relativistic Navier-Stokes Equations

In order to arrive at equations for the viscous coefficients we take the entropy flow $s^\mu = su^\mu$ and impose the second law of thermodynamics $\partial_\mu s^\mu \geq 0$.

$$\partial_\mu s^\mu = u^\mu \partial_\mu s + s\, \partial_\mu u^\mu \tag{2.16}$$

In equation (2.16), using equation (2.11b) and with some algebra we can arrive at

$$\partial_\mu s^\mu = \frac{1}{T}\Pi^{\mu\nu}\nabla_{(\mu}u_{\nu)} \geq 0 \tag{2.17}$$

Here $\nabla_\mu = \Delta_{\mu\nu}\partial^\nu$ and the parenthesis brackets () is the symmetric operator *i.e.* $A_{(\mu}B_{\nu)} = \frac{1}{2}(A_\mu B_\nu + A_\nu B_\mu)$. Now we can apply the decomposition (2.12) and truly

separate $\partial_\mu s^\mu$ into traceless and the non-traceless part. With some more algebra we arrive at

$$\partial_\mu s^\mu = \frac{1}{2T}\pi^{\mu\nu}\nabla_{<\mu}u_{\nu>} + \frac{1}{T}\Pi\ \nabla_\alpha u^\alpha \geq 0 \tag{2.18}$$

Here $\nabla_{<\mu}u_{\nu>} \equiv 2\nabla_{(\mu}u_{\nu)} - \frac{2}{3}\Delta_{\mu\nu}\nabla_\alpha u^\alpha$ is the traceless part of $\nabla_\mu u_\nu$. If we are to guarantee the positivity of equation (2.18), then that will give us expressions for shear viscosity and bulk viscosity.

$$\pi^{\mu\nu} = \eta\, \nabla^{\langle\mu}u^{\nu\rangle}, \tag{2.19}$$

$$\Pi = \zeta\, \nabla_\alpha u^\alpha \tag{2.20}$$

where η is the shear viscosity coefficient and ζ is the bulk viscosity coefficient. The above equations are the relativistic Navier Stokes equations. The Navier Stokes value of shear stress (2.19) is also expressed as

$$\pi^{\mu\nu} = 2\ \eta\ \sigma^{\mu\nu}, \tag{2.21}$$

Here $\sigma^{\mu\nu}$ is the traceless, symmetric and orthogonal flow portion of $\partial_{;\mu}u_\nu$, that we describe in more detail in section 2.2.3.

However, there is a well known causality problem with these equations in the relativistic case. For instance if we give a small perturbation in velocity then the evolution of that perturbation can go to infinite speeds violating causality. Corrections to the Navier-Stokes equations have been worked out in the past by Muller, Israel and Stewart [70]. These second order corrections are now known as the Israel-Stewart equations. We will look into these equations derived from both the second

law of thermodynamics and from the Boltzmann equation.

2.2 Israel Stewart Formalism

2.2.1 Arriving From Second Law of thermodynamics

The generalized definition of the entropy current was suggested, which must include viscous corrections

$$s^{\mu} = su^{\mu} - \frac{\beta_2}{2T}u^{\mu}\,\pi_{\alpha\beta}\,\pi^{\alpha\beta} - \frac{\beta_0}{2T}\,u^{\mu}\Pi^2 + \mathcal{O}(\Pi^3) \tag{2.22}$$

where β_0 and β_2 are coefficients which can be written in terms of relaxation times τ_π and τ_Π, respectively as, $\beta_0 = \frac{\tau_\Pi}{\zeta}$ and $\beta_2 = \frac{\tau_\pi}{2\eta}$. Again, if we apply $\partial_\mu s^\mu \geq 0$ to equation (2.22) we get the Israel Stewart equations for shear and bulk stress.

$$\pi^{\mu\beta} = \eta\ \left(\nabla^{<\mu}u^{\beta>}\ - \pi^{\mu\beta}Tu^{\rho}\partial_{\rho}\left(\frac{\beta_2}{T}\right) - 2\beta_2 u^{\rho}\partial_{\rho}\pi^{\mu\beta} - \beta_2\pi^{\mu\beta}\partial_{\rho}u^{\rho}\right) \tag{2.23}$$

$$\Pi = \zeta\ \left(\nabla_{\rho}u^{\rho}\ - \frac{1}{2}\Pi Tu^{\rho}\partial_{\rho}\left(\frac{\beta_0}{T}\right) - \beta_0 u^{\rho}\partial_{\rho}\Pi - \frac{1}{2}\beta_0\Pi\partial_{\rho}u^{\rho}\right) \tag{2.24}$$

2.2.2 Derivation From the Boltzmann Equation

We will also show the approach for deriving the shear viscous Israel Stewart equation from the Boltzmann transport equation [72]

$$p^{\mu}d_{\mu}f(x,t,p) = C(x) \tag{2.25}$$

where f is the distribution function, p^μ is the four momentum and C is the

collision term. The zeroth and first moments of the Boltzmann transport equation give us charge and energy-momentum conservation, which we may ignore for now. The idea is to work out the second moment of the Boltzmann transport equation so that we can find deviations from $T^{\mu\nu}_{id}$. Using $\int d\omega \equiv \int \frac{d^3p}{(2\pi)^3 p_0}$ for integrating over momentum space

$$\int d\omega \; p^\mu p^\alpha p^\beta d_\mu f = \int d\omega \; p^\alpha p^\beta C \tag{2.26}$$

The equilibrium distribution f_0 is given by

$$f_0(u_\mu p^\mu) = \exp\bigl(-\beta \; u_\mu p^\mu\bigr) \tag{2.27}$$

with $\beta = \frac{1}{T}$ and we can use the following relaxation time approximation for the collision term.

$$C = -p_\mu u^\mu \frac{f - f_0}{\tau_\Pi} \tag{2.28}$$

We can write the deviations from local equilibrium f_0 as

$$f = f_0(1 + \delta f). \qquad |\delta f| \ll 1 \tag{2.29}$$

In order to find corrections to $T^{\mu\nu} = T^{\mu\nu}_{id} + \pi^{\mu\nu}$, coming only from the shear viscous effects we can write the correction term δf as

$$\delta f(x, t, p) = \epsilon_{\lambda\nu}(x, t) p^\lambda p^\nu \tag{2.30}$$

From these assumptions (equation (2.27) through (2.30)), and starting from the second moment equation (2.26), we can arrive at the equations of motion including

dissipative corrections to second order. For a complete derivation and the intermediate steps please refer to the appendix of [72]. Here we will quote the familiar final result.

$$\tau_{\Pi}\Delta^{\mu}_{\alpha}\Delta^{\nu}_{\beta}\, D\pi^{\alpha\beta} + \pi^{\mu\nu} = \eta\nabla^{<\mu}u^{\nu>} - 2\tau_{\pi}\pi^{\alpha(\phi}\Omega^{\nu)}_{\alpha} \tag{2.31}$$

here $D = u^{\mu}\partial_{\mu}$ and $\Omega^{\mu\nu} = \Delta^{\mu\alpha}\Delta^{\nu\beta}(\frac{\partial_{;\beta}u_{\alpha} - \partial_{;\alpha}u_{\beta}}{2})$ is the anti-symmetric tensor, which is used to evaulate the vorticity contribution. One can also find a corresponding equation of motion for bulk viscosity Π.

2.2.3 Israel-Stewart Equations

We can arrive at the Israel-Stewart equations from different approaches, let's look at the final version of the equation which we wish to solve numerically. In this equation we also include the $\frac{4}{3}\pi^{\mu\nu}\partial_{\rho}u^{\rho}$ contribution as mentioned in [73] which preserves conformal symmetry. Since we will be working in hyperbolic coordinate system $\{\tau, x, y, \eta\}$, we also need to replace all derivatives with the covariant derivatives. This equation is really a tensor equation consisting of 16 individual equations. But once we consider the symmetry, tracelessness and orthogonality to u^{μ}, for $\pi^{\mu\nu}$ we see that there are really only 5 independent variables.

$$\langle u^{\rho}\partial_{;\rho}\pi^{\mu\nu}\rangle \;=\; \left(\frac{\pi^{\mu\nu}_{NS} - \pi^{\mu\nu}}{\tau_{\pi}}\right) - \frac{4}{3}\,\pi^{\mu\nu}\,\partial_{;\rho}u^{\rho} + 2\,\pi^{\phi(\mu}\Omega^{\nu)}{}_{\phi} \tag{2.32}$$

here, $\pi^{\mu\nu}_{NS}$ is the Navier Stokes value for the shear stress, as previously mentioned in equations (2.19) and (2.21).

The angled bracket $\langle\rangle$ operation makes the enclosed tensor symmetric, traceless and orthogonal to the flow field. This is achieved by acting the tensor with the

following operators

$$\sigma^{\mu\nu} \equiv \langle \partial^{\mu}_{;} u^{\nu} \rangle \equiv \Delta^{\mu\nu\alpha\beta} \partial_{;\alpha} u_{\beta} \tag{2.33a}$$

$$\langle u^{\rho} \partial_{;\rho} \pi^{\mu\nu} \rangle \equiv \Delta^{\mu\nu}{}_{\alpha\beta} u^{\rho} \partial_{;\rho} \pi^{\alpha\beta} \tag{2.33b}$$

and $\Delta^{\mu\nu\alpha\beta}$ and $\Delta^{\mu\nu}{}_{\alpha\beta}$ are both double symmetric, orthogonal to flow and traceless operators defined by

$$\Delta^{\mu\nu\alpha\beta} \equiv \frac{1}{2}(\Delta^{\mu\alpha}\Delta^{\nu\beta} + \Delta^{\mu\beta}\Delta^{\nu\alpha}) - \frac{1}{3}(\Delta^{\mu\nu}\Delta^{\alpha\beta}) \tag{2.34a}$$

$$\Delta^{\mu\nu}{}_{\alpha\beta} \equiv \frac{1}{2}(\Delta^{\mu}_{\alpha}\Delta^{\nu}_{\beta} + \Delta^{\mu}_{\beta}\Delta^{\nu}_{\alpha}) - \frac{1}{3}(\Delta^{\mu\nu}\Delta_{\alpha\beta}) \tag{2.34b}$$

The Israel-Stewart formalism for bulk viscosity, being a non-tensor equation and absent of vorticity affects, is a relatively simpler one and given by

$$u^{\rho}\partial_{;\rho}\Pi = \left(\frac{\Pi_{NS} - \Pi}{\tau_{\Pi}}\right) - \frac{4}{3}\,\Pi\,\partial_{;\rho}u^{\rho} \tag{2.35}$$

Here the Navier Stokes value of the bulk stress is given by

$$\Pi_{NS} = -\zeta\ \partial_{;\rho}u^{\rho} \tag{2.36}$$

2.2.4 Rewriting Israel-Stewart Equations in Conservative Form

2.2.4.1 The Shear Israel-Stewart Equation

We want our shear stress tensor IS-equation rewritten in conservative form. We can begin doing that by simplifying the left hand side of equation (2.32). Every term on the right hand side of equation (2.32) acts like a source term to the conservation

equation. We will also use the operator D for brevity. So the left hand side of equation (2.32) can be simplified to

$$\begin{aligned}
\langle D\pi^{\mu\nu}\rangle &= \Delta^{\mu\nu}{}_{\alpha\beta}\, D\pi^{\alpha\beta} \\
&= \frac{1}{2}\Big((g^{\mu}{}_{\alpha} - u^{\mu}u_{\alpha})(g^{\nu}{}_{\beta} - u^{\nu}u_{\beta}) + (g^{\mu}{}_{\beta} - u^{\mu}u_{\beta})(g^{\nu}{}_{\alpha} - u^{\nu}u_{\alpha}) \\
&\quad - \frac{1}{3}(g^{\mu\nu} - u^{\mu}u^{\nu})(g_{\alpha\beta} - u_{\alpha}u_{\beta})\Big)\, D\pi^{\alpha\beta} \\
&= \frac{1}{2}\Big((g^{\mu}{}_{\alpha}g^{\nu}{}_{\beta} - g^{\nu}{}_{\beta}u^{\mu}u_{\alpha} - g^{\mu}{}_{\alpha}u^{\nu}u_{\beta} + u^{\mu}u_{\alpha}u^{\nu}u_{\beta}) \\
&\quad + (g^{\mu}{}_{\beta}g^{\nu}{}_{\alpha} - u^{\mu}u_{\beta}g^{\nu}{}_{\alpha} - g^{\mu}{}_{\beta}u^{\nu}u_{\alpha} + u^{\mu}u_{\beta}u^{\nu}u_{\alpha}) \\
&\quad - \frac{1}{3}(g^{\mu\nu}g_{\alpha\beta} - g_{\alpha\beta}u^{\mu}u^{\nu} - g^{\mu\nu}u_{\alpha}u_{\beta} + u^{\mu}u^{\nu}u_{\alpha}u_{\beta})\Big)\; D\pi^{\alpha\beta} \\
&= D\pi^{\mu\nu} + \frac{1}{2}\Big((-g^{\nu}{}_{\beta}u^{\mu}u_{\alpha} - g^{\mu}{}_{\alpha}u^{\nu}u_{\beta} + u^{\mu}u_{\alpha}u^{\nu}u_{\beta} \\
&\quad - u^{\mu}u_{\beta}g^{\nu}{}_{\alpha} - g^{\mu}{}_{\beta}u^{\nu}u_{\alpha} + u^{\mu}u_{\beta}u^{\nu}u_{\alpha}) \\
&\quad - \frac{1}{3}(g^{\mu\nu}g_{\alpha\beta} - g_{\alpha\beta}u^{\mu}u^{\nu} - g^{\mu\nu}u_{\alpha}u_{\beta} + u^{\mu}u^{\nu}u_{\alpha}u_{\beta})\Big)\; D\pi^{\alpha\beta} \\
&= D\pi^{\mu\nu} + \frac{1}{2}\Big((-g^{\nu}{}_{\beta}u^{\mu}u_{\alpha} - g^{\mu}{}_{\alpha}u^{\nu}u_{\beta} - u^{\mu}u_{\beta}g^{\nu}{}_{\alpha} - g^{\mu}{}_{\beta}u^{\nu}u_{\alpha}) \\
&\quad - \frac{1}{3}(g^{\mu\nu}g_{\alpha\beta} - g_{\alpha\beta}u^{\mu}u^{\nu})\Big)\; D\pi^{\alpha\beta}
\end{aligned} \tag{2.37}$$

We now use the following relations to simplify our expression further. These relations come from tracelessness and transversality of $\pi^{\mu\nu}$.

- $u_{\alpha}D\pi^{\alpha\beta} \equiv -\pi^{\alpha\beta}Du_{\alpha}$ from transversality with respect to flow
- $u_{\beta}D\pi^{\alpha\beta} \equiv -\pi^{\alpha\beta}Du_{\beta}$ from transversality with respect to flow
- $u_{\alpha}u_{\beta}D\pi^{\alpha\beta} \equiv 0$ from transversality with respect to flow
- $g_{\alpha\beta}D\pi^{\alpha\beta} \equiv -\pi^{\alpha\beta}Dg_{\alpha\beta} = 0$ from tracelessness

For our metric of choice $g_{\alpha\beta} = \{1, -1, -1, -\tau^2\}$ in the evaluation of $Dg_{\alpha\beta}$, the covariant derivative tensor $\partial_{;\rho} g_{\alpha\beta}$ has all zero entries. Now we can simplify (2.37) further

$$\begin{aligned} < D\pi^{\mu\nu} > &= D\pi^{\mu\nu} + \frac{1}{2}(g^{\nu}{}_{\beta} u^{\mu}\pi^{\alpha\beta} Du_{\alpha} + g^{\mu}{}_{\beta} u^{\nu}\pi^{\alpha\beta} Du_{\alpha} + g^{\mu}{}_{\alpha} u^{\nu}\pi^{\alpha\beta} Du_{\beta} + g^{\nu}{}_{\alpha} u^{\mu}\pi^{\alpha\beta} Du_{\beta}) \\ &= D\pi^{\mu\nu} + \frac{1}{2}((u^{\mu}\pi^{\nu\beta} + u^{\nu}\pi^{\mu\beta})Du_{\beta} + (u^{\nu}\pi^{\mu\beta} + u^{\mu}\pi^{\nu\beta})Du_{\beta}) \\ &= D\pi^{\mu\nu} + (u^{\nu}\pi^{\mu\beta} + u^{\mu}\pi^{\nu\beta})Du_{\beta} \\ &= u^{\rho}\partial_{;\rho}\pi^{\mu\nu} + (u^{\nu}\pi^{\mu\beta} + u^{\mu}\pi^{\nu\beta})u^{\rho}\partial_{;\rho}u_{\beta} \end{aligned} \tag{2.38}$$

Let's apply this result to the left hand side of equation (2.32) to get

$$u^{\rho}\partial_{;\rho}\pi^{\mu\nu} + (u^{\mu}\pi^{\nu\beta} + u^{\nu}\pi^{\mu\beta})Du_{\beta} \;=\; \left(\frac{\pi^{\mu\nu}_{NS} - \pi^{\mu\nu}}{\tau_{\pi}}\right) - \frac{4}{3}\pi^{\mu\nu}(\partial_{;\rho}u^{\rho}) + 2\,\pi^{\phi(\mu}\Omega^{\nu)}{}_{\phi} \tag{2.39}$$

$$u^{\rho}\partial_{\rho}\pi^{\mu\nu} + G^{\mu\nu} \;=\; \left(\frac{\pi^{\mu\nu}_{NS} - \pi^{\mu\nu}}{\tau_{\pi}}\right) - \frac{4}{3}\pi^{\mu\nu}(\partial_{;\rho}u^{\rho}) - (u^{\mu}\pi^{\nu\beta} + u^{\nu}\pi^{\mu\beta})Du_{\beta} + 2\,\pi^{\phi(\mu}\Omega^{\nu)}{}_{\phi} \tag{2.40}$$

Here $G^{\mu\nu}$ is the geometrical term which comes from the covariant differentiation of $u^{\rho}\partial_{;\rho}\pi^{\mu\nu}$, please find the explicit terms for $G^{\mu\nu}$ in equation (A.19) of appendix A. We also divide the equation by u^{τ} which is same as the Lorentz γ factor to arrive at

$$\partial_\tau \pi^{\mu\nu} + v_x \partial_x \pi^{\mu\nu} + v_y \partial_y \pi^{\mu\nu} + v_\eta \partial_\eta \pi^{\mu\nu} \; = \left(\frac{\pi^{\mu\nu}_{NS} - \pi^{\mu\nu}}{\tau_\pi \gamma} \right) - \frac{4}{3\gamma} \pi^{\mu\nu} (\partial_{;\rho} u^\rho) - \frac{(u^\mu \pi^{\nu\beta} + u^\nu \pi^{\mu\beta})}{\gamma} D u_\beta - \frac{G^{\mu\nu}}{\gamma} + 2 \frac{\pi^{\phi(\mu} \Omega^{\nu)}{}_{\phi}}{\gamma} \quad (2.41)$$

We can finally rewrite equation (2.32) in conservative form with a source term. This is the preferred form for hydro algorithms to numerically solve these equations. The source terms also are independent of any derivative of $\pi^{\mu\nu}$

$$\partial_\tau \pi^{\mu\nu} + \partial_x (v_x \pi^{\mu\nu}) + \partial_y (v_y \pi^{\mu\nu}) + \partial_\eta (v_\eta \pi^{\mu\nu}) \; = \left(\frac{\pi^{\mu\nu}_{NS} - \pi^{\mu\nu}}{\tau_\pi \gamma} \right) - \frac{4}{3} \frac{\pi^{\mu\nu} (\partial_{;\rho} u^\rho)}{\gamma} - \frac{(u^\nu \pi^{\mu\beta} + u^\mu \pi^{\nu\beta}) D u_\beta}{\gamma} - \frac{G^{\mu\nu}}{\gamma} + \pi^{\mu\nu} \partial_\rho (\frac{u^\rho}{\gamma}) + 2 \frac{\pi^{\phi(\mu} \Omega^{\nu)}{}_{\phi}}{\gamma} \quad (2.42)$$

2.2.4.2 The Bulk IS Equation

Simplifying the bulk IS equation to conservative form is relatively easier. We will quote the final result here.

$$\partial_\tau \Pi + \partial_x (v_x \Pi) + \partial_y (v_y \Pi) + \partial_\eta (v_\eta \Pi) \; = \left(\frac{\Pi_{NS} - \Pi}{\tau_\Pi \, \gamma} \right) - \frac{4}{3} \frac{\Pi (\partial_{;\rho} u^\rho)}{\gamma} + \Pi \partial_\rho (\frac{u^\rho}{\gamma}) \quad (2.43)$$

Equations (2.42) and (2.43) in addition to equations (2.15a, 2.15b, 2.15c, 2.15d)

form a complete set of equations for viscous second order relativistic hydrodynamics. We have already written them in explicit conservation form with source terms. This will enable us to readily apply established fluid dynamics algorithms to solve them.

3. HYDRO ALGORITHMS

Computational fluid dynamics is a simulation methodology in which we use computers and numerical schemes to discretize our equations of motion on a numerical grid. The system of discrete equations is then solved on computational clusters by using suitable algorithms. In the previous chapter we talked in detail about setting up the relativistic equations of motion pertaining to hydrodynamics and in this chapter we will study the algorithms used to solve the discrete form of those partial differential equations.

The first algorithm which we implemented to solve the hydrodynamical equations was SHASTA [74]. In 1+1 and 2+1 dimensions we found it gave good results for some standard problems. However in comparison to the Kurgunov Tadmor (KT) scheme [75] we found the latter being generally superior. While most of our 3+1 viscous hydrodynamics simulations have been done with the KT scheme, SHASTA is also available in our package.

3.1 The Primary Conserved Variables

Let us review the entire set of hydro equations. From equations (2.15a), (2.15b), (2.15c), (2.15d), (2.42) and (2.43) we can see that our list of 21 conserved variables are

$$\vec{\rho} = \{\tau T^{\tau\tau}, \tau T^{x\tau}, \tau T^{y\tau}, \tau T^{\eta\tau}, \pi^{\mu\nu}, \Pi\} \qquad \mu, \nu \in \{\tau, x, y, \eta\} \tag{3.1}$$

As we mentioned earlier in section (2.2.3), the $\pi^{\mu\nu}$ tensor is symmetric, traceless and orthogonal to the fluid flow velocity u^{μ},

$$\pi^{\mu\nu} = \pi^{\nu\mu} \tag{3.2a}$$

$$\pi^{\mu\nu} g_{\mu\nu} = 0 \tag{3.2b}$$

$$\pi^{\mu\nu} u_\nu = \pi^{\mu\nu} u_\mu = 0 \tag{3.2c}$$

These conditions reduce the number of independent variables in the shear stress tensor $\pi^{\mu\nu}$ from 16 to 5. We can write the $\pi^{\mu\nu}$ tensor as

$$\pi^{\mu\nu} = \begin{bmatrix} A_1 & A_2 & A_3 & A_4 \\ A_2 & \pi^{xx} & \pi^{xy} & \pi^{x\eta} \\ A_3 & \pi^{xy} & \pi^{yy} & \pi^{y\eta} \\ A_4 & \pi^{x\eta} & \pi^{y\eta} & A_5 \end{bmatrix} \tag{3.3}$$

Here our choice of dependent variables are $\pi^{xx}, \pi^{yy}, \pi^{xy}, \pi^{x\eta}, \pi^{y\eta},$. The other entries of the shear stress tensor, A_1 through A_5 can be calculated from the following relations provided we know the four velocity $u^\mu = \{u^\tau, u^x, u^y, u^\eta\}$

$$\begin{aligned} A_1 \equiv \pi^{\tau\tau} = \frac{1}{(u^\tau)^2 - (\tau u^\eta)^2} \Big[& \pi^{xx}(u^x)^2 + \pi^{yy}(u^y)^2 + 2\pi^{xy} u^x u^y \\ & + u^\eta \tau^2 \Big(2\pi^{x\eta} u^x + 2\pi^{y\eta} u^y - (\pi^{xx} + \pi^{yy}) u^\eta \Big) \Big] \end{aligned} \tag{3.4}$$

$$A_2 \equiv \pi^{\tau x} = \frac{\pi^{xx} u^x + \pi^{xy} u^y + \pi^{x\eta} u^\eta \tau^2}{u^\tau} \tag{3.5}$$

$$A_3 \equiv \pi^{\tau y} = \frac{\pi^{xy} u^x + \pi^{yy} u^y + \pi^{y\eta} u^\eta \tau^2}{u^\tau} \tag{3.6}$$

$$A_4 \equiv \pi^{\tau\eta} = \frac{1}{(u^\tau)^3 - u^\tau(\tau u^\eta)^2}\Bigg[\Bigg(\pi^{xx}(u^x)^2 + \pi^{yy}(u^y)^2 + 2\pi^{xy}u^x u^y - (u^\tau)^2(\pi^{xx} + \pi^{yy})\Bigg)u^\eta + \Bigg((u^\tau)^2 + (\tau u^\eta)^2)(\pi^{x\eta}u^x + \pi^{y\eta}u^y)\Bigg)\Bigg] \tag{3.7}$$

$$A_5 \equiv \pi^{\eta\eta} = \frac{1}{(u^\eta)^2\tau^4 - (u^\tau)^2\tau^2}\Bigg[\pi^{xx}\big((u^\tau)^2 - (u^x)^2\big) + \pi^{yy}\big((u^\tau)^2 - (u^y)^2\big) - 2\pi^{xy}u^x u^y - 2u^\eta\tau^2\big(\pi^{x\eta}u^x + \pi^{y\eta}u^y\big)\Bigg] \tag{3.8}$$

One can readily check that the resulting tensor $\pi^{\mu\nu}$ from equation (3.3) satisfies equations (3.2a, 3.2b, 3.2c). Since we need to only evolve 5 shear stress variables instead of 16, our number of conserved quantities reduces to the following 10.

$$\vec{\rho} = \{\tau T^{\tau\tau}, \tau T^{x\tau}, \tau T^{y\tau}, \tau T^{\eta\tau}, \pi^{xx}, \pi^{yy}, \pi^{xy}, \pi^{x\eta}, \pi^{y\eta}, \Pi\} \tag{3.9}$$

3.2 Hyperbolic Conservation Equations

The primary objective of any fluid dynamics algorithm is to solve hyperbolic equations of the type

$$\partial_t\rho + \partial_x(v_x\rho) = 0 \tag{3.10}$$

Here ρ is a conserved variable like mass density or momentum and v_x is the x-component of the fluid velocity. Algorithms are often first devised for this one dimensional simple form of a conservation equation. The computational approach in solving these equations is to begin with a start time t_0 for simulation and define an initial condition $\rho(t_0)$. For equation (3.10), in the space domain this is achieved

by discretizing the x-axis into a number of points with a fixed spacing. For our implementation of algorithms our approach to meshing is fixed spacing. However the dynamical spacing of grid points during the run time of the code is also an option, often mentioned as adaptive meshing in literature. Obviously, finer meshing in a region would result in higher accuracy for results in that region. Adaptive meshing would allow the concentration of points in key regions where we might have to resolve important structures like steep energy gradients, a complex boundary condition etc.

A difference equation is then devised based on the original differential equation. The algorithm then advances the conserved variable ρ, from a time t^n to t^{n+1}. Here we choose spacings Δx and Δt in x- and t- directions respectively. The time step forward can be expressed as

$$\rho^{n+1} - \rho^n = F(\rho^n, v_x^n, \Delta x, \Delta t) \tag{3.11}$$

The upper superscript n denotes the current time step, starting from the initial condition *i.e.* $\rho^n = \rho(t_0 + n\Delta t)$. Here $F(\rho^n, v_x^n, \Delta x, \Delta t)$ is the flux of the quantity ρ in or out of the spatial cell of size Δx considered here during the time step Δt.

For our calculation we will have to consider a more general equation in three dimensions of the form

$$\partial_t \rho + \partial_x(v_x \rho) + \partial_y(v_y \rho) + \partial_z(v_z \rho) = S(\rho, \vec{v}, t, x, y, z) \tag{3.12}$$

Here $S(\rho, t, x, y, z)$ acts like a source or sink term to the conservation equation. We saw in the last chapter that the relativistic hydro equations give us a non zero source term, that arises from using hyperbolic coordinates and becomes particularly lengthy when viscous terms are considered. However, once calculated the source terms simply need to be integrated over time to evaluate its contribution to ρ^n. To

proceed further we need to devise an algorithm to calculate the flux F, and we need to discuss the integration for the source term.

We would like to generalize the one dimensional equation (3.1) for multi-dimensional partial differential equations of the type (3.12). In one dimension the value of a variable at location x_i represents the region from $x_i - \frac{\Delta x}{2}$ to $x_i + \frac{\Delta x}{2}$. This could be something as simple as a piecewise linear assumption between the cells, or a higher order sophisticated fit like the WENO scheme [76, 77].

In three dimensions, discretization implies that the value of a variable at (x_i, y_j, z_k) approximates the value inside a cube with side length equal to grid spacing $\Delta x, \Delta y, \Delta z$ in x, y and z directions. Hence the three dimensional problem can be rephrased as one of flow of the conserved variable into or out of a cell (parallelepiped) of dimensions $\Delta x, \Delta y, \Delta z$, see Fig. 3.1. The net flow from or into a cell, can be expressed as the sum of fluxes through each face and the contribution of the source term inside the cell. For our problem in Cartesian coordinates we can achieve this by directional operator splitting.

$$\Delta\rho_{total} = \Delta\rho_X + \Delta\rho_Y + \Delta\rho_Z + \Delta\rho_S \tag{3.13a}$$

$$\Delta\rho_X = F_x(\rho^n, v_x^n, \Delta x, \Delta t) \tag{3.13b}$$

$$\Delta\rho_Y = F_y(\rho^n, v_y^n, \Delta y, \Delta t) \tag{3.13c}$$

$$\Delta\rho_Z = F_z(\rho^n, v_z^n, \Delta z, \Delta t) \tag{3.13d}$$

$$\Delta\rho_S = \Delta t\ S^n(\rho^n, \vec{v}^n, t^n, x, y, z) \tag{3.13e}$$

The simplistic way of looking at the problem is that, at the end of a time step iteration, the total update of lets say the conserved variable ρ can be expressed as

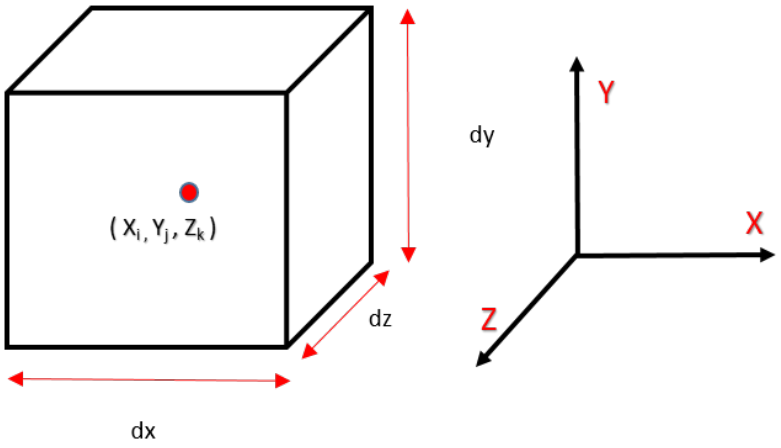

Figure 3.1: A fluid cell in XYZ coordinate system.

the sum of its updates due to the flow along the 3 coordinate axes in X, Y and Z and also due to the source/sink contribution within the computational cell. This assumption is valid because flow along each direction and the influx or outflux in a cell due to sink or source terms is independent of the others. This approach is also known as operator splitting. Hence we can split equation (3.13a) into four separate difference equations (3.13b, 3.13c, 3.13d, 3.13e).

We can write the final result after a full three dimensional time step as

$$\rho^{n+1} - \rho^{n} = \Delta\rho_X + \Delta\rho_Y + \Delta\rho_Z + \Delta\rho_S. \tag{3.14}$$

We still need effective algorithms to compute the updates in $\rho = \{\Delta\rho_X, \Delta\rho_Y, \Delta\rho_Z\}$ from the fluxes, on the right hands side of equation (3.13a). The source term is time integrated and added to the result of the updates from fluxes, to get the total update in ρ for the time step Δt. (3.14).

3.3 Sharp and Smooth Transport Algorithm (SHASTA)

SHASTA was one of the first flux correction algorithms which gave good results in terms shock resolution [74]. Its essential philosophy was to give a high order solution in smooth regions devoid of shock, (2^{nd} order in Δx and Δt in the original work) however on encountering shocks it would try to prevent growth of new extrema, by sacrificing accuracy. It accomplishes this objective by doing non-linear flux based corrections, which give a lower order but stable solution in regions of shocks.

3.3.1 Transport Stage

The first step in SHASTA is the transport stage. The cell centered values are interpolated linearly as shown in Figure 3.2a. After a time Δt each grid point moves forward by $v_j \Delta t$. Each grid point moves according to the velocity at that point, however it is obvious that the following condition be met for a positive solution

$$\left| v_j \, \frac{\Delta t}{\Delta x} \right| < \frac{1}{2} \tag{3.15}$$

After a time of Δt each cell center would have moved to new positions dictated by the velocity at that point. However the material between two neighboring cells would have been conserved. Hence the height of each trapezoid will be scaled in proportion to how much its base on the X-axis has shrunk or expanded. Hence we will have two peak values (for instance ρ_{1j} , ρ_{2j} in the j^{th} cell Figure (3.2)) for the variable ρ within each cell. Now we can find the updated transport value $\tilde{\rho}_j^{n+1}$ inside each cell by using linear interpolation between neighboring cells and recalculating the area of the new shaded region within the cell. This computation gives us the result

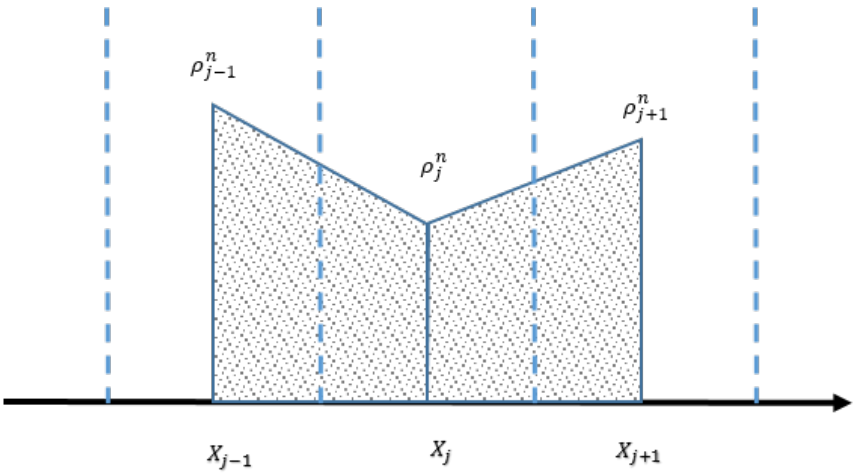

(a) at t^n

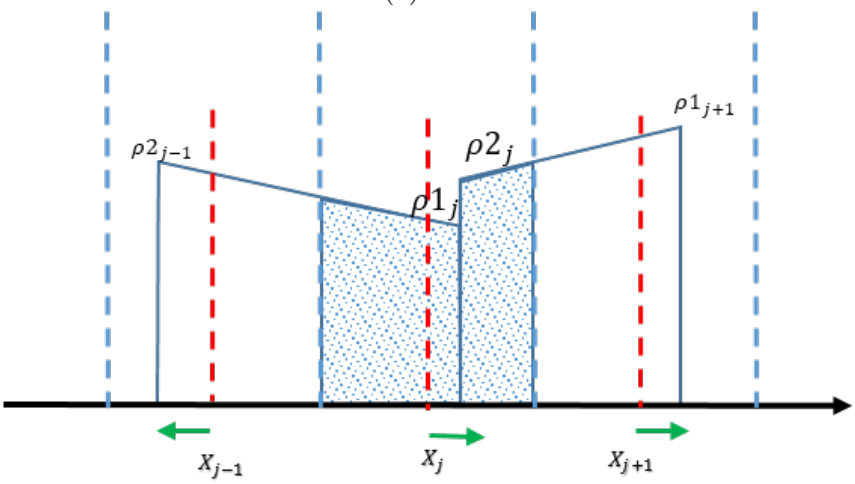

(b) at $t^n + \Delta T$

Figure 3.2: Shasta transport stage.

$$\tilde{\rho}_j^{n+1} = \frac{1}{2}Q_-^2(\rho_{j-1}^n - \rho_j^n) + \frac{1}{2}Q_+^2(\rho_{j+1}^n - \rho_j^n) + (Q_+ + Q_-)\rho_j^n$$

$$Q_\pm = \frac{(\frac{1}{2} \mp v_j \frac{\Delta t}{\Delta x})}{1 \pm (v_{j\pm1} - v_j)\frac{\Delta t}{\Delta x}}. \tag{3.16}$$

3.3.2 Flux Correction

Equation (3.16) carries substantial diffusion in its solution and for zero velocity flow, it reduces to the diffusion equation.

$$\tilde{\rho}_j^{n+1} = \rho_j^n - \frac{1}{8}(\rho_{j+1}^n - 2\rho_j^n + \rho_{j-1}^n) \tag{3.17}$$

The diffusive properties of the solution (3.16) can be canceled by introducing anti-diffusive fluxes of the transported solution.

$$f_{j\pm\frac{1}{2}} \equiv \pm\frac{1}{8}(\tilde{\rho}_{j\pm1}^{n+1} - \tilde{\rho}_j^{n+1}) \tag{3.18}$$

While applying these anti-diffusive fluxes to the transport solution it is essential that no new maxima or minima should be generated in the solution. The prescription of selectively applying these anti diffusive fluxes to the transport solution was the key point of the SHASTA algorithm. The corrected fluxes are

$$f_{j+\frac{1}{2}}^c = \mathrm{sgn}(\Delta_{j+\frac{1}{2}}) \;\; \max(\, 0,\, \min(\, \Delta_{j-\frac{1}{2}}\, \mathrm{sgn}(\Delta_{j+\frac{1}{2}}),\, \frac{1}{8}\left|\Delta_{j+\frac{1}{2}}\right|,\, \Delta_{j+\frac{3}{2}}\;\; \mathrm{sgn}(\Delta_{j+\frac{1}{2}})\,)\;\;) \tag{3.19}$$

where

$$\Delta_{j+\frac{1}{2}} \equiv \tilde{\rho}_{j+1}^{n+1} - \tilde{\rho}_j^{n+1} \tag{3.20}$$

This flux correction essentially compares three consecutive slopes between neighboring points of the transported solution and checks for maxima or minima. The anti-diffusive flux is not applied if there is a new maxima/minima growing in the solution. With the corrected anti diffusive flux of equation (3.19) computed, the final value of ρ_j after the time step is given by

$$\rho_j^{n+1} = \tilde{\rho}_j^{n+1} - f^c_{j+\frac{1}{2}} + f^c_{j-\frac{1}{2}} \tag{3.21}$$

This result (3.21) is second order in Δx. For time integration one can use schemes like RK2, RK3 or RK4. SHASTA and its multidimensional extension proposed by Zalesak [78] has been used in our field [27, 28, 41] with good success.

3.4 Kurganov and Tadmor (KT) Central Scheme

The KT scheme [75] is a finite volume scheme of the MUSCL (Monotonic Upstream-Centered Scheme for Conservation Laws) type [79]. The KT scheme can be used to solve conservation equations written down in flux form.

$$\partial_t \rho + \partial_x (F_x) = 0 \tag{3.22}$$

Unlike the SHASTA scheme it is not necessary for the equations to be in precisely the form of equation (3.10). The quantities inside the space derivatives are interpreted as the flux flowing along that particular direction. This interpretation comes from applying the *divergence theorem*. Let us look at the three dimensional conservation law

$$\partial_t \rho + \boldsymbol{\nabla} \cdot \vec{F}(\rho) = 0 \ . \tag{3.23}$$

Let's integrate over a finite volume (V_j) of the computational cell j.

$$\partial_t \int_{V_j} \rho \, dV + \int_{V_j} (\boldsymbol{\nabla} \cdot \vec{F}(\rho)) \, dV = 0 \tag{3.24}$$

Now we use the divergence theorem to change the volume integral in the second term to a surface integral.

$$\partial_t \int_{V_j} \rho \, dV + \oint_S (\vec{F}(\rho) \cdot \vec{n}) \, dS = 0 \tag{3.25}$$

Where $\vec{n}$ is a vector normal to the surface S. For computational purposes we assume that the value at the center of a cell is the average of that entire cell. Hence the volume integral of ρ over the entire computational cell can be written as the product of the cell center value of ρ *i.e.* ρ_j and the volume of the cell V_j.

$$\int_{V_j} \rho \, dV = V_j \rho_j \tag{3.26}$$

Using this in equation (3.25) we get

$$V_j \frac{\partial \rho_j}{\partial t} + \oint_S (\vec{F}(\rho) \cdot \vec{n}) \, dS = 0 \tag{3.27}$$

and thus with discretized time step

$$\frac{\rho_j^{n+1} - \rho_j^n}{\Delta t} = -\frac{1}{V_j} \oint_S (\vec{F}(\rho) \cdot \vec{n}) \, dS \tag{3.28}$$

We simplify the right hand side for the one dimensional case

$$\frac{\rho_j^{n+1} - \rho_j^n}{\Delta t} = -\frac{1}{\Delta x} \oint_{x_j - \frac{\Delta x}{2}}^{x_j + \frac{\Delta x}{2}} F_x(\rho) \, dS \tag{3.29}$$

The surface integral of $F_x(\rho)$ along the x-axis equals evaluating it at $x_j - \frac{\Delta x}{2}$ and $x_j + \frac{\Delta x}{2}$, *i.e.*

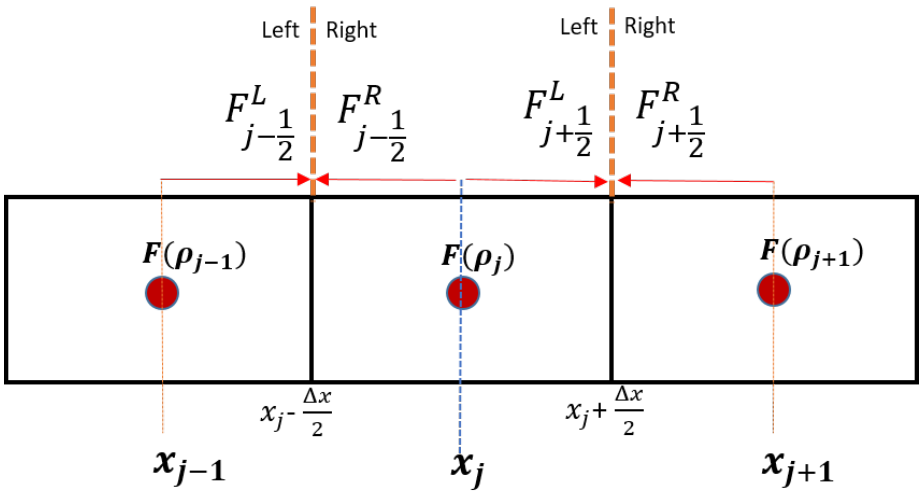

Figure 3.3: Reconstruction of central flux to boundary in a fluid cell.

$$\rho_j^{n+1} = \rho_j^n - \frac{\Delta t}{\Delta x} \left(F(\rho_{j+\frac{1}{2}}) - F(\rho_{j-\frac{1}{2}}) \right) \tag{3.30}$$

here $F(\rho_{j+\frac{1}{2}})$ is the flux evaluated at boundary $x_{j+\frac{1}{2}} = x_j + \frac{\Delta x}{2}$ and $F_{j-\frac{1}{2}}$ is the flux evaluated at boundary $x_{j-\frac{1}{2}} = x_j - \frac{\Delta x}{2}$. Equation (3.31) is the general equation for any finite volume scheme. We can also see similarity with equation (3.14), as $\Delta\rho_X$ would be given by $\big(- \frac{\Delta t}{\Delta x}(F(\rho_{j+\frac{1}{2}}) - F(\rho_{j-\frac{1}{2}}))\big)$.

The two key aspects of using (3.30) are **a)** the choice of how to construct fluxes of the boundaries of cells from fluxes at the center, and **b)** the process of finding the total flux at each boundary between two neighbor cells. Figure 3.3 clarifies the situation. The so-called reconstruction scheme will give us reconstructed values of fluxes both at the right and left of any cell boundary, for example $F^R_{j+\frac{1}{2}}$, $F^L_{j+\frac{1}{2}}$ for the boundary located at $x_{j+\frac{1}{2}}$. These values need not be same (due to discontinuities). In order to find the total flux at a boundary we need to make a reasonable choice from the right and left-hand fluxes. We use the WENO scheme for reconstruction and the KT scheme for the computation of final flux needed by equation (3.30).

3.4.1 WENO Reconstruction

For our hydro code we have used the 5^{th} order WENO scheme for reconstructing the centered average fluxes to the boundary walls of the computational cell. WENO stands for Weighted Essentially Non-Oscillatory scheme. In this scheme we use cell average values of flux or primary variables and reconstruct them at the boundary of cells.

The WENO scheme is an improvement over the older ENO scheme [80]. For an n^{th} order ENO scheme one needs $2n-1$ points. As we previously saw with SHASTA, the order of scheme is only guaranteed for smooth regions. If a shock is being resolved in a region, then the order of the solution is reduced to prevent unphysical ripples in the solution. An ENO scheme of order n may use a stencil up to n points (hence n^{th} order). The crux of the ENO scheme is in selecting an adaptive stencil based on the profile being resolved. For smooth regions all the n points will be used.

In the WENO scheme, k candidate stencils are considered. These k stencils each covering k neighboring cells, altogether span $2k-1$ adjacent cells. In smooth regions WENO will use information from all the $2k-1$ cells and give a $(2k-1)^{th}$ order solution. So for our need of a 5^{th} order WENO scheme we need three $k=3$ stencils $\{S_1, S_2, S_3\}$, with each stencil enclosing 3 neighboring cells and in total covering 5 cells. (Figure 3.4)

We will give the recipe for the WENO reconstruction scheme of centered flux F_j at cell centered at X_j. After the reconstruction we should arrive at $F^L_{j+\frac{1}{2}}$ and$F^R_{j-\frac{1}{2}}$.

Here the three stencils include points,

$$S_1 = \{X_{j-2}, X_{j-1}, X_j\},\ S_2 = \{X_{j-1}, X_j, X_{j+1}\},\ S_3 = \{X_j, X_{j+1}, X_{j+2}\} \qquad (3.31)$$

Each of these three stencils will give a contribution to the reconstructed flux at

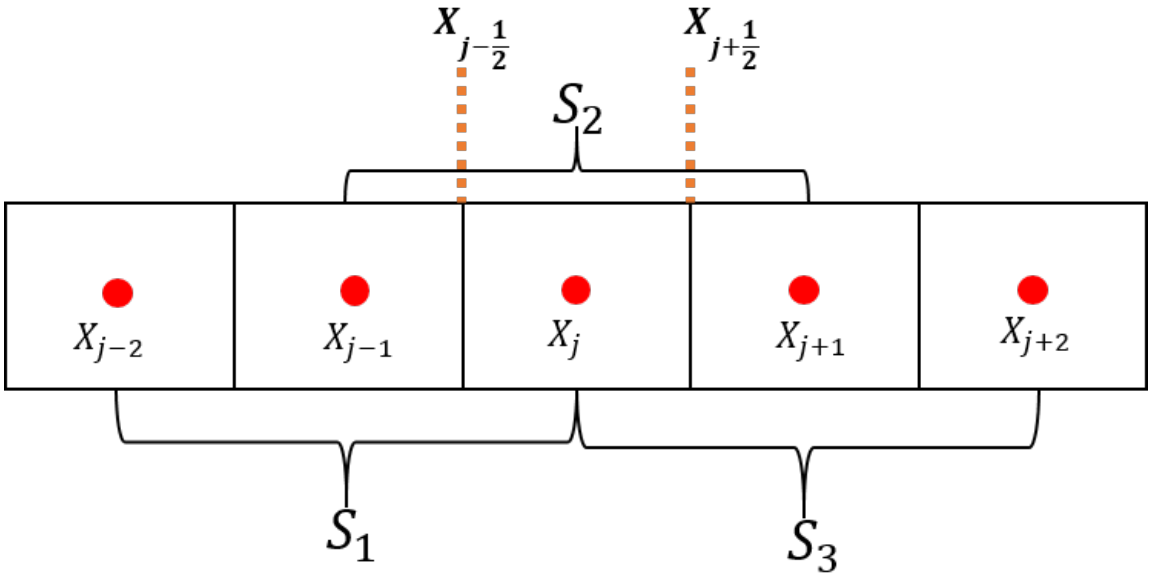

Figure 3.4: Stencils for the WENO scheme.

$X_{j+\frac{1}{2}}$. The WENO scheme assigns weights to the reconstructed fluxes from each stencil $f^{S_1}_{j+\frac{1}{2}}$, $f^{S_2}_{j+\frac{1}{2}}$ and $f^{S_3}_{j+\frac{1}{2}}$.

$$F^L_{j+\frac{1}{2}} = w_1\, f^{S_1}_{j+\frac{1}{2}} + w_2\, f^{S_2}_{j+\frac{1}{2}} + w_3\, f^{S_3}_{j+\frac{1}{2}} \tag{3.32}$$

Here $\sum_{k=1}^{3} w_k = 1$. Reconstructed third order fluxes from each stencil are given by

$$f^{S_1}_{j+\frac{1}{2}} = \frac{1}{3}F(\rho_{j-2}) - \frac{7}{6}F(\rho_{j-1}) + \frac{11}{6}F(\rho_j) \tag{3.33a}$$

$$f^{S_2}_{j+\frac{1}{2}} = -\frac{1}{6}F(\rho_{j-1}) + \frac{5}{6}F(\rho_j) + \frac{1}{3}F(\rho_{j+1}) \tag{3.33b}$$

$$f^{S_3}_{j+\frac{1}{2}} = \frac{1}{3}F(\rho_j) - \frac{5}{6}F(\rho_{j+1}) - \frac{1}{6}F(\rho_{j+2}) \tag{3.33c}$$

The essential component of the scheme is the calculation of the weights $\{w_1, w_2, w_3\}$.

These weights give a 5^{th} order solution in the smooth region and lower order solution in shocks. These weights also include smoothing effects to the final solution, which keeps the solution non-oscillatory. These weights are given by

$$w_i = \frac{\tilde{w}_i}{\sum_{k=1}^{3} \tilde{w}_k}, \quad \tilde{w}_k = \frac{\gamma_k}{(\epsilon + \beta_k)^2} \tag{3.34}$$

The weights γ_k are given by

$$\gamma_1 = \frac{1}{10}, \quad \gamma_2 = \frac{3}{5}, \quad \gamma_3 = \frac{3}{10} \tag{3.35}$$

and the smoothness indicators β are given by

$$\beta_1 = \frac{13}{12}(F(\rho_{j-2}) - 2F(\rho_{j-1}) + F(\rho_j))^2 + \frac{1}{4}(F(\rho_{j-2}) - 4F(\rho_{j-1}) + 3F(\rho_j))^2 \tag{3.36a}$$

$$\beta_2 = \frac{13}{12}(F(\rho_{j-1}) - 2F(\rho_j) + F(\rho_{j+1}))^2 + \frac{1}{4}(F(\rho_{j-1}) - F(\rho_{j+1}))^2 \tag{3.36b}$$

$$\beta_3 = \frac{13}{12}(F(\rho_j) - 2F(\rho_{j+1}) + F(\rho_{j+2}))^2 + \frac{1}{4}(3F(\rho_j) - 4F(\rho_{j+1}) + F(\rho_{j+2}))^2 \tag{3.36c}$$

The parameter ϵ is used to prevent the denominator from becoming 0. We set it to 10^{-6} in our code. Now we have everything we need to compute $F^L_{j+\frac{1}{2}}$. The recipe for $F^R_{j-\frac{1}{2}}$ is mirror symmetric to what we did earlier for $F^L_{j+\frac{1}{2}}$.

Using this process we can reconstruct all fluxes, velocities and conserved variables to each boundary between adjacent cells. Now every such boundary in X, Y and Z direction would have two different values coming from the cell on its left and right side. The KT scheme can now be employed to find the final values for total fluxes at each boundary using these left and right values.

3.4.2 The KT Recipe For Total Flux

The Kurganov and Tadmor [75] (KT) algorithm is a finite volume MUSCL [79] (Monotonic Upstream-Centered Scheme for Conservation Laws) scheme which can provide accurate solutions to hyperbolic partial differential equations. Other research groups have already used the KT algorithm to solve hydro (notably Schenke *et.al* in [39]). Our approach of using KT algorithm with a better 5^{th} order smooth reconstruction of WENO and a stable third order time integration of TVD-RK3 gives excellent results in tests which we will present in next chapter.

As we saw with the reconstruction step, at any interface $x_{j+\frac{1}{2}}$ we will have left $F^L_{j+\frac{1}{2}}$ and right $F^R_{j+\frac{1}{2}}$ values. These values could result in discontinuities at that boundary. KT algorithm uses a staggered grid approach and computes maximum local propagation speed at the interface boundary, in order to restrict the propagation of discontinuities to the cell centers. We will quote the final results for the KT scheme, please refer the original paper [75] and also [39] for detailed derivation.

The total flux is given by

$$F_{j\pm\frac{1}{2}} = \frac{F^R_{j\pm\frac{1}{2}} + F^L_{j\pm\frac{1}{2}}}{2} - a_{j\pm\frac{1}{2}}\frac{\rho^R_{j\pm\frac{1}{2}} - \rho^L_{j\pm\frac{1}{2}}}{2} \tag{3.37}$$

Here, $a_{j\pm\frac{1}{2}}$ is the maximum absolute value of all the eigenvalues of both the left and right flux Jacobian matrices at $x_j \pm \frac{\Delta x}{2}$ *i.e.*

$$a_{j\pm\frac{1}{2}} = Max\left(\tilde{\rho}\left(\frac{\partial F^R_{j\pm\frac{1}{2}}}{\partial\rho}\right), \tilde{\rho}\left(\frac{\partial F^L_{j\pm\frac{1}{2}}}{\partial\rho}\right)\right) \tag{3.38}$$

Here $\tilde{\rho}(F)$ is the spectral radius of the square matrix F. The spectral radius of a square matrix is the maximum of the magnitude of all Eigenvalues. This completes the calculation of the fluxes needed for equation (3.30).

3.5 Time Integration

We see that the KT algorithm with WENO reconstruction computes spatial derivatives with an accuracy of 5th order in Δx. But from our main equations we can see that we also have source terms, over which we need to do time integration. Our conservative equation (3.23) with source term looks like.

$$\partial_t \rho + \boldsymbol{\nabla} \cdot \vec{F}(\rho) = S(\rho) \tag{3.39}$$

We are using the third order Total Variation Diminishing Runge-Kutta 3 (TVD RK3) [81, 82] algorithm to perform the time integration. Loosing the coordinate indices's, The semi-discrete form of equations can be succinctly written in a general form for any cell as

$$\partial_t \rho = f(t^n, \rho^n_{i,j,k}). \tag{3.40}$$

Here, i, j and k are the spatial indices in x, y and z directions respectively of the cell. We are computing the right hand side of this equation at current time t^n. Let us remember that this right hand side already includes the fluxes calculated with the KT scheme. Instead of simply doing a first order integration $\rho^{n+1} = \rho^n + \Delta t\ f(t^n, \rho^n)$, we now intend to advance from ρ^n to ρ^{n+1} using the TVD RK3 integration which gives a 3^{rd} order in time solution. Losing the spatial indices, the equations are

$$\rho^1 = \rho^n + \Delta t f(t^n, \rho^n) \tag{3.41a}$$

$$\rho^2 = \frac{3}{4}\rho^n + \frac{1}{4}\rho^1 + \frac{1}{4}\Delta t f(t^n + \Delta t, \rho^1) \tag{3.41b}$$

$$\rho^{n+1} = \frac{1}{3}\rho^n + \frac{2}{3}\rho^2 + \frac{2}{3}\Delta t f(t^n + \frac{\Delta t}{2}, \rho^2) \tag{3.41c}$$

The accuracy improves because we use contributions from intermediate partial time steps to complete the full time step.

3.6 Multi-Dimensional Root Finding

Equation (3.9) gives our list of variables. Using the scheme we have developed in the previous sections we can advance all of these 10 variables by a single time step from τ to $\tau + \Delta\tau$. However, the equations are phrased directly in terms of the variables in $\vec{\rho}$, and not in terms of the more physical variables local rest frame energy density ϵ , pressure P and velocities (v_x, v_y and v_η). We need these quantities to compute the fluxes, source terms etc. in the computations of future time step.

So our problem is – given that we know $T^{\tau\tau}$, $T^{\tau x}$, $T^{\tau y}$, $T^{\tau\eta}$, π^{xx}, π^{yy}, π^{xy}, $\pi^{x\eta}$, $\pi^{y\eta}$ and Π in a fluid cell, how can we numerically compute the local energy density and velocity of the cell. Finding pressure is straight forward after that, using the equation of state. The solution can be found by considering the complete energy momentum tensor.

$$T^{\mu\nu} = \big(\epsilon + P(\epsilon)\big)u^\mu u^\nu - P(\epsilon)g^{\mu\nu} + \Delta^{\mu\nu}\Pi + \pi^{\mu\nu} \tag{3.42}$$

The trace of the energy momentum tensor is given by

$$\mathrm{Tr}(T^{\mu\nu}) = T^{\mu\nu}g_{\mu\nu} = \epsilon - 3P(\epsilon) + \Pi \tag{3.43}$$

On the other hand, introducing the variables in $\vec{\rho}$ into equation (3.42) gives

$$T^{\mu\nu} = \begin{bmatrix} T^{\tau\tau} & T^{x\tau} & T^{y\tau} & T^{\eta\tau} \\ T^{x\tau} & \pi^{xx} + P(\epsilon) - \Pi + (u^x)^2\delta & \pi^{xy} + u^x u^y \delta & \pi^{x\eta} + u^x u^\eta \delta \\ T^{y\tau} & \pi^{xy} + u^x u^y \delta & \pi^{yy} + P(\epsilon) - \Pi + (u^y)^2\delta & \pi^{y\eta} + u^y u^\eta \delta \\ T^{\eta\tau} & \pi^{x\eta} + u^x u^\eta \delta & \pi^{y\eta} + u^y u^\eta \delta & X \end{bmatrix} \tag{3.44}$$

Here we use the symbol δ for brevity and it stands for

$$\delta = \epsilon + P(\epsilon) - \Pi \tag{3.45}$$

and X is determined by the trace equation (3.43)

$$X = \frac{T^{\tau\tau} - \Big(\epsilon - P(\epsilon) + \Pi + \pi^{xx} + \pi^{yy}\Big) - \Big((u^x)^2 + (u^y)^2\Big)^2\delta}{\tau^2} \tag{3.46}$$

Now that we have used the trace equation (3.43) and symmetry of $T^{\mu\nu}$, and now the only unknowns we are left with are ϵ, $P(\epsilon)$, u^x, u^y and u^η. Considering that Pressure, $P(\epsilon)$ depends on ϵ through the equation of state we are left with four unknowns ϵ, u^x, u^y and u^η. We need another set of 4 equations to solve for these unknowns. For that let's start by contracting $T^{\mu\nu}$ from equation (3.42) with u_ν, this gives us

$$T^{\mu\nu}u_\nu = \big(\epsilon + P(\epsilon)\big)u^\mu u^\nu u_\nu - P(\epsilon)g^{\mu\nu}u_\nu + \Delta^{\mu\nu}u_\nu\Pi + \pi^{\mu\nu}u_\nu \quad . \tag{3.47}$$

Now we use the relations $u^\nu u_\nu = 1$, $\Delta^{\mu\nu}u_\nu = 0$ and $\pi^{\mu\nu}u_\nu = 0$ to arrive at

$$T^{\mu\nu}u_\nu = \epsilon\, u^\mu \quad . \tag{3.48}$$

The four velcoity u_ν can be written in terms of u^x, u^y and u^η as

$$u_\nu = \{\gamma, -u^x, -u^y, -u^\eta\} \tag{3.49}$$

where γ is given by

$$\gamma = \sqrt{1 + (u^x)^2 + (u^y)^2 + \tau^2(u^\eta)^2} \tag{3.50}$$

Using $T^{\mu\nu}$ from (3.42), X from (3.46) and u_ν from (3.49) and substituting in equation (3.50) we can simplify to the following 4 non-linear equations. (The non-linearity comes from γ and possibly the equation of state.)

$$\gamma(T^{\tau\tau} - \epsilon) - u^x T^{x\tau} - u^y T^{y\tau} - \tau^2 u^\eta T^{\eta\tau} = 0 \tag{3.51}$$

$$\gamma(T^{x\tau}) - u^x\big((1 + (u^x)^2)\delta - \pi^{xx}\big) - u^y\big(u^x u^y \delta - \pi^{xy}\big) - \tau^2 u^\eta\big(u^x u^\eta \delta + \pi^{x\eta}\big) = 0 \tag{3.52}$$

$$\gamma(T^{y\tau}) - u^x\big(u^x u^y \delta - \pi^{xy}\big) - u^y\big((1 + (u^y)^2)\delta - \pi^{yy}\big) - \tau^2 u^\eta\big(u^y u^\eta \delta + \pi^{y\eta}\big) = 0 \tag{3.53}$$

$$\gamma(T^{\eta\tau}) - u^x\pi^{x\eta} - u^y\pi^{y\eta} + u^\eta\Big(\pi^{xx} + \pi^{yy} + \Pi - P(\epsilon) - T^{\tau\tau}\Big) = 0 \tag{3.54}$$

We use the *gsl_multiroot_fsolver_dnewton* algorithm (Discrete Newton's) within the GSL library [83] to solve these 4 equations iteratively. The library requires us to provide the Jacobian terms (with respect to ϵ , u^x, u^y, u^η) of the equations (3.51) to (3.54), and an initial guess for ϵ , u^x, u^y, u^η. For the initial guess we provide values

from the previous time step.

3.7 3+1D Parallelization and Code Details

In Fig. 3.5 we can see a visualization of what happens when we parallelize our code in the spatial domain. The goal is to give each processor a sub-domain of the space, where it can solve the equations independently. However due to the nature of the algorithms employed we know that to find the spatial gradient at any point (e.g. for the WENO scheme) we need to get information on the neighboring few points. Hence each processor cannot simply do computations within its domain without interacting with neighbors.

We have used an MPI based parallelization where we split the transverse plane into $m \times n$ tiles in the X-Y-plane, each of which will be assigned to one processor. In Fig. 3.5, $m = n = 3$. For the process number 5 at the center (marked in yellow), one can see there will be a pseudo-boundary region (shaded in dark blue) where we need information from neighboring processes (numbered 2, 4, 6 and 8) in order to compute the gradients and evolve the equation. MPI based parallelization gives us routines like *MPI_Send*, *MPI_Recv* for inter process communication. This has to be done at the end of every time iteration. For simplicity we chose to not decompose space in the η direction. In our runs we have run the hydro code with up to 100 processors *i.e.* $m = 10$ and $n = 10$ and we have found an almost linear speedup with this parallelization.

Inter-process communications are also needed when we have to compute some quantity globally, like the maximum temperature, or the maximum velocity in the grid. Such computations can be done using *MPI_Reduce* calls of the MPI library.

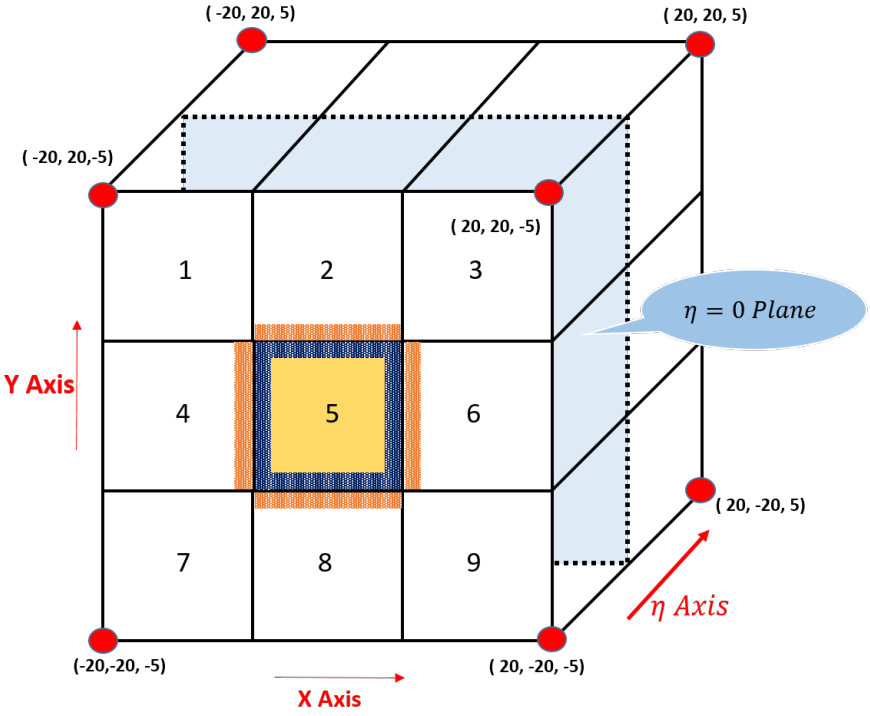

Figure 3.5: The computational grid using 9 processors spanning a space from -20 fm to 20 fm in transverse plane and from -5 to 5 in η direction. In our code we use spatial domain decomposition only along the X and Y axis. The η direction has no decomposition. The $\eta = 0$ plane has been shaded light blue to emphasize that this is a three-dimensional computational grid.

3.7.1 Boundary Conditions

The computational grid also has 6 boundary faces, for instance in Fig. 3.5 the boundaries are the planes along $x = -20$, $x = 20$, $y = -20$, $y = 20$, $\eta = -5$ and $\eta = 5$. We deal with the boundary, which is typically far removed from any physical region by holding few a shadow cells which have the same value of primary variables ($\tau T^{\tau\tau}, \pi^{xx}$.. etc), as the nearest cell on the grid. Such a boundary condition allows for free flow of material to the outside of the grid. It is appropriate if the system is either translationally invariant perpendicular to the wall, or if the energy density at the wall is negligibly small.

3.7.2 Parallel File Writing

Writing out space time information for quantities of interest is essential for hydro. Not only are these output files large, but disk access slows down the run time. In our parallelization we write files out in parallel and in binary format. This gave us a compression of file sizes in comparison to writing out in ASCII. Considerable speedup also happens when many processes are allowed to write out different chunks of a file to a single binary file. We have routines like *MPI_Write* for parallel binary mode writing to disk in the MPI library.

4. TESTS AND RESULTS

In this chapter we will look into some of the standard benchmarks to test our hydro package. To begin with we had started with ideal hydrodynamics in $1+1$ dimensions in the $\{t, x, y, z\}$ coordinates. Standard tests like the Sod shock tube and the Bjorken boost invariance [84] were conducted. We then moved to the hyperbolic coordinates $\{\tau, x, y, \eta\}$, in which we implemented our $3+1$ viscous hydrodynamics.

The tests we will look at in this chapter in $\{t, x, y, z\}$ coordinates are

- 1+1 Ideal Sod Test (sub-section 4.2.1) ,
- 2+1 Ideal Sod Test (sub-section 4.2.2) ,
- 1+1 Shear Viscous Sod Test (sub-section 4.2.3),

and then in $\{\tau, x, y, \eta\}$ coordinates are

- 2+1 Boost invariant fluctuating initial conditions (sub-section 4.3.1),
- 3+1 Boost invariant Navier-Stokes approximation test (sub-section 4.3.2),
- 3+1 Boost invariant Bulk Visocus analytical test (sub-section 4.3.3),
- 2+1 Ideal Gubser test (sub-section 4.3.4),
- 2+1 Shear viscous Gubser semi-analytical test (sub-section 4.3.5),
- 2+1 Shear viscous Gubser in cold-plasma limit analytical test (sub-section 4.3.6),
- 3+1 Non-boost invariant setup with rapidity cutoff in energy density (sub-section 4.3.7),

- 3+1 Non-boost invariant setup simulating $V_z = 0$ (sub-section 4.3.8).

4.1 Equation of State and Vorticity

For all the computational tests done in this chapter we have considered the relativistic free gas, for which the energy density ϵ, as a function of temperature is given by

$$\epsilon = 3\left(g_b + \frac{7}{8}g_f\right)\frac{\pi^2}{90}T^4. \tag{4.1}$$

Here, g_b is the degeneracy for bosons, which are gluons in this case. And g_f is the degeneracy for fermions, which are quarks in this case. For the computational simulations we have considered 8 color charges for gluons and 2.5 flavors for the 3 quark colors. This gives us

$$g_b = 2_{helicity} \times 8_{colour} = 16 \tag{4.2a}$$

$$g_f = 2_{spin} \times 2_{q,\bar{q}} \times 3_{colour} \times 2.5_{flavor} = 30 \ . \tag{4.2b}$$

The energy density ϵ becomes

$$\epsilon = 42.25 \ \frac{\pi^2}{30}\ T^4 \ , \tag{4.3}$$

and the fluid pressure p, given by the equation of state for a relativistic conformal fluid is

$$p = \frac{\epsilon}{3} \ . \tag{4.4}$$

For all tests in this chapter we have turned the vorticity term $\pi^{\phi(\mu}\Omega^{\nu)}{}_{\phi}$ in the

Israel Stewart equation 2.42 for shear stress to zero. We enable the vorticity term when dealing with CGC based initial conditions which we will discuss in chapter 5.

4.2 Hydrodynamics Tests in $\{t, x, y, z\}$ Coordinates

During my master's work we tested a $1+1$ dimension set up where we took the classical Sod tube test and solved the relativistic inviscid hydro equations. This test was done in $\{t, x, y, z\}$ coordinates so the equations we solved are different from but easily related to the equations we worked out in hyperbolic coordinates in chapter 2. Here we will simply state the equations in $\{t, x, y, z\}$ coordinates for the $1+1$ dimensional setup.

$$\partial_t T^{tt} + \partial_x T^{tx} + \partial_y T^{ty} + \partial_z T^{tz} = 0 \tag{4.5a}$$

$$\partial_t T^{xt} + \partial_x T^{xx} + \partial_y T^{xy} + \partial_z T^{xz} = 0 \tag{4.5b}$$

$$\partial_t T^{yt} + \partial_x T^{yx} + \partial_y T^{yy} + \partial_z T^{yz} = 0 \tag{4.5c}$$

$$\partial_t T^{zt} + \partial_x T^{zx} + \partial_y T^{zy} + \partial_z T^{zz} = 0 \tag{4.5d}$$

We can either use the KT algorithm on the above equations as they are or we can rewrite the equations in conservative form (like the form of equation 2.42, 2.43) for the SHASTA algorithm. For sake of completion we will quote the final result of the rearranged equations used by SHASTA for the viscous case. To arrive at ideal equations of same form, we can just set the viscous terms $\pi^{\mu\nu}$ and Π to zero.

$$\partial_t T^{tt} + \partial_x(v_x T^{tt}) + \partial_y(v_y T^{tt}) + \partial_z(v_z T^{tt}) = S_0 \tag{4.6a}$$

$$\partial_t T^{xt} + \partial_x(v_x T^{xt}) + \partial_y(v_y T^{xt}) + \partial_z(v_z T^{xt}) = S_1 \tag{4.6b}$$

$$\partial_t T^{yt} + \partial_x(v_x T^{yt}) + \partial_y(v_y T^{yt}) + \partial_z(v_z T^{yt}) = S_2 \tag{4.6c}$$

$$\partial_t T^{zt} + \partial_x(v_x T^{zt}) + \partial_y(v_y T^{zt}) + \partial_z(v_z T^{zt}) = S_3 \tag{4.6d}$$

Here the source terms S_0, S_1, S_2 and S_3 are

$$S_0 = -\partial_x(v_x(P - \Pi - \pi^{tt}) + \pi^{tx}) - \partial_y(v_y(P - \Pi - \pi^{tt}) + \pi^{ty}) - \partial_z(v_z(P - \Pi - \pi^{tt}) + \pi^{tz}) \tag{4.7a}$$

$$S_1 = -\partial_x(P - \Pi - v_x\pi^{xt} + \pi^{xx}) - \partial_y(-v_y\pi^{xt} + \pi^{xy}) - \partial_z(-v_z\pi^{xt} + \pi^{xz}) \tag{4.7b}$$

$$S_2 = -\partial_x(-v_x\pi^{yt} + \pi^{yx}) - \partial_y(P - \Pi - v_y\pi^{yt} + \pi^{yy}) - \partial_z(-v_z\pi^{yt} + \pi^{yz}) \tag{4.7c}$$

$$S_3 = -\partial_x(-v_x\pi^{zt} + \pi^{zx}) - \partial_y(-v_y\pi^{zt} + \pi^{zy}) - \partial_z(P - \Pi - v_z\pi^{zt} + \pi^{zz}) \ . \tag{4.7d}$$

The equations for the viscous case are the same as the previously described equations (2.42) and (2.43), with the small change that we have to set the geometrical terms coming from the covariant derivative to zero. Hence we are not repeating them again here.

4.2.1 1+1 Inviscid Sod Test

In Sod shock tube test [85], we set up the fluid along the z-axis into two different pressure zones initially. This can be thought of as realizing an invisible barrier separating the two zones at the origin $z = 0$. At $t = 0$ the invisible barrier is instantaneously removed and the fluid faces a shock at the boundary between two pressure zones.

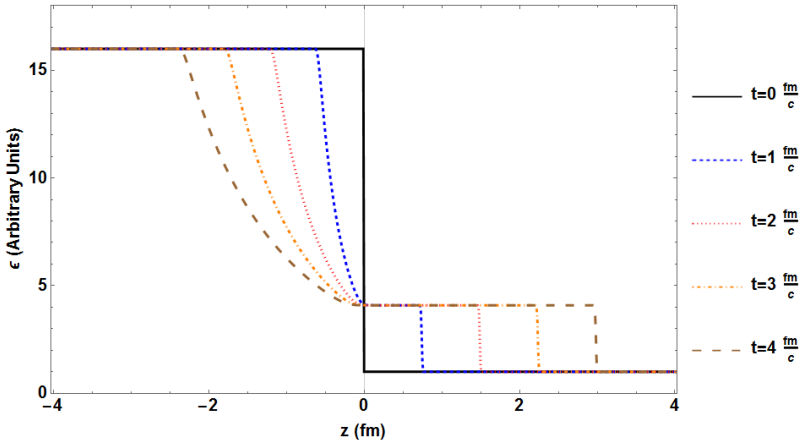

(a) Energy density ϵ versus z

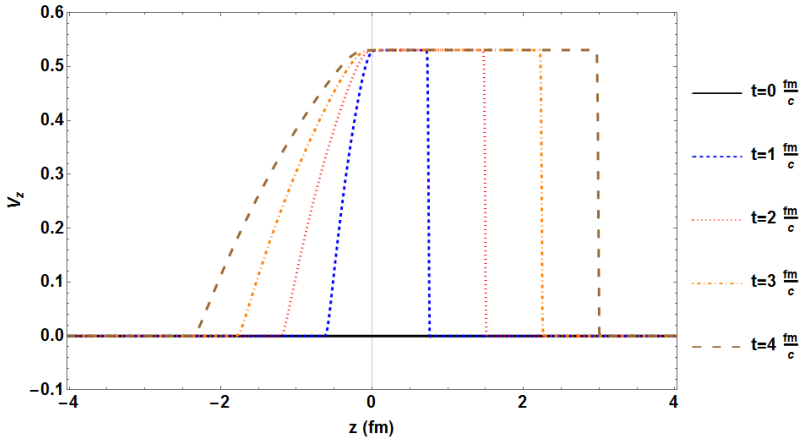

(b) Velocity V_z versus z

Figure 4.1: Sod shock tube test solved with SHASTA and RK4 time integration.

In figure 4.1a, we can see the initial energy density (black bold line) and it is given by

$$\epsilon(z, t = 0) = \begin{cases} 16 & z < 0 \\ 1 & z \geq 0 \end{cases} \tag{4.8}$$

and the initial velocity $V_z(z, t = 0) = 0$. Pressure on both sides comes from the equation of state (4.4), and we can see that the sharp shock-like pressure gradient at $z = 0$ drives the flow of fluid. As a reminder, in the $1 + 1$ case we are only solving the two equations, (4.5a) and (4.5d). This test has been previously studied [86] and analytical solutions were found. For our simulation the details of grid are in table 4.1 and the results are in Fig. 4.1a and Fig. 4.1b for ϵ and v_z respectively. We ran the hydro code from initial time at $t = 0$ to $t = 4$ and our results were indistinguishable from the analytical results.

Table 4.1: Grid details for inviscid Sod test.

Coordinate	Min	Max	Grid Spacing	Grid Points	Integration Scheme
z (in fm)	-4	4	0.01	801	SHASTA
time t (c)	0	4	0.004	1000	RK4

The Sod test is a good benchmark for how well a fluid simulation can deal with shocks and steep gradients.

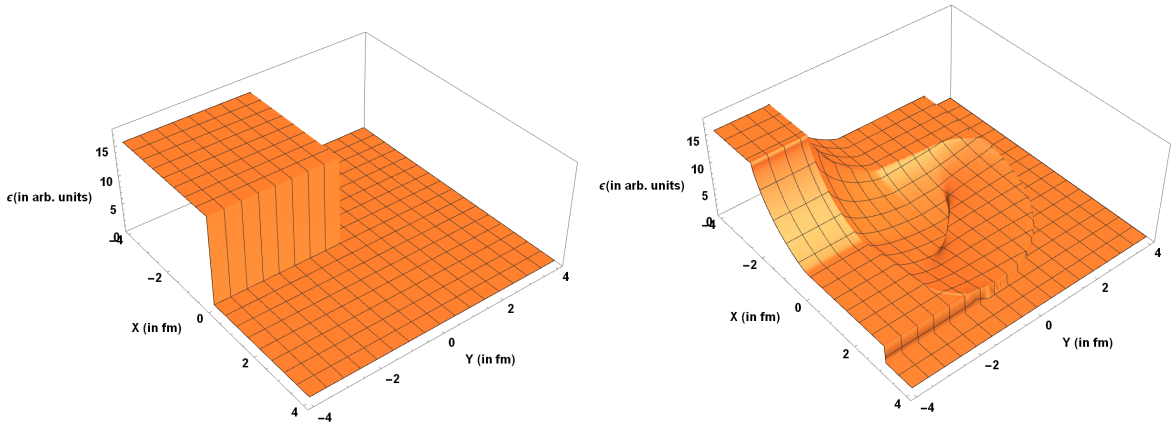

(a) Energy density ϵ in xy-plane at $t = 0$.

(b) Energy density ϵ in xy-plane at $t = 4fm/c$.

Figure 4.2: Sod shock test tube in 2+1 dimensions.

4.2.2 2+1 Ideal Sod Test

We do the same test in $2 + 1$ dimensions, with the initial condition

$$\epsilon(x, y, t = 0) = \begin{cases} 16 & x < 0 \text{ and } y < 0 \\ 1 & \text{otherwise} \end{cases} \tag{4.9}$$

The grid details for this are given in table 4.2. In Fig. 4.2b we can see the results of energy density evolution. The signatures of the $1 + 1$ D result can be seen in two of the quadrants, but the rest of the plot shows the interaction of fluids movement happening due to the combined effect of flow in x and y direction. This is a test that the operator splitting approach we took in (3.13a) resolves this interaction, in a smooth and stable fashion.

Table 4.2: Grid details for 2+1 ideal Sod test.

Coordinate	Min	Max	Grid Spacing	Grid Points	Integration Scheme
x (in fm)	-4	4	0.01	801	SHASTA
y (in fm)	-4	4	0.01	801	SHASTA
time t (c)	0	4	0.004	1000	RK4

4.2.3 1+1 Shear Viscous Sod Test

Here we perform the same Sod test of section 4.2.1 but now with non-zero shear viscosity. The shear viscous tensor looks like

$$\pi^{\mu\nu}_{rest} = \begin{bmatrix} 0 & 0 & 0 & 0 \\ 0 & \phi/2 & 0 & 0 \\ 0 & 0 & \phi/2 & 0 \\ 0 & 0 & 0 & -\phi \end{bmatrix} \tag{4.10}$$

in the local rest frame of the fluid. Since v_z is non zero, we apply a boost to it to arrive at $\pi^{\mu\nu}$ in lab frame. This is done by

$$\pi^{\mu\nu} = \Lambda^{\mu}{}_{\alpha}\, \Lambda^{\nu}{}_{\beta}\ \pi^{\alpha\beta}_{rest}\ . \tag{4.11}$$

Here, the Lorentz boost tensor is

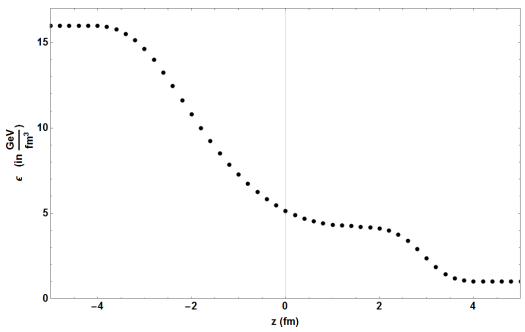

(a) Energy density ϵ versus z

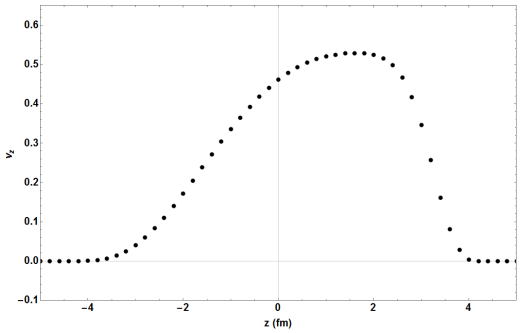

(b) Shear viscosity ϕ versus z

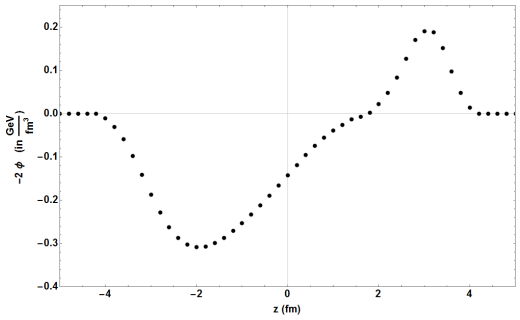

(c) Velocity v_z versus z

Figure 4.3: Sod shock tube test for viscous fluid with non-zero shear viscosity, solved with SHASTA and first order time integration.

$$\Lambda^{\mu}{}_{\nu} = \begin{bmatrix} \frac{1}{1-v_z^2} & 0 & 0 & \frac{v_z}{1-v_z^2} \\ 0 & 1 & 0 & 0 \\ 0 & 0 & 1 & 0 \\ \frac{v_z}{1-v_z^2} & 0 & 0 & \frac{1}{1-v_z^2} \end{bmatrix} \tag{4.12}$$

Now we can use $\pi^{\mu\nu}$ to solve the Israel Stewart equations like we did for the other cases. For this test the η/s ratio was set to 0.1. We choose a coarse grid (Table 4.3) to emulate test conditions similar to what as was done in [38]. Our results are shown in figure 4.3. We can see that even a small nominal shear viscosity, significantly smoothens the sharp features in the solution compared to the inviscid case. For this test we had used a $1+1$ code with SHASTA scheme.

Table 4.3: Grid details for the viscous Sod test.

Coordinate	Min	Max	Grid Spacing	Grid Points	Integration Scheme
z (in fm)	-20	20	0.2	201	SHASTA
time t (c)	0	4	0.04	100	First Order

4.3 Hydrodynamics Tests in $\{\tau, x, y, \eta\}$ Coordinates

4.3.1 Fluctuating Initial Conditions

In this test we initialize our $3+1$ hydro only in the $\eta = 0$ plane assuming boost invariance with fluctuating initial conditions provided by R. Rodriguez and generated by the Glauber Monte Carlo code GLISSANDO [87]. Details of the grid are given in table 4.4. This test should demonstrate that steeper gradients typically associated with fluctuating initial conditions are easily resolved by this code. We use the KT scheme here

Table 4.4: Grid details for fluctuating initial conditions.

Coordinate	Min	Max	Grid Spacing	Grid Points	Integration Scheme
x (in fm)	-15	14.975	0.025	1200	KT(WENO)
y (in fm)	-15	14.975	0.025	1200	KT(WENO)
time τ (c)	0.6	10.6	0.001	10000	TVDRK3

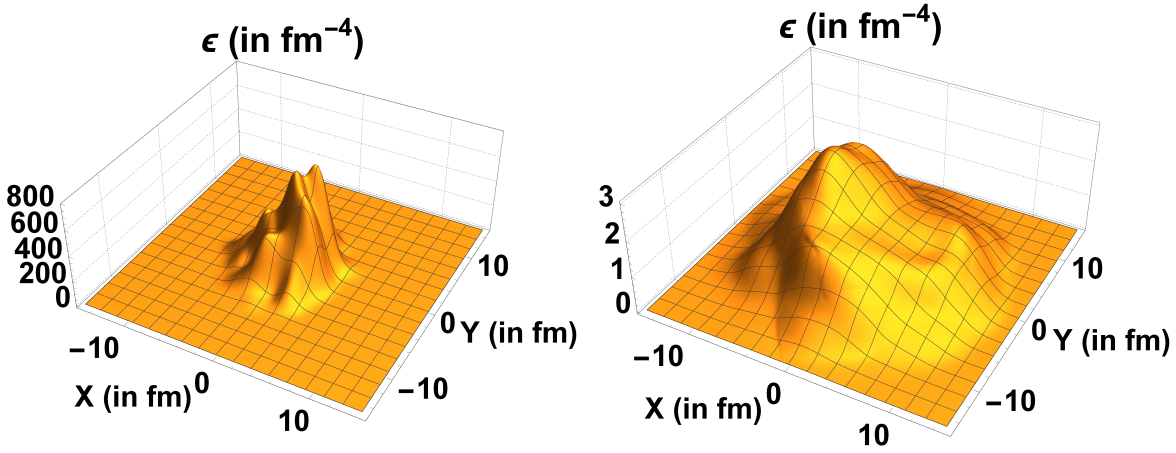

(a) ϵ in xy plane at $\tau = 0.6$ fm

(b) ϵ in xy plane at $\tau = 10.6$ fm

Figure 4.4: Fluctuating initial conditions with longitudinal boost invariance.

We run this code for 10000 TVDRK3 time steps. The initial and final three dimensional plots of energy density ϵ can be seen in figure 4.4. The schematics for temperature evolution is presented in figure 4.5. As we can that the hydro scheme is able to deal with the complex fluctuating initial conditions and cool down the system as time progresses.

4.3.2 Bjorken Test in the Navier-Stokes Limit

In this test we initialize the energy density in the entire $3+1$ D hydro grid with constant value ($\epsilon = 30$ GeV/fm^3, temperature $= 359$ MeV) and zero velocities ($u^\mu = \{1, 0, 0, 0\}$ *i.e.* $v_x = v_y = v_\eta = 0$). Considering these symmetries this system is effectively a $0+1$ system with all physical quantities invariant in three spatial dimensions and only the time evolution being a variant. The traceless shear stress tensor in $\{\tau, x, y, \eta\}$ coordinates and in the local rest frame can be parametrized as

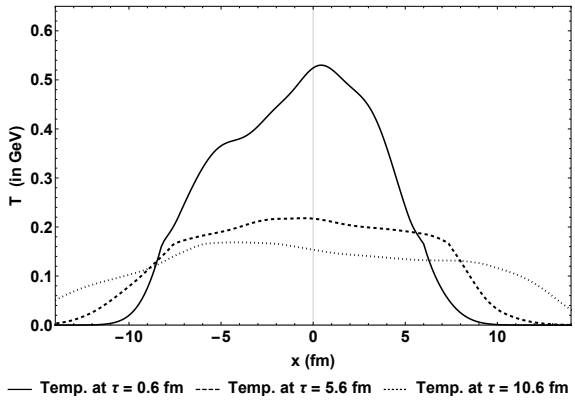

Figure 4.5: Temperature evolution at $y = 0$.

$$\pi^{\mu\nu} = \begin{bmatrix} 0 & 0 & 0 & 0 \\ 0 & \phi/2 & 0 & 0 \\ 0 & 0 & \phi/2 & 0 \\ 0 & 0 & 0 & -\phi/\tau^2 \end{bmatrix} \tag{4.13}$$

Our equation of motions involve only two independent variables (ϵ and ϕ) governed by the following equations (derived by imposing the symmetry of a 0+1 system in equations (2.15a) and (2.42))

$$\partial_\tau(\tau\epsilon) = -P + \phi \tag{4.14a}$$

$$\partial_\tau\phi = \frac{\phi_{NS} - \phi}{\tau_\pi} - \frac{4\phi}{3\tau}. \tag{4.14b}$$

Here there are no direct analytical solutions, but if we set τ_π to a small value (we test with $\tau_\pi = 0.005$ fm), then the ϕ relaxes to its Navier-Stokes value rather quickly. In such a scenario we can set $\phi = \phi_{NS} \equiv \frac{4\eta}{3\tau}$ in equation (4.14a). For our test we

have set $\eta/s = a = 0.2$. From (4.3), we can write $\epsilon = f\ T^4$, here $f = \frac{42.25\pi^2}{30}$. Now we are set to convert (4.14a) to an equation with temperature T as the independent variable.

$$\partial_\tau(\tau\ T^4) = -\frac{T^4}{3} + \frac{4}{3\tau}a\left(\frac{4T^3}{3}\right) \tag{4.15}$$

For a certain choice of initial temperature $T(\tau_0) = T_0$ at $\tau = \tau_0$, equation (4.15) has an analytical solution, given by

$$T(\tau) = \left(\frac{\tau_0}{\tau}\right)^{1/3} T_0 + \frac{2a}{3}\left(\frac{1}{\tau^{1/3}\ \tau_0^{2/3}} - \frac{1}{\tau}\right) \tag{4.16}$$

In figure 4.6 we show the results for evolution of temperature at $x = 0$, $y = 0$ and $\eta = 0$. In table 4.5 we can see the details of the grid we used. Despite the symmetry of $0 + 1$ we used the full $3 + 1$ dimensional viscous code with bulk viscosity turned off. As previously studied in [45] we start the hydro simulation from $\tau_0 = 0.6$ and we get a perfect agreement with the analytical solution.

Table 4.5: Grid details for the Bjorken test in the Navier Stokes limit.

Coordinate	Min	Max	Grid Spacing	Grid Points	Integration Scheme
x (in fm)	-0.5	0.4	0.1	9	KT(WENO)
y (in fm)	-0.5	0.4	0.1	9	KT(WENO)
η	-2	2	0.1	41	KT(WENO)
time τ (c)	0.6	10	0.01	940	TVDRK3

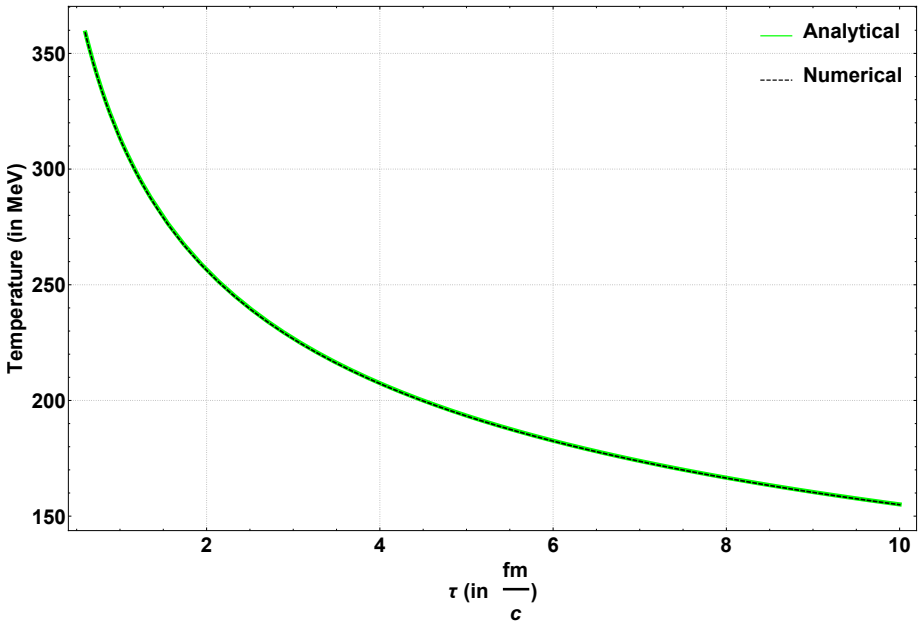

Figure 4.6: Temperature evolution at origin of the three dimensional hydro grid.

4.3.3 Bjorken Bulk Test

We repeat the same test as in previous sub-section 4.3.2 with bulk viscosity turned on. For the $0+1$ case the equation of motion for Π from (2.43) is

$$\partial_\tau(\Pi) = \frac{\Pi_{NS} - \Pi}{\tau_\Pi} - \frac{4\Pi}{3\tau} \tag{4.17}$$

Here we can use the Navier-Stokes value of bulk viscosity $\Pi_{NS} = -\zeta\ \partial_{;\mu} u^\mu$, which can be further simplified because the expansion $\partial_{;\mu} u^\mu = 1/\tau$ in the local rest frame of hyperbolic coordinates. One might be expecting expansion to be zero with $\vec{v} = 0$ in this frame, but this non-zero result we get is from the geometrical term of covariant derivative and hence is a result of the hyperbolic geometry. Of course in the usual cartesian coordinates we would have $v_z = \tanh(\eta)$. The details of the grid are the same as we used before in table 4.4. Now setting the initial condition $\Pi(\tau_0) = 0$ and

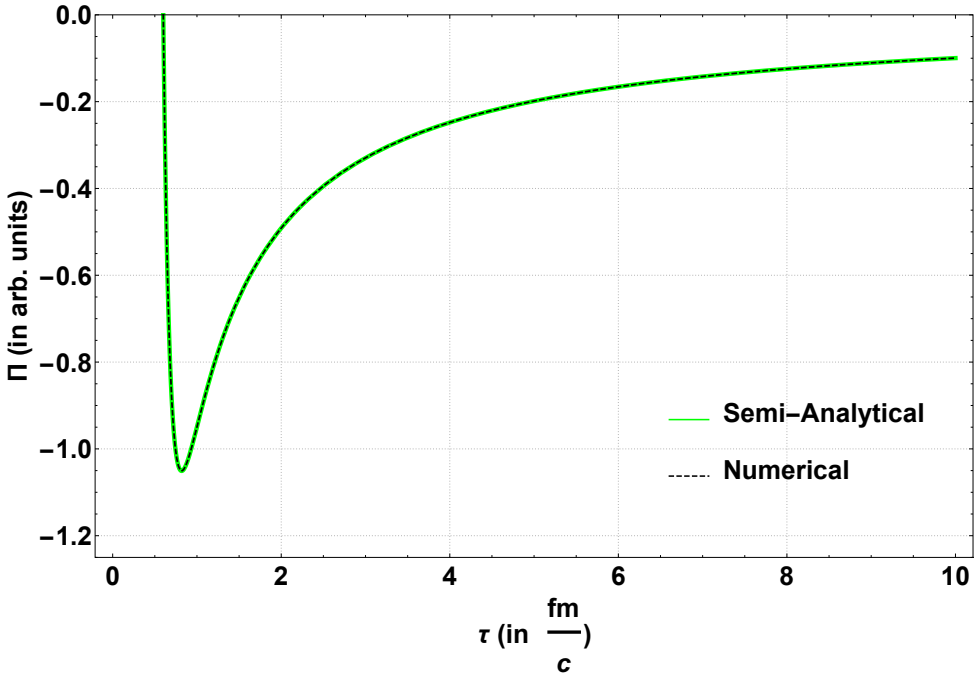

Figure 4.7: Bulk viscous stress evolution in the Navier-Stokes limit.

with the help of Mathematica [88] we can find the analytical result for Π

$$\Pi(\tau) = \frac{e^{-\frac{\tau}{\tau_\Pi}}\zeta\left(-\sqrt[3]{\tau}E_{\frac{2}{3}}\left(-\frac{\tau}{\tau_\Pi}\right) + \sqrt[3]{\tau_0}E_{\frac{2}{3}}\left(-\frac{\tau_0}{\tau_\Pi}\right) - 3\sqrt[3]{\tau}e^{\tau/\tau_\Pi} + 3\sqrt[3]{\tau_0}e^{\tau_0/\tau_\Pi}\right)}{3\tau^{4/3}} \tag{4.18}$$

Here $E_n(z) = \int_1^\infty \frac{\exp(-zt)}{t^n}\, dt$. In figure 4.7 we can see that our numerical result matches the analytical result perfectly. In this hydro run we used $\tau_0 = 0.6$ fm, $\tau_\Pi = 0.1$ fm and the bulk viscosity $\zeta = 1$.

4.3.4 3+1 Gubser Flow - Ideal

One of the most useful tests for relativistic hydrodynamics comes from Gubser flow [89, 90]. In [89], Gubser's primary objective was to find a generalization of Bjorken flow which could give a non-zero flow (u_r) in the transverse plane. The

intent was to break the translational invariance in the transverse plane while keeping the longitudinal boost invariance and the rotational invariance in the transverse plane. This symmetry possessed by the Gubser flow is $SO(3)_q \otimes SO(1,1) \otimes \mathbb{Z}_2$. The Minkowski metric in cylindrical like coordinates for the transverse plane can be parametrized as

$$ds^2 = d\tau^2 - dr^2 - r^2 d\phi^2 - \tau^2 d\eta^2. \tag{4.19}$$

Gubser discovered a flow that obeys the symmetry constraints (*i.e.* invariance under $\frac{\partial}{\partial\eta}$, $\frac{\partial}{\partial\phi}$ and $\eta \to -\eta$). In $\{\tau, r, \phi, \eta\}$ coordinates, this four velocity is parametrized as

$$u^\mu = \{\cosh(\kappa), \sinh(\kappa), 0, 0\} \tag{4.20}$$

and in $\{\tau, x, y, \eta\}$ coordinates as

$$u^\mu = \{\cosh(\kappa), \frac{x}{r}\sinh(\kappa), \frac{y}{r}\sinh(\kappa), 0\} \tag{4.21}$$

where ,

$$\kappa \equiv \text{arctanh}(\frac{2q^2\tau r}{1 + q^2\tau^2 + q^2 r^2}) \tag{4.22}$$

and q is a scaling factor. This expression for flow is used for both the inviscid and viscous tests. Since the flow is known at all times we do not have to solve analytically for equations (2.15b, 2.15c, 2.15d). It can be shown that for the inviscid case the energy density follows the analytical equation

$$\epsilon(\tau, r) = \frac{\hat{\epsilon_0}}{\tau^{4/3}} \quad \frac{(2q)^{8/3}}{[1 + 2q^2(\tau^2 + r^2) + q^4(\tau^2 - r^2)^2]^{4/3}} \tag{4.23}$$

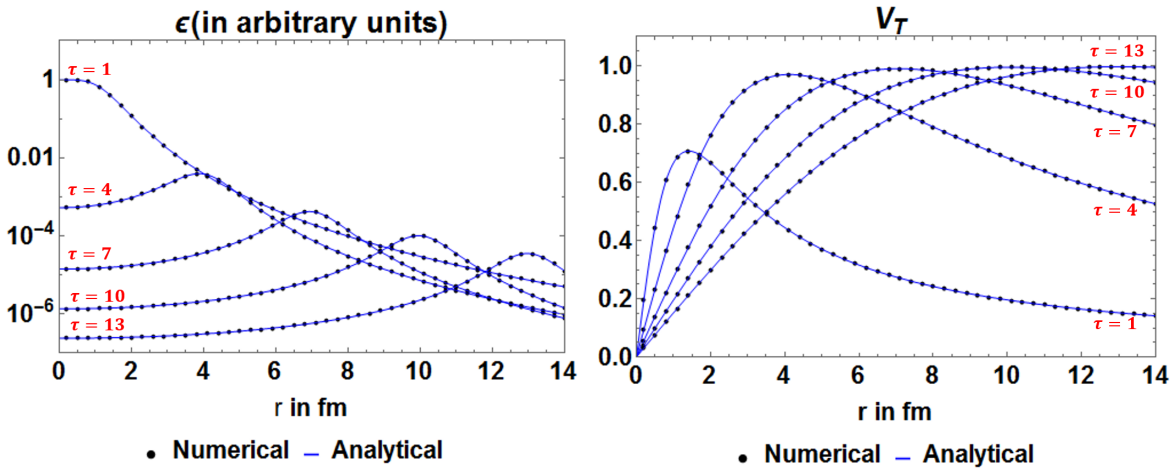

(a) ϵ plotted with respect to cylindrical coordinate r

(b) Transverse velocity V_T plotted with respect to cylindrical coordinate r

Figure 4.8: Gubser flow results - 3+1 ideal fluid.

Here, $\hat{\epsilon_0}$ is an integration constant. Notice that the transverse velocity $V_T = \sqrt{v_x^2 + v_y^2}$ is given by

$$V_T(\tau, r) = \tanh \kappa = \frac{2q^2\tau r}{1 + q^2\tau^2 + q^2 r^2} \tag{4.24}$$

For testing our $3 + 1$ ideal hydro code we set $q = \hat{\epsilon_0} = 1$. We start the hydro simulation from $\tau = 1$ and this gives us $\epsilon(1, 0) = 1$. With these assumptions we ran the hydro in a grid of specification shown in table 4.5. And we were able to get a stable and long run till $\tau = 13$ fm, in which the numerical results matched the analytical result perfectly.

Table 4.6: Grid details for ideal Gubser test.

Coordinate	Min	Max	Grid Spacing	Grid Points	Integration Scheme
x (in fm)	-16	15.9	0.1	320	KT(WENO)
y (in fm)	-16	15.9	0.1	320	KT(WENO)
η	-0.1	0.1	0.1	3	KT(WENO)
time τ (c)	1	13	0.01	1200	TVDRK3

4.3.5 Semi-Analytical Case with Israel-Stewart

Using the same Gubser flow as in the previous section and following along the lines of [91] we will test our code with solutions to Israel-Stewart equations. Ignoring bulk viscosity, vorticity and the flow equations (since flow is already defined) it can be shown that our equations of interest are

$$\frac{D(T)}{T} + \frac{1}{3}\partial_{;\rho}u^{\rho} + \frac{\pi_{\mu\nu}\,\sigma^{\mu\nu}}{sT} = 0 \tag{4.25a}$$

$$\frac{\tau_{\pi}}{sT}\left(\langle D\pi^{\mu\nu}\rangle + \frac{4}{3}\partial_{;\rho}u^{\rho}\right) + \frac{\pi^{\mu\nu}}{sT} = \frac{-2\eta\,\sigma^{\mu\nu}}{sT}. \tag{4.25b}$$

It would be easier to solve these equation if one could find a transformation wherein the Gubser flow transform to a zero flow in the new coordinates. This was done in [90] with the coordinate system

$$d\hat{s}^2 = d\rho^2 - \cosh^2\rho\, d\theta^2 - \cosh^2\rho\, \sin^2\theta\, d\phi^2 - d\eta^2 \tag{4.26}$$

Here ρ and θ are defined as

$$\rho = \operatorname{arcsinh}\left(\frac{1 - q^2\tau^2 + q^2r^2}{2q\tau}\right) \tag{4.27a}$$

$$\theta = \arctan\left(\frac{2qr}{1 + q^2\tau^2 - q^2r^2}\right) \tag{4.27b}$$

In the new coordinates and using $u^\mu = \{1, 0, 0, 0\}$, equation (4.25) can be written into two equations

$$\frac{1}{\hat{T}}\frac{d\hat{T}}{d\rho} + \frac{2}{3}\tanh\rho = \frac{1}{3}\hat{\pi}^\eta_\eta \tanh\rho \tag{4.28a}$$

$$\tau_\pi\left(\frac{d\hat{\pi}^\eta_\eta}{d\rho} + \frac{4}{3}(\hat{\pi}^\eta_\eta)^2\tanh\rho\right) + \hat{\pi}^\eta_\eta = \frac{4\tau_\pi}{3c}\tanh\rho. \tag{4.28b}$$

Here $\tau_\pi = \frac{c\,\eta}{\hat{T}\,s}$, η is the shear viscosity, s is the entropy and c is a constant. As we saw earlier in equations (4.10) and (4.13), in the rest frame the shear stress tensor has just one degree of freedom. The other non zero components can be found ($\hat{\pi}^\theta_\theta = \hat{\pi}^\phi_\phi = -\frac{\hat{\pi}^\eta_\eta}{2}$). These equations can be solved in Mathematica [88] and we can generate initial conditions by performing a coordinate transformation from $\hat{x} \equiv \{\rho, \theta, \phi, \eta\}$ to $x \equiv \{\tau, x, y, \eta\}$. The temperature T and $\pi^{\mu\nu}$ in hyperbolic coordinates are given by

$$T = \frac{\hat{T}}{\tau} \tag{4.29}$$

$$\pi^{\mu\nu} = \frac{1}{\tau^2}\,\frac{\partial x^\mu}{\partial \hat{x}^\alpha}\,\frac{\partial x^\nu}{\partial \hat{x}^\beta}\,\hat{\pi}^{\alpha\beta} \tag{4.30}$$

Thereafter the results from a hydro simulation can be compared to the solution found by Mathematica. This is the semi-analytical approach to testing the algorithm for the Israel Stewart equations. In our tests we took $q = 1$, $\tau_\pi = \frac{5\,\eta}{\hat{T}\,s}$ and the viscosity

by entropy ratio $\frac{\eta}{s}$ was set to 0.2. The details of the grid are given in table (4.7). We used 10 processors each in x and y direction for this test, in total using 100 processors.

Table 4.7: Grid details for viscous Gubser test.

Coordinate	Min	Max	Grid Spacing	Grid Points	Integration Scheme
x (in fm)	-23	22.075	0.025	1840	KT(WENO)
y (in fm)	-23	22.075	0.025	1840	KT(WENO)
η	-0.1	0.1	0.1	3	KT(WENO)
time τ (c)	1	6	0.001	5000	TVD-RK3

In figures 4.9 and 4.10 we can see the comparison plots between the hydro computation and the semi analytical results. We get very good agreement after 5000 TVD-RK3 integration steps.

4.3.6 Analytical with the Modified Israel-Stewart Equations

The slight drawback of the previous tests was the dependence on another library or method (Mathematica) to give us a numerical solution of (4.28a) and (4.28b), so that we can compare them with hydro. An analytical solution is more desirable, and as was argued in [91], that, in the so called *cold-plasma limit* with the assumption $\frac{\eta}{s\,\hat{T}} \gg 1$, we can set the term $\hat{\pi}^{\eta}_{\eta}$ to zero. This reduces (4.28b) to

$$\frac{d\hat{\pi}^{\eta}_{\eta}}{d\rho} + \frac{4}{3}(\hat{\pi}^{\eta}_{\eta})^2 \tanh\rho = \frac{4}{3\,c}\tanh\rho \tag{4.31}$$

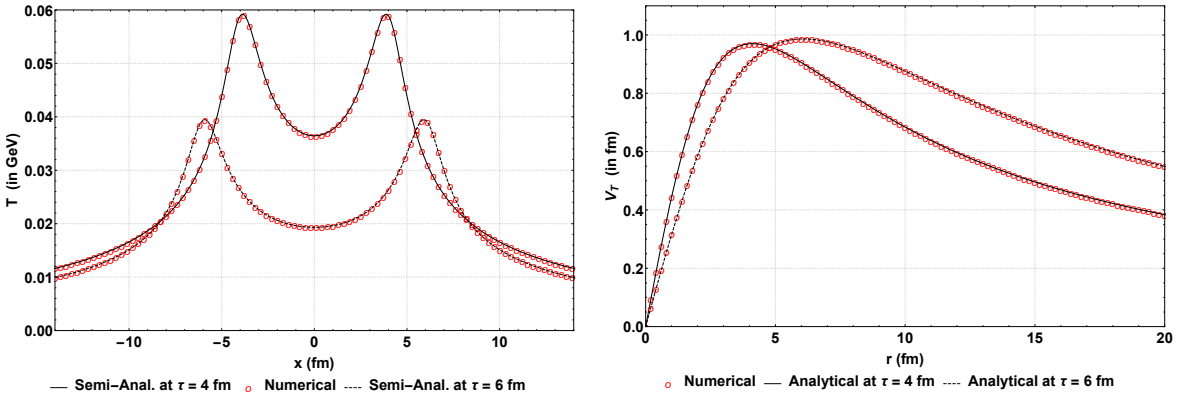

(a) Temperature T versus x at $y = 0$ and $\eta = 0$

(b) Transverse velocity V^T along $x = y$ at $\eta = 0$

Figure 4.9: Gubser flow results - comparison between hydro evolution and the semi-analytical calculations.

Now we set $c = 5$ as in the semi-analytical tests, and find that (4.31) has analytical solutions given by

$$\hat{\pi}^{\eta}_{\eta}(\rho) = \tanh\left[\frac{-5\alpha + (4/3)\log(\cosh\rho)}{\sqrt{5}}\right] \tag{4.32}$$

where α is some constant. We can use this solution of $\hat{\pi}^{\eta}_{\eta}(\rho)$ in (4.28a) and find the analytical solution for the temperature

$$\hat{T}(\rho) = \frac{\exp\big(5\alpha/2\big)\beta\cosh\left[\frac{-5\alpha+(4/3)\log(\cosh\rho)}{\sqrt{5}}\right]}{(\cosh\rho)^{2/3}} \tag{4.33}$$

where β is another constant.

For our hydro simulation we have set $\alpha = 0$ and $\beta = 1.21$. We can find the analytical functions for temperature T and $\pi^{\mu\nu}$ in $\{\tau, x, y, \eta\}$ coordinate system by using equations (4.29) and (4.30) respectively. These along with the Gubser flow profile (4.21) is used as the initial condition for the hydro simulation. The grid

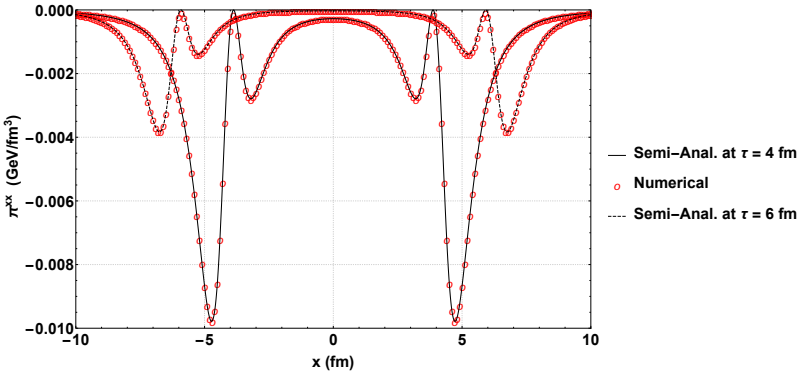

(a) π^{xx} versus x at $y = 0$ and $\eta = 0$

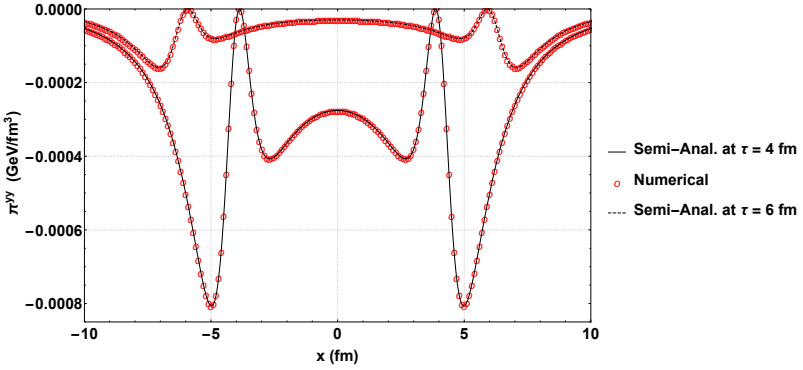

(b) π^{yy} versus x at $y = 0$ and $\eta = 0$

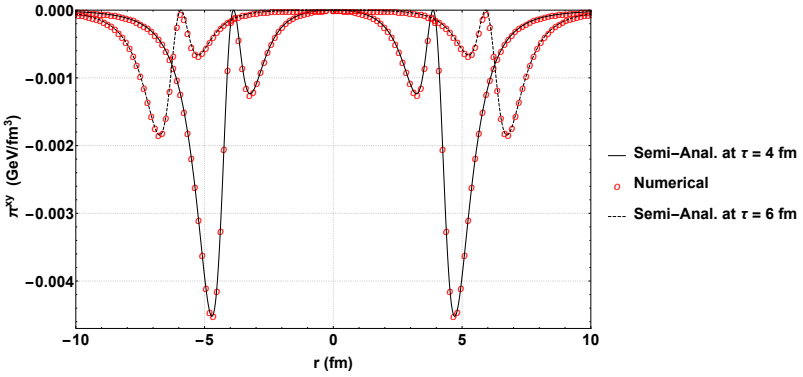

(c) π^{xy} along $x = y$ line and $\eta = 0$

Figure 4.10: Gubser flow results - comparison between hydro and the semi-analytical calculations.

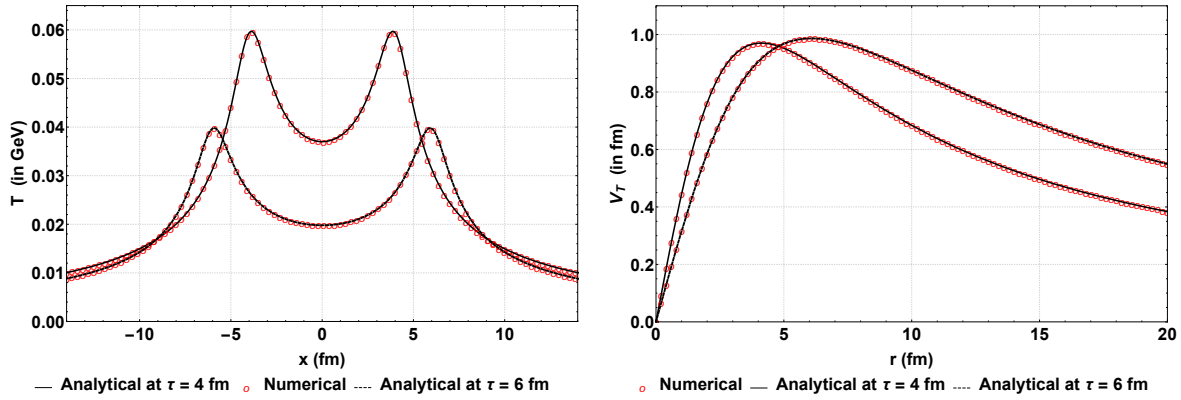

(a) Temperature T versus x at $y = 0$ and $\eta = 0$

(b) Transverse velocity V^T along $x = y$ at $\eta = 0$

Figure 4.11: Gubser flow results - comparison between hydro and the analytical calculations for the modified Israel-Stewart shear equations in the *cold-plasma limit*.

details are same as the table 4.7 in previous sub-section, and our results are in Fig. 4.11 and Fig. 4.12. For this test we also used 100 processors.

4.3.7 Non Boost Invariant Setup with Rapidity Cutoff in Energy Density

In this and the next test, we will employ profiles which are variant in η, in this way we are breaking the boost invariance. Here we will use an energy density profile which is invariant in x and y but has a profile in η made up of two half Gaussian's and a flat region around mid-rapidity.

$$\epsilon(x, y, \eta) = 16 \exp\left(- \left(\frac{|\eta| - \frac{\eta_F}{2}}{\sqrt{2}\sigma} \right)^2 \right) \theta\big(|\eta| - \frac{\eta_F}{2}\big) \text{ fm}^{-4} \tag{4.34}$$

$$v_x = v_y = v_\eta = 0; \tag{4.35}$$

Here, θ is the Heaviside function, η_F is the flat region in η centered around mid-rapidity and σ is the width of the Gaussian. This has been the standard procedure

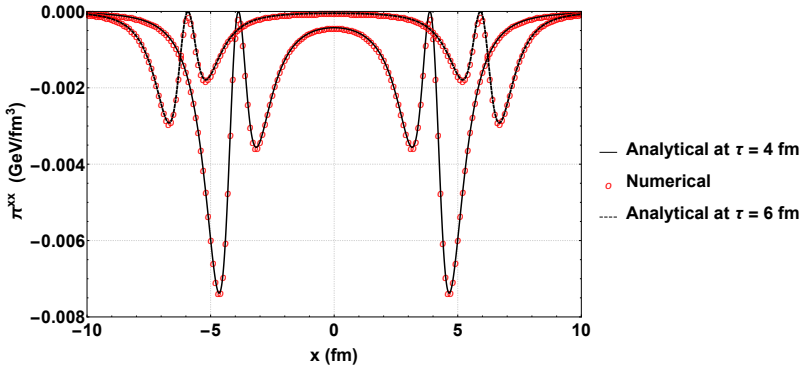

(a) π^{xx} versus x at $y = 0$ and $\eta = 0$

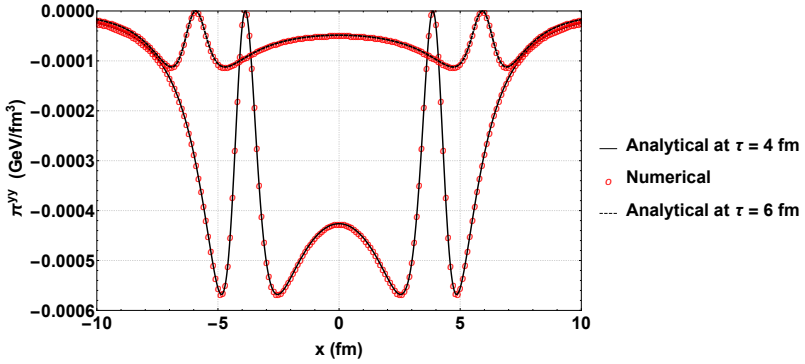

(b) π^{yy} versus x at $y = 0$ and $\eta = 0$

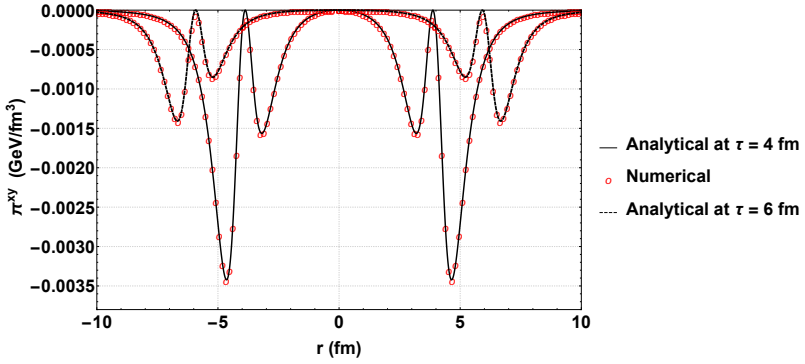

(c) π^{xy} along $x = y$ line and $\eta = 0$

Figure 4.12: Gubser flow results - comparison between hydro and the analytical calculations for the modified Israel-Stewart shear equations in the *cold-plasma limit*.

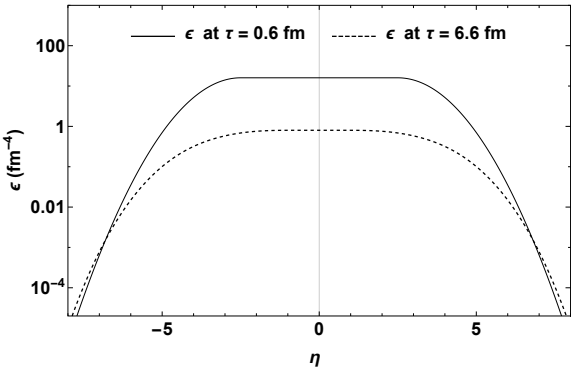

(a) Log plot of ϵ versus η at $x = 0$ and $y = 0$

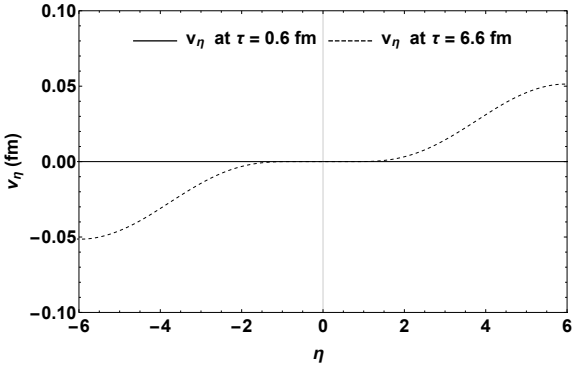

(b) v_η versus η at $x = 0$ and $y = 0$

Figure 4.13: Gaussian with a flat portion, initialization for ϵ.

to initialize $3 + 1$ D non-boost invariant hydrodynamics for many years [92, 93]. We expect the v_x and v_y to remain zero as there are no pressure gradients that drive transverse motion. However due to the pressure gradients in η we should see v_η developing flow outside the flat region of Gaussian's and indeed in Fig. 4.13b we see the expected behavior. The grid details for our simulation are given in table 4.8.

Table 4.8: Grid details for the Gaussian profile in η.

Coordinate	Min	Max	Grid Spacing	Grid Points	Integration Scheme
x (in fm)	-0.3	0.2	0.1	6	KT(WENO)
y (in fm)	-0.3	0.2	0.1	6	KT(WENO)
η	-8	8	0.025	641	KT(WENO)
time τ (c)	0.6	6.6	0.002	3000	TVD-RK3

4.3.8 Non Boost Invariant Setup Simulating $v_z = 0$

We know that boost invariance can be enforced in $\{t, x, y, z\}$ coordinates by using a velocity profile $v_z = \tanh(\eta)$. This boost invariance is much easily obtained in $\{\tau, x, y, \eta\}$ coordinates by setting $v_\eta = 0$. In appendix, in equation (A.30) we can see that corresponding to $v_z = 0$ we get

$$v_\eta = \frac{-\tanh(\eta)}{\tau} \tag{4.36}$$

This implies that if we initialize our hydro code with $v_x = 0$, $v_y = 0$ and $v_\eta = \frac{-\tanh(\eta)}{\tau}$ and a uniform spatially invariant energy density, then in the Minkowski world the fluid will be at rest. Hence by giving a non-trivial flow (4.36) in η direction we should observe that the energy density, pressure and temperature remain invariant with τ. Intuitively one can see that the in-built flow coming from the geometry of the hyperbolic coordinates is exactly canceled by the flow in (4.36), in such a manner that we end up with a static system.

Table 4.9: Grid details for $v_z = 0$ test.

Coordinate	Min	Max	Grid Spacing	Grid Points	Integration Scheme
x (in fm)	-0.3	0.2	0.1	6	KT(WENO)
y (in fm)	-0.3	0.2	0.1	6	KT(WENO)
η	-3	3	0.025	121	KT(WENO)
time τ (c)	0.6	5.6	0.002	2500	TVD-RK3

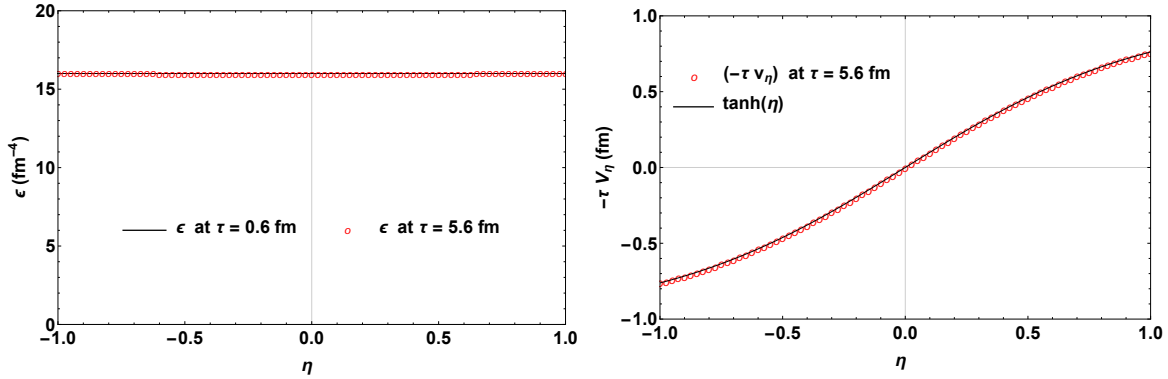

(a) ϵ versus η at $x = 0$ and $y = 0$

(b) $(-\tau v_\eta)$ versus η at $x = 0$ and $y = 0$

Figure 4.14: Non boost invariant evolution with $v_z = 0$.

To simulate this test we set a grid as in table 4.9. In the $3 + 1$ grid we initialize all grid points with $\epsilon = 16$ fm^{-4} at $\tau = 0.6$ fm. As expected, we observe in figure 4.14a that the temperature remains constant even after 2500 time steps at $\tau = 5.6$ as expected. Also notice that from equation (4.36) that the expression $-\tau v_\eta$ retains a static profile of $\tanh(\eta)$ with respect to η. In figure 4.14b we can see that the profile for $-\tau v_\eta$ and $\tanh(\eta)$ agree very well with each other at $\tau = 5.6$ fm.

In conclusion we can say that we have tested our code for numerical accuracy by giving it challenging initial conditions with non-trivial initial conditions in all the three directions.

5. COLOR GLASS CONDENSATE BASED INITIAL CONDITIONS

In this chapter we will give a brief overview of the Color Glass Condensate (CGC) theory following the work done by Guangyao Chen and Rainer Fries [94]. Then we work towards arriving at initial conditions for our hydrodynamics equations and thereafter we will discuss results from a subsequent hydro simulation. In section 5.2 we discuss matching of the Color Glass fields with the hydro energy momentum tensor. And in the last section 5.3 we will discuss some of the interesting results which came from evolution of this CGC based initial conditions with our 3+1 viscous hydro code.

5.1 Overview of CGC

In CGC theory the hadron is seen as a collection of valence quarks carrying large momentum fraction x and *wee* partons, which are small x carrying gluons. The system evolves at much longer time scale compared to typical collision times and hence the term color glass is used. Condensate refers to the saturated state of the gluons in the infinite momentum frame (IMF). Since the nuclei in heavy ion collisions at RHIC and LHC stay ultrarelativistic, using the IMF is a good assumption. Here it will be convenient to use the light cone coordinates

$$x^{\pm} = \frac{1}{\sqrt{2}}(t \pm z) \tag{5.1}$$

in describing the color currents associated with hadrons. One can also derive the relationship between the light cone coordinates and the proper time τ and the space

time rapidity η,

$$\tau = \sqrt{t^2 - z^2} = \sqrt{2x^+x^-} \tag{5.2a}$$

$$\eta = \frac{1}{2}\log\frac{t+z}{t-z} = \frac{1}{2}\log\frac{x^+}{x^-} \quad . \tag{5.2b}$$

The Yang-Mills equations describe the relation between gluon field strength $F^{\mu\nu}$ and the current J^ν

$$[D_\mu, F^{\mu\nu}] = J^\nu \tag{5.3}$$

where

$$D^\mu = \partial^\mu - igA^\mu, \tag{5.4}$$

is the covariant derivative and the field strength tensor is given by

$$F^{\mu\nu} = \frac{i}{g}[D^\mu, D^\nu] \quad . \tag{5.5}$$

The components of the current J^ν are given by

$$J_1^+(x) = \delta(x^-)\rho_1(\vec{x}_\perp), \quad J_1^-(x) = 0 \tag{5.6a}$$

$$J_2^-(x) = \delta(x^+)\rho_2(\vec{x}_\perp), \quad J_2^+(x) = 0 \tag{5.6b}$$

$$J_{1,2}^i = 0 \tag{5.6c}$$

reflecting the two colliding nuclei approaching each other along the light cone axes. ρ_1 and ρ_2 are the distributions of color charges in nucleus 1 and 2 in the transverse

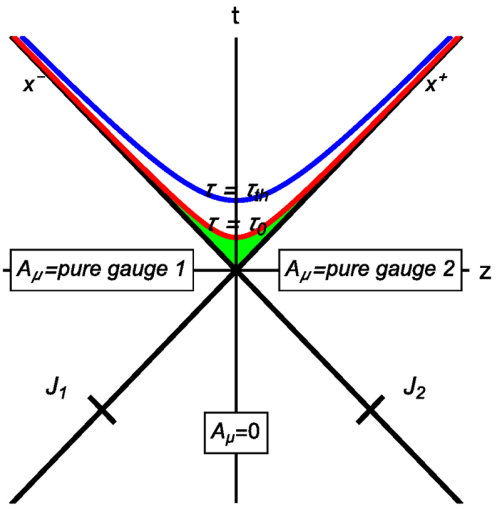

Figure 5.1: Light cone coordinates and the initial field configuration. The green region is the applicability for the CGC theory wherein we want to use the τ expansion. Image taken with permission from [6].

plane. And for the choice of axial gauge

$$x^+ A^- + x^- A^+ = 0, \tag{5.7}$$

the current J^ν fulfills the equation of continuity

$$[D_\mu, J^\mu] = 0 \tag{5.8}$$

We can express the charge currents and fields in terms of light cone coordinates x^+, x^- and the transverse coordinates $x_\perp$. In light of longitudinal boost invariance we can see that the glasma fields of the individual nuclei and the collided nuclei depend only on the transverse coordinates. In case of collided nuclei there is also an additional τ dependence for the evolving fields. The following ansatz solution for

the fields reflects these properties

$$A^+(x) = \Theta(x^+)\Theta(x^+)x^+A(\tau, \vec{x}_\perp) \tag{5.9}$$

$$A^-(x) = -\Theta(x^+)\Theta(x^-)x^-A(\tau, \vec{x}_\perp) \tag{5.10}$$

$$\begin{aligned} A^i(x) = {} & \Theta(x^-)\Theta(-x^+)A_1^i(\vec{x}_\perp) \; + \; \Theta(x^-)\Theta(-x^+)A_1^i(\vec{x}_\perp) \\ & + \Theta(x^+)\Theta(x^-)A_\perp^i(\tau, \vec{x}_\perp) \end{aligned} \tag{5.11}$$

Here, $A_1^i(\vec{x}_\perp)$ and $A_2^i(\vec{x}_\perp)$ are the gluon fields of individual nuclei before the collision whereas $A_\perp^i(\tau, \vec{x}_\perp)$ and $A(\tau, \vec{x}_\perp)$ are the fields after collision. In figure 5.1 we can see the two currents J_1 and J_2 traveling along the light cone axes's. The boundary conditions connecting different sections for the forward light cone are

$$A_\perp^i(\tau = 0, \vec{x}_\perp) = A_1^i(\vec{x}_\perp) + A_2^i(\vec{x}_\perp) \tag{5.12}$$

$$A(\tau = 0, \vec{x}_\perp) = -\frac{ig}{2}[A_1^i(\vec{x}_\perp), A_2^i(\vec{x}_\perp)] \tag{5.13}$$

5.1.1 CGC for Later Times - τ Expansion

In [51, 52] a novel approach to solve the Yang Mills equations was proposed. The crux of the idea was to focus on the *near field* at small τ as at higher τ's, as the classical Yang Mills loses its applicability. The solution proposed [95] was to use a power series expansion

$$A(\tau, \vec{x}_\perp) = \sum_{n=0}^{\infty} \tau^n A_{(n)}(\vec{x}_\perp) \tag{5.14}$$

$$A_\perp^i(\tau, \vec{x}_\perp) = \sum_{n=0}^{\infty} \tau^n A_{\perp(n)}^i(\vec{x}_\perp) \tag{5.15}$$

For the general solution of the non-abelian case, a recursion solution was found

by Fries et al in [52]. The solution for even n, $n > 1$ was found to be

$$A_{(n)} = \frac{1}{n(n+2)} \sum_{k+l+m=n-2} \left[D^i_{(k)}, \left[D^i_{(l)}, A_{(m)}\right]\right], \tag{5.16}$$

$$A^i_{\perp(n)} = \frac{1}{n^2}\Bigg(\sum_{k+l=n-2} \left[D^j_{(l)}, F^{ji}_{(l)}\right] + ig \sum_{k+l+m=n-4} \left[A_{(k)}, \left[D^i_{(l)}, A_{(m)}\right]\right]\Bigg). \tag{5.17}$$

The boundary condition (5.12, 5.13) is the initial step for the recursion in which one finds that odd power contributions vanish and the even terms ($n > 1$) remain. From this approach one can compute the chromoelectric and chromomagnetic field at different orders of τ terms.

$$\mathbf{E} = \mathbf{E}_{(0)} + \tau\mathbf{E}_{(1)} + \tau^2\mathbf{E}_{(2)} + ... \tag{5.18}$$

$$\mathbf{B} = \mathbf{B}_{(0)} + \tau\mathbf{B}_{(1)} + \tau^2\mathbf{B}_{(2)} + ... \tag{5.19}$$

by using

$$F^{+-} = -\frac{1}{\tau}\frac{\partial}{\partial\tau}\tau^2 A, \tag{5.20}$$

$$F^{i\pm} = -x^{\pm}\left(\frac{1}{\tau}\frac{\partial}{\partial\tau}A^i_{\perp} \mp [D^i, A]\right), \tag{5.21}$$

$$F^{ij} = \partial^i A^j_{\perp} - \partial^j A^i_{\perp} - ig[A^i_{\perp}, A^j_{\perp}], \tag{5.22}$$

one observes that only the longitudinal components of electric and magnetic field are

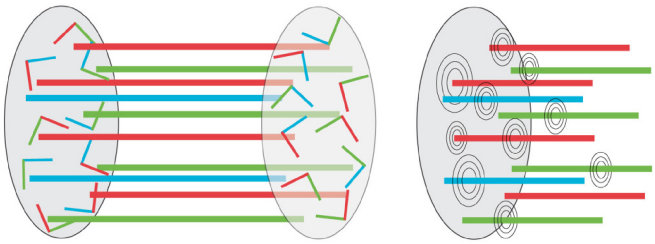

Figure 5.2: On the left we see in the immediate aftermath of the collision only the longitudinal chromofields exist. On the right we see that shortly thereafter at later τ the transverse chromofields are developing fueled by the QCD version of Gauss's law and Ampere's law. Image taken with permission from [6].

non-zero at $\tau = 0$

$$E_0 \equiv E^3_{(0)} = F^{+-}_{(0)} = ig[A^i_1, A^i_2] \tag{5.23}$$

$$B_0 \equiv B^3_{(0)} = F^{21}_{(0)} = ig\,\epsilon^{ij}[A^i_1, A^i_2]. \tag{5.24}$$

It is observed that longitudinal fields have even powers of τ contributions and the transverse fields have odd power of τ contributions. For expressions of higher order terms $(E^i_1, B^i_1, E^3_2, B^3_2)$ please refer to [6].

An intuitive understanding is that at $\tau = 0$ only longitudinal chromofields exist, but at later times due to the change of the longitudinal chromofields, transverse chromofields are generated. This is analogous to what we see in classical electrodynamics and depicted in figure 5.2.

5.1.2 Energy Momentum Tensor for the Initial Gluon Field

We can compute the energy momentum tensor of the gluon field just like in the case of electromagnetic fields

$$T^{\mu\nu} = F^{\mu\lambda}F^{\nu}_{\lambda} + \frac{1}{4}g^{\mu\nu}F^{\kappa\lambda}F_{\kappa\lambda} \quad . \tag{5.25}$$

Like our previous approach we can analyse the tensor $T^{\mu\nu}$ by expansion in τ

$$T^{\mu\nu} = T^{\mu\nu}_{(0)} + \tau T^{\mu\nu}_{(1)} + \tau^2 T^{\mu\nu}_{(2)} + ... \tag{5.26}$$

At $\tau = 0$ the energy momentum tensor is diagonal $T^{\mu\nu}_{(0)} = diag\{\epsilon_0, \epsilon_0, \epsilon_0, -\epsilon_0\}$, similar to a longitudinal field in classical electrodynamics. Here,

$$\epsilon_0 = \frac{1}{2}(E_0^2 + B_0^2) \ . \tag{5.27}$$

At first order we have contributions with η dependence (despite being longitudinally boost invariant) and contributions which reflect the onset of the transverse flow

$$T^{0i}_{(1)} = \frac{1}{2}\alpha^i \cosh\eta + \frac{1}{2}\beta^i \sinh\eta \tag{5.28}$$

$$T^{3i}_{(1)} = \frac{1}{2}\alpha^i \sinh\eta + \frac{1}{2}\beta^i \cosh\eta \tag{5.29}$$

and here

$$\alpha^i = -\boldsymbol{\nabla}^i \epsilon_0 \tag{5.30}$$

$$\beta^i = \epsilon^{ij}\big([D^j, B_0]E_0 - [D^j, E_0]B_0\big) \tag{5.31}$$

For second and higher order terms please refer to [6].

5.1.3 Average Energy Momentum Tensor for Colliding Nuclei

What we saw in previous section was the description of the energy momentum tensor in terms of initial charges ρ_1 and ρ_2 . They are not known to us however if we know the statistical distributions of the color charge densities ρ_k then we can analytically compute the two point correlation functions for the gluon fields $\langle A(\vec{x}_\perp)A(\vec{y}_\perp)\rangle$, where $\langle..\rangle$ denotes a statistical average over all ρ_k. Using a Gaussian distribution

for color charges, as proposed first by McLerran and Venugopalan [96, 97], one can analytically calculate gluon correlation functions. After this one can go ahead and calculate the energy momentum tensor for the collided nuclei. All these extensive calculations have been carried out in detail in [6]. We will quote the result for the energy momentum tensor in $\{\tau, x, y, \eta\}$ coordinates up to the second order terms. For a Gaussian distribution we only need to know the expectation values $\langle \rho_k \rangle = 0$ for both nuclei $\langle \rho_k(\vec{x}), \rho_k(\vec{y}) \rangle = \frac{g^2}{N_c^2 - 1}\ \mu_k\ \delta^{(2)}(\vec{x} - \vec{y})$

$$T^{\mu\nu}(\tau, x_\perp) = \begin{bmatrix} \epsilon_0 - \frac{\tau^2}{8}(-2\Delta\epsilon_0\ +\ \delta) & \frac{\tau}{2}\alpha^x & \frac{\tau}{2}\alpha^y & \frac{\tau}{8}\boldsymbol{\nabla}^i\beta^i \\ \frac{\tau}{2}\alpha^x & \epsilon_0 - \frac{\tau^2}{4}(-\Delta\epsilon_0\ +\ \delta) & 0 & \frac{1}{2}\beta^x \\ \frac{\tau}{2}\alpha^y & 0 & \epsilon_0 - \frac{\tau^2}{4}(-\Delta\epsilon_0\ +\ \delta) & \frac{1}{2}\beta^y \\ \frac{\tau}{8}\boldsymbol{\nabla}^i\beta^i & \frac{1}{2}\beta^x & \frac{1}{2}\beta^y & \frac{\epsilon_0}{\tau^2} + \frac{1}{8}(-2\Delta\epsilon_0\ +3\ \delta) \end{bmatrix} \tag{5.32}$$

Let's unpack the expression for the stress tensor. The term ϵ_0 is given by

$$\epsilon_0(\vec{x}_\perp) = \frac{2\pi N_c \alpha_s^3}{N_c^2 - 1}\mu_1(\vec{x}_\perp)\mu_2(\vec{x}_\perp) \ln\left(\frac{Q_1^2}{\hat{m}^2}\right) \ln\left(\frac{Q_2^2}{\hat{m}^2}\right), \tag{5.33}$$

where N_c is the number of color charges, α_s is the coupling constant for the strong force and Q_1, Q_2 are energy scales for each nucleus. The α^i and β^i are given by

$$\alpha^i = -\epsilon_0 \frac{\boldsymbol{\nabla}^i(\mu_1\mu_2)}{\mu_1\mu_2}, \tag{5.34}$$

$$\beta^i = -\epsilon_0 \frac{\mu_2\boldsymbol{\nabla}^i\mu_1 - \mu_1\boldsymbol{\nabla}^i\mu_2}{\mu_1\mu_2}\ . \tag{5.35}$$

The δ term is

$$\delta = 4\epsilon_0 Q^2 \ln^{-1}\left(\frac{Q^2}{\hat{m}^2}\right) \tag{5.36}$$

Finally, the $\Delta\epsilon_0$ term is the divergence for ϵ_0 given by $(\partial_x^2 + \partial_y^2)\epsilon_0$. The equations in this subsection provide a description of the true evolution of the energy momentum tensor of the system up to a roughly a time $\approx$ 1/saturation scale $\approx$ 0.1 to 0.2 fm/c at RHIC and LHC.

5.2 Matching with Hydro - Initial Conditions

For generating the CGC initial conditions for our hydro code it is essential that we first compute the energy momentum tensor in equation (5.30). It is interesting to note that the tensor only depends on the transverse coordinates and the proper time τ, we can see it is manifestly boost invariant. The key step in computing the tensor in code is to first get the average charge densities of both nuclei μ_1 and μ_2. From (5.31) we can see that ϵ_0 is proportional to the product '$\mu_1(\vec{x}_\perp)\mu_2(\vec{x}_\perp)$'. We use the thickness function from equation (1.4) derived from the Wood Saxon potential for the functional form of the μ_k. For this in our code we numerically integrate the Wood-Saxon nucleon density over z-axis using the GSL library and compute the thickness function as a function of transverse coordinates only. In our hydro simulation we used the thickness function of two Gold (Au) nuclei separated by an impact parameter b, hence the nuclear densities are

$$\begin{aligned} \mu_1 &= C\, T_{Au}\left(x + \frac{b}{2}, y\right), \\ \mu_2 &= C\, T_{Au}\left(x - \frac{b}{2}, y\right). \end{aligned} \tag{5.37}$$

where C is a normalization parameter. Once we compute μ_1 and μ_2 for both

the nuclei then it is straightforward to compute the ϵ_0, δ_1, α^i and β^i terms from equations (5.32) and (5.33). In this step we also need the x and y derivatives of the μ's, for which we used the WENO scheme, so as to get smooth numerical gradients. Lastly for the hydro simulation we chose an energy scale of $Q = 1$ GeV and mass $\hat{m} = 0.3$ GeV. With this our calculation of the tensor in (5.30) is complete.

At this point our energy momentum tensor describes a system of classical gluon fields. The actual process of decoherence and thermalization is not quite clear yet, but is known to happen very fast. Here we adopt the matching procedure as in [98]. Thus we simply decompose the energy momentum tensor into the local energy density ϵ, the four velocity u^μ, shear viscosity $\pi^{\mu\nu}$ and the bulk viscosity Π. Thus we simply write (5.30) as

$$T^{\mu\nu} = \big(\epsilon + P(\epsilon)\big)u^\mu u^\nu - P(\epsilon)\, g^{\mu\nu} + \pi^{\mu\nu} + \Delta^{\mu\nu}\, \Pi \tag{5.38}$$

Notice that,

$$T^{\mu\nu}u_\nu = \big(\epsilon + P(\epsilon)\big)u^\mu - P(\epsilon)\, u^\mu = \epsilon\, u^\mu. \tag{5.39}$$

Using this interesting property we can see that the solution for the Eigenvalue problem

$$T^\mu{}_\nu\, u^\nu = \epsilon\, u^\mu, \tag{5.40}$$

gives us the local energy density ϵ as the Eigenvalue and the four velocity comes from the corresponding Eigenvector. We use the *GSL* library routines to solve for the Eigen values of $T^\mu{}_\nu$. Out of the possible four solutions, only one set of Eigenvalue and vector, gives us positive ϵ and a causal structure for the four velocity. Next thing

in order, is to find both the bulk and shear viscosity. Another property of the energy momentum tensor is that its trace is given by

$$\mathrm{Tr}(T^{\mu\nu}) = \epsilon - 3P(\epsilon) + 3\Pi. \tag{5.41}$$

Since we already know the tensor $T^{\mu\nu}$, ϵ and $P(\epsilon)$, we can calculate the bulk viscosity

$$\Pi = \frac{1}{3}\bigg(\mathrm{Tr}(T^{\mu\nu}) - \epsilon + 3P(\epsilon) \bigg). \tag{5.42}$$

Finally we can calculate the shear tensor,

$$\pi^{\mu\nu} = T^{\mu\nu} - \bigg[\big(\epsilon + P(\epsilon)\big) u^{\mu}u^{\nu} - P(\epsilon)\ g^{\mu\nu} + \Delta^{\mu\nu}\ \Pi \bigg]\ . \tag{5.43}$$

Here we have used the modern lattice QCD equation of state *s95p-PCE165-v0* [1, 99], in its parametrized form.

From this we now have a complete CGC based initial condition which gives us fluid energy, velocity and the initial viscosity. Recall that the Navier-Stoke values of viscosities are given by

$$\pi^{\mu\nu}_{NS} = 2\ \eta\ \Delta^{\mu\nu\alpha\beta}\ \partial_{;\alpha}u_{\beta} \tag{5.44}$$

$$\Pi_{NS} = -\zeta\ \ \partial_{;\rho}u^{\rho} \tag{5.45}$$

In figure (5.3) we present comparisons between the bulk and shear stress from CGC initial conditions and the bulk and shear stress from Navier-Stokes based on the initial flow profile. We find two interesting features

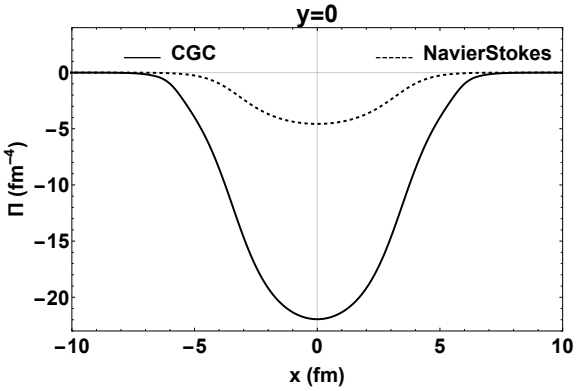

(a) Bulk viscosity Π versus x at $y = 0$

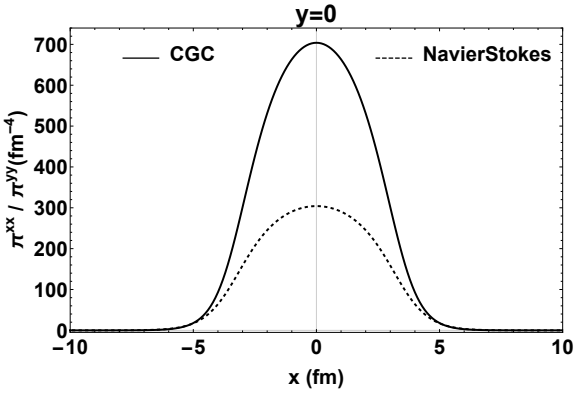

(b) Shear viscosity π^{xx} or π^{yy} versus x at $y = 0$

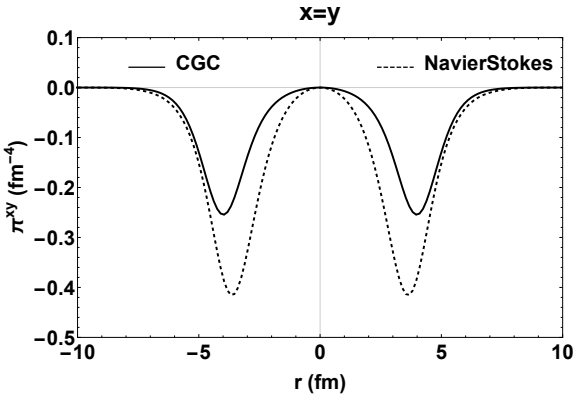

(c) Shear viscosity π^{xy} versus r along $x = y$

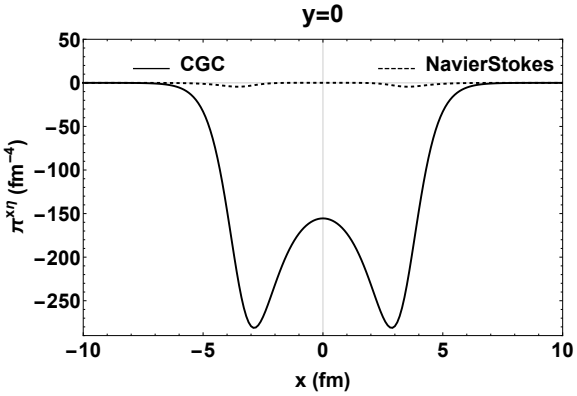

(d) Shear viscosity $\pi^{x\eta}$ versus x at $y = 0$

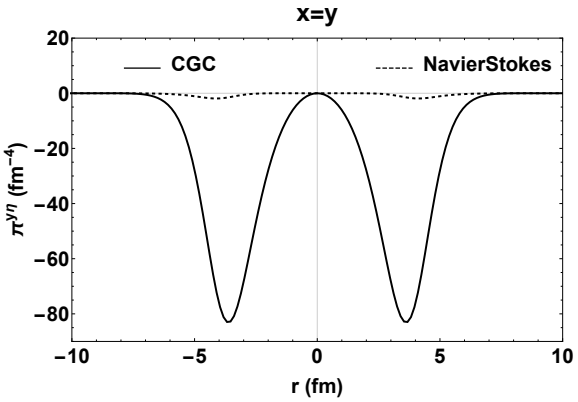

(e) Shear viscosity $\pi^{y\eta}$ versus r at $x = y$

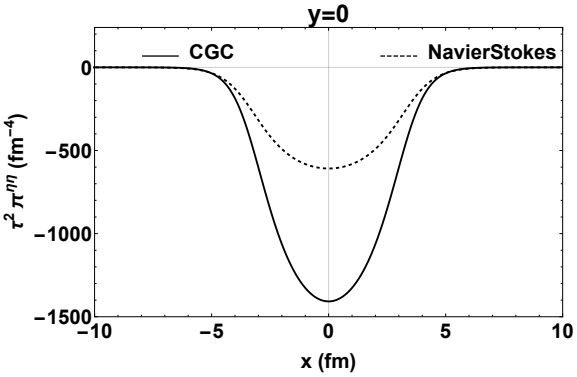

(f) Shear viscosity $\tau^2\pi^{\eta\eta}$ versus x at $y = 0$

Figure 5.3: Comparative plots between CGC based initial condition and the Navier-Stokes initialization for both shear and bulk viscosities at $\tau = 0.1$ fm.

- The general shape of viscous stress (both bulk and shear) from classical gluon fields is similar to their Navier-Stokes behavior.

- We can see that except for π^{xy} in all other cases the magnitude of viscous stress from CGC is greater than the Navier Stokes value, and in some cases like $\pi^{x\eta}$ or $\pi^{y\eta}$ the difference can be very large.

While the latter result is not surprising as the system is not close to equilibrium, the first result is somewhat unexpected and deserves more attention in the future.

5.3 Results

In this section we will present some of the results from our CGC hydro simulation. For this section we have simulated the collision of two gold nuclei at various impact parameters. The parameter C in (5.37) and hence the initial maximum temperature in the grid at $\tau = 0.1$ fm has been adjusted such that

$$T_{max}(\tau = 0.6 \text{ fm}) \approx 0.4 \text{ GeV}, \tag{5.46}$$

which roughly matches initial energy densities at RHIC. However no precision fits to data have been performed here for further refinement.

5.3.1 Evolution of Physical Quantities

For observing the evolution of physical quantities we did a simulation with impact parameter of $b = 6$ fm. In table 5.1 we have listed the details of the grid. The shear viscosity over entropy ratio was set at $\eta/s = 1/4\pi$. Bulk viscosity was set at $\zeta/s = 0.01/4\pi$.

Table 5.1: Grid details for the CGC initial condition at $b = 6$ fm.

Coordinate	Min	Max	Grid Spacing	Grid Points	Integration Scheme
x (in fm)	-20	19.5	0.1	400	KT(WENO)
y (in fm)	-20	19.5	0.1	400	KT(WENO)
η	-0	0	0	1	KT(WENO)
time τ (c)	0.1	9.604	0.002	4752	TVD-RK3

In Fig. 5.4 we show temperature T, velocities v_x, v_η and the shear stress π^{xy} at various time steps between 0.1 fm and 9.6 fm for $\eta = 0$. As expected we can see the temperature coming down until we stop the hydro simulation when the system cools down below 120 MeV.

5.3.1.1 Flow Features

The angular momentum about y axis, L_y is a quantity of interest for us. We talk about it in more detail in the sub-section 5.3.3. Since the flow v_y does not contribute to L_y let's study the flow vector $\{v_x, v_\eta\}$ in the xη plane. We can see in Fig. 5.5a that the initial longitudinal velocities v_η dominates and contributes to a negative L_y and by the end of the hydro simulation (Fig. 5.5b) we see that the v_η dies and we have a strong radial flow.

5.3.2 Momentum Anisotropy

In this and the next sub-section (5.3.3) we run the CGC simulation at various impact parameters. The x and y grid details are same as in table 5.1. In each case, as before, we run the hydro simulation until the peak temperature in the computational

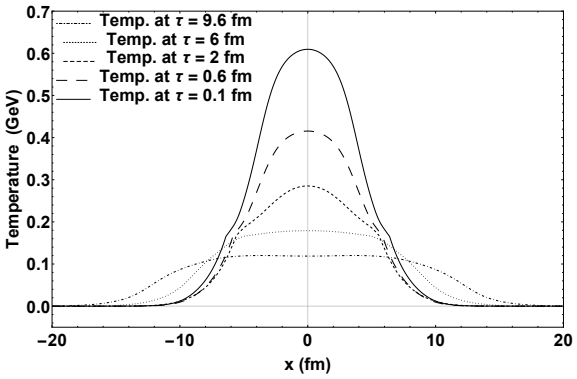

(a) Temperature evolution at $y = 0$ *w.r.t* x

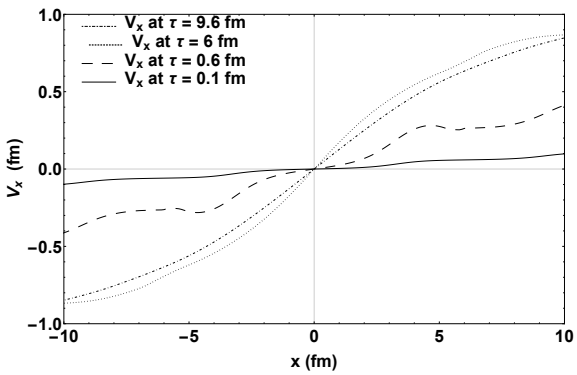

(b) x-component of velocity V_x at $y = 0$

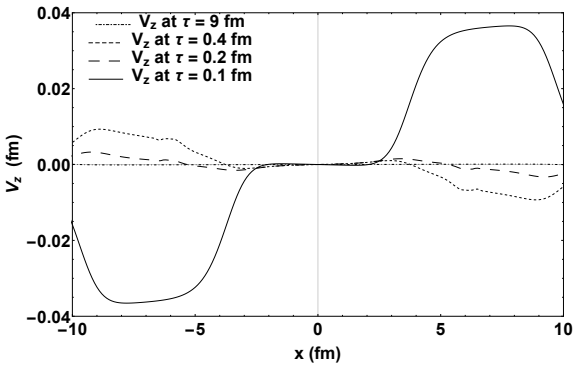

(c) z-component of velocity V_x at $y = 0$

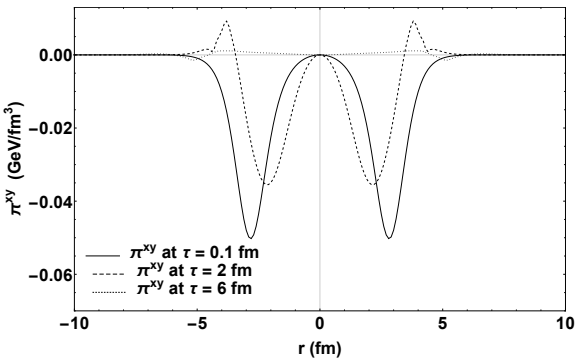

(d) π^{xy} is plotted along the line $x = y$

Figure 5.4: Time evolution of temperature T, velocities v_x and $v_z \equiv \tau v_\eta$ and the shear stress component π^{xy} of the physical quantities. All of these quantities have been calculated at $\eta = 0$ for the longitudinal boost invariance assumption and with an impact parameter of $b = 6$ fm.

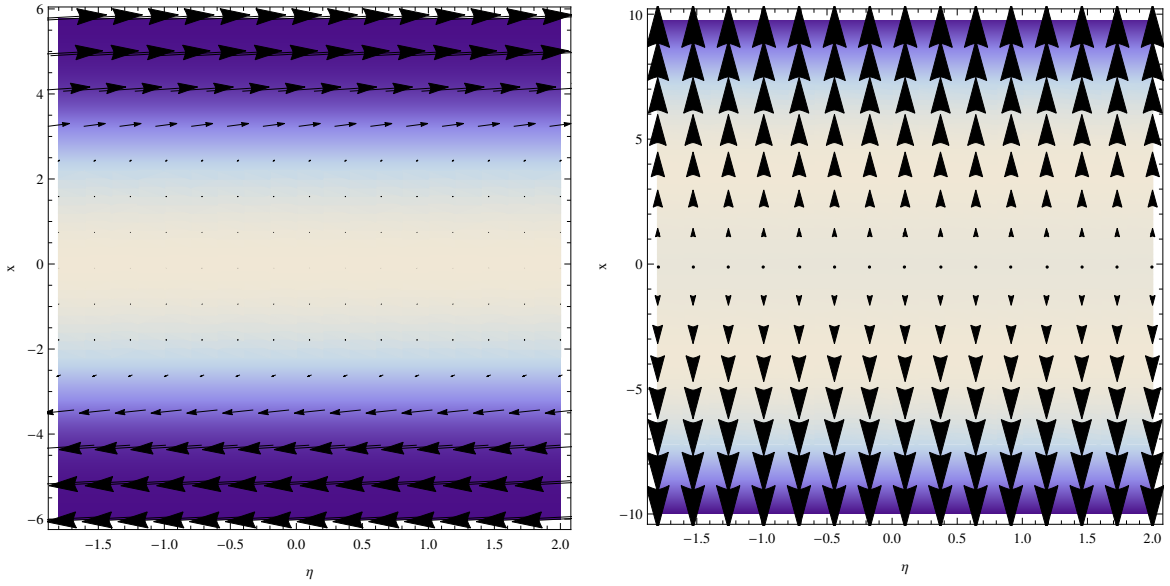

(a) $\{v_x, v_\eta\}$ vector plotted at $\tau = 0.1$ fm

(b) $\{v_x, v_\eta\}$ vector plotted at $\tau = 9.6$ fm

Figure 5.5: A plot of the vector $\{v_x, v_\eta\}$ at $y = 0$ in the xη plane. The colored shading in background shows the energy density. The initial longitudinal flow converts to radial flow by the end of hydro simulation.

grid has cooled down below 120 MeV. Hence, dependent on the impact parameter b, the run time of the simulation is different for each case. We show the temporal grid details in table 5.2. In hydrodynamics the anisotropy

$$\omega = \frac{\int \left(T^{xx} - T^{yy}\right) dx\ dy}{\int \left(T^{xx} + T^{yy}\right) dx\ dy}, \tag{5.47}$$

is the quantity reflecting elliptic flow v_2. We can also define this only for the ideal part of energy momentum tensor.

$$\omega_{ideal} = \frac{\int \left(T^{xx}_{ideal} - T^{yy}_{ideal}\right) dx\ dy}{\int \left(T^{xx}_{ideal} + T^{yy}_{ideal}\right) dx\ dy} \tag{5.48}$$

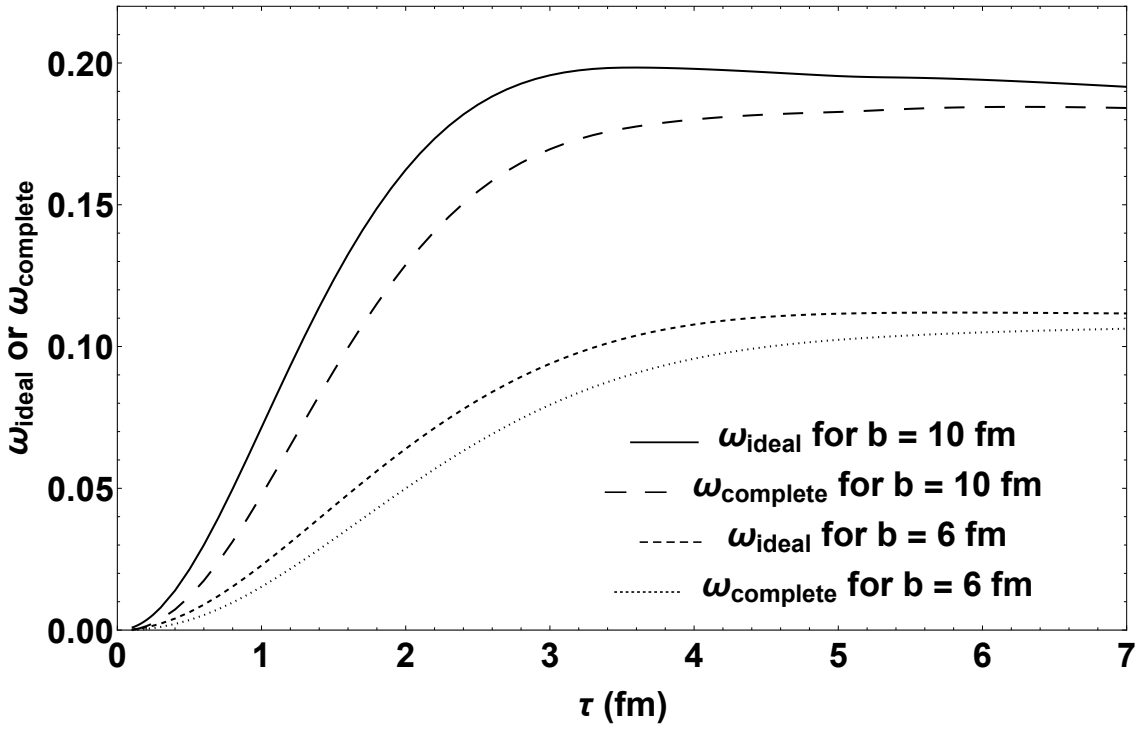

Figure 5.6: Momentum anisotropy.

In Fig. 5.6 one can observe the expected suppression in anisotropy to the ideal part due to the presence of shear and bulk viscosity.

Table 5.2: Grid details for the time evolution of CGC runs at various impact parameters

Coordinate	Min	Max	Grid Spacing	Grid Points	Integration
$b = 0$, time τ (in fm)	0.1	12.224	0.002	6062	TVD-RK3
$b = 2$, time τ (in fm)	0.1	11.806	0.002	5853	TVD-RK3
$b = 4$, time τ (in fm)	0.1	10.804	0.002	5352	TVD-RK3
$b = 6$, time τ (in fm)	0.1	9.604	0.002	4752	TVD-RK3
$b = 8$, time τ (in fm)	0.1	8.558	0.002	4229	TVD-RK3
$b = 10$, time τ (in fm)	0.1	7.602	0.002	3751	TVD-RK3

5.3.3 Angular Momentum - L_y

Our CGC initial conditions exhibit obvious angular momentum for $b \neq 0$. This is to be expected. Note however that the total angular momentum in the system would not be conserved since the sources on the light cone are fixed. However, we can study angular momentum around mid-rapidity and relative behavior *e.g.* as a function of impact parameter. In the relativistic case we need the covariant angular momentum density tensor

$$\mathcal{M}^{\mu\nu\rho} = x^{\mu}T^{\nu\rho} - x^{\nu}T^{\mu\rho} \tag{5.49}$$

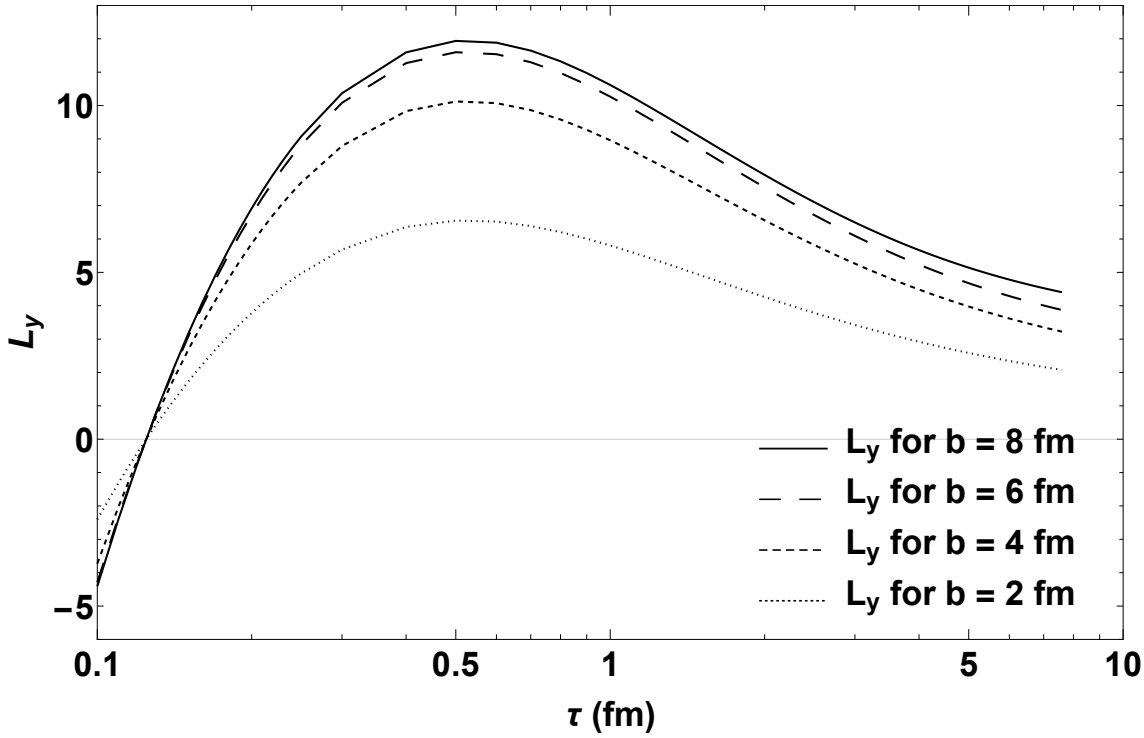

Figure 5.7: Angular momentum component L_y around the origin.

Integrating over some spatial volume we get

$$M^{\mu\nu} = \int \mathcal{M}^{\mu\nu 0}\, \tau dx dy d\eta \tag{5.50}$$

The familiar angular momentum operator (L_k) about any axis can be extracted from the components of this tensor, since

$$M^{\mu\nu} = \epsilon^{ijk} L_k \ , \tag{5.51}$$

here ϵ^{ijk} is the anti-symmetric Levi-Cevita symbol. The reference point chosen in (5.49) is the origin. In Fig. 5.7 we show L_y around $\eta = 0$ as a function of time τ for different impact parameters. To compute (5.50), in the η direction we have

done the integration from $\eta = -0.5$ to $\eta = 0.5$, while in the x and y directions we have integrated from -20 fm to 20 fm. We observe as expected, that L_y increases with impact parameter, and increases with time to a maximum value after which it relaxes to zero.

5.3.4 Particle Spectra

Finally we show some results for particles generated from this hydrodynamics code. The freeze out and particle generator developed by S. Rose were used in this section with $T_{f.o} = 120$ MeV and impact parameter $b = 6$ fm. In Fig. 5.8a and Fig. 5.8b we show the spectra and v_2 results for proton p. We see typical features like the "flow shoulder" reflecting radial flow. And in Fig. 5.8c and Fig. 5.8d we show the spectra and v_2 results for pion π^0.

In all of these plots we show the freeze-out with the equilibrium particle distribution only (ideal) and the full result using corrections to the particle distributions given by the shear and bulk stress [100]. And in the v_2 plots (Fig.5.8b and 5.8d) we can see the suppression of flow due to the viscous corrections just as we had observed on the hydro side in Fig. 5.6.

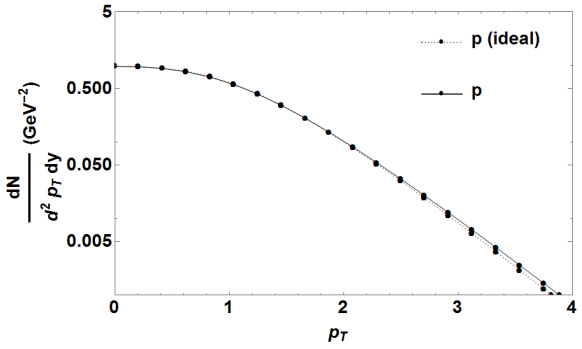

(a) Particle spectra for proton.

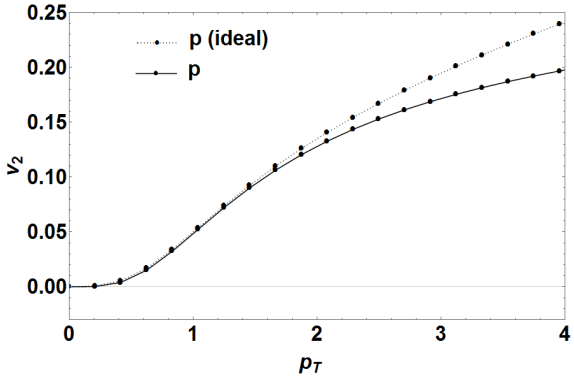

(b) v_2 for proton.

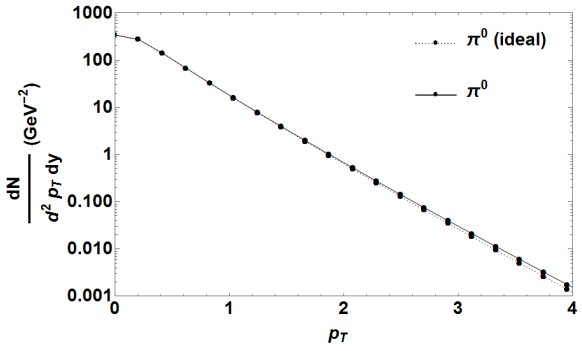

(c) Particle spectra for pion.

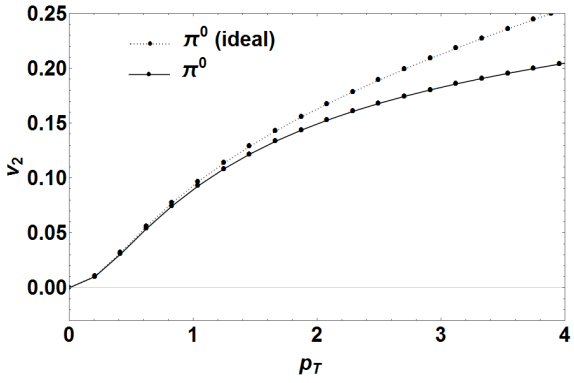

(d) v_2 for pion.

Figure 5.8: Figures (a) and (b) show the particle spectra and v_2 for proton and in figures (c) and (d) we see the particle spectra and v_2 for pion.

6. SUMMARY AND OUTLOOK

We have developed from bottom-up a shear and bulk viscous three dimensional hydrodynamics code. There are several hydro codes in the market but in many technical respects they are distinct to each other with different choices of algorithms and implementation details. We used a 5th order WENO scheme as a reconstruction scheme along with the KT algorithm. We saw a marked improvement in the stability and accuracy of our results for standard tests with the WENO scheme. For an accurate time integration we have used the total variation diminishing TVD-RK3 scheme, a variant of Runge-Kutta integration. We have run our code through a gamut of tests many of them with analytical results and we were able to match the results with high accuracy for non-trivial initial conditions. Gubser flow and its semi-analytical and analytical shear viscous tests are examples of such highly non-trivial tests. And we have run through these tests with stability and more importantly without any manual fixes.

Finally we ran our code with CGC based initial conditions with strong initial flows at early times, when the expansion is very high (proportional to $1/\tau$). Our CGC initial conditions, have very high corrections for shear and bulk stresses, which we have been able to run stably. We believe currently no other research group is dealing with such initial condition with large flows and large viscous corrections. We also discovered that the structure of viscous stresses coming from the CGC initial conditions are similar in shape and profile to their natural Navier-Stokes values, that can be calculated from the initial CGC flow. This was a surprising observation. We have also studied that behavior of angular momentum in our CGC hydro evolution, we observed that though it is not conserved globally it does relax to the "naive"

boost invariant case.

Our outlook for the future is

- Further investigation of the relation between CGC viscous corrections and Navier Stokes,
- Correcting large initial radial flow that needs taming by 3^{rd} order terms in the CGC initial conditions,
- Eventually tuning to data from RHIC and LHC,
- And finally looking at CGC beyond boost invariance and with fluctuations, which will be a definitive treatment of the angular momentum.

REFERENCES

[1] P. Huovinen and P. Petreczky. *Nuclear Physics A*, **837**(1):26–53, 2010.

[2] S. Ruester et al. *Physical Review D*, **72**(3):034004, 2005.

[3] B. Abelev et al. *Physical Review Letters*, **109**(25):252301, 2012.

[4] A. Adare et al. *Physical Review Letters*, **98**(16):162301, 2007.

[5] M. Heffner et al. *Journal of Physics G: Nuclear and Particle Physics*, **30**(8):S1043, 2004.

[6] G. Chen et al. *Physical Review C*, **92**(6):064912, 2015.

[7] G. Altarelli and G. Parisi. *Nuclear Physics B*, **126**(2):298–318, 1977.

[8] D. Politzer. *Physics Reports*, **14**(4):129–180, 1974.

[9] D. Gross and F. Wilczek. *Physical Review Letters*, **30**(26):1343, 1973.

[10] M. M. Aggarwal et al. *ArXiv Preprint ArXiv:1007.2613*, 2010.

[11] R. A. Lacey et al. *Physical Review Letters*, **98**(9):092301, 2007.

[12] E. O'Brien et al. *Nuclear Physics A*, **904**:264C, 2013.

[13] M. Alford et al. *Nuclear Physics B*, **537**(13):443 – 458, 1999.

[14] M. Alford et al. *Physics Letters B*, **422**(1):247–256, 1998.

[15] R. Rapp et al. *Annals of Physics*, **280**(1):35–99, 2000.

[16] J. Adams et al. *Nuclear Physics A*, **757**(1):102–183, 2005.

[17] K. Adcox et al. *Nuclear Physics A*, **757**(1):184–283, 2005.

[18] B. Abelev et al. *Journal of High Energy Physics*, **2015**(6):1–41, 2015.

[19] K. Aamodt et al. *Physical Review Letters*, **105**(25):252302, 2010.

[20] M. Gyulassy. In *Structure and Dynamics of Elementary Matter*, pages 159–182. Springer, 2004.

[21] M. Gyulassy and L. McLerran. *Nuclear Physics A*, **750**(1):30–63, 2005.

[22] B. Muller et al. *ArXiv Preprint ArXiv:1202.3233*, 2012.

[23] J. D. Bjorken. *Physical Review D*, **27**(1):140, 1983.

[24] L. P. Csernai et al. *Physical Review C*, **26**(1):149, 1982.

[25] D. H. Rischke et al. *Nuclear Physics A*, **595**(3):346–382, 1995.

[26] T. Hirano et al. *ArXiv Preprint Nucl-th/0011087*.

[27] P. F. Kolb et al. *Physical Review C*, **62**(5):054909, 2000.

[28] P. F. Kolb et al. *Physics Letters B*, **500**(3):232–240, 2001.

[29] D. Teaney et al. *ArXiv Preprint Nucl-th/0110037*, 2001.

[30] C. Nonaka et al. *The European Physical Journal C-Particles and Fields*, **17**(4):663–673, 2000.

[31] C. Nonaka and S. A. Bass. *Physical Review C*, **75**(1):014902, 2007.

[32] U. Heinz et al. *Physical Review C*, **73**(3):034904, 2006.

[33] A. K. Chaudhuri. *Physical Review C*, **74**(4):044904, 2006.

[34] R. Baier and P. Romatschke. *The European Physical Journal C*, **51**(3):677–687, 2007.

[35] A. Muronga. *Physical Review C*, **76**(1):014909, 2007.

[36] H. Song and U. Heinz. *Physical Review C*, **77**(6):064901, 2008.

[37] H. Petersen et al. *Physical Review C*, **78**(4):044901, 2008.

[38] E. Molnar et al. *The European Physical Journal C*, **65**(3-4):615–635, 2010.

[39] B. Schenke et al. *Physical Review C*, **82**(1):014903, 2010.

[40] B. Schenke et al. *Physical Review C*, **85**(2):024901, 2012.

[41] L. Pang et al. *Physical Review C*, **86**(2):024911, 2012.

[42] P. Bożek. *Physical Review C*, **85**(3):034901, 2012.

[43] C. Gale et al. *International Journal of Modern Physics A*, **28**(11):1340011, 2013.

[44] L. Del Zanna et al. *The European Physical Journal C*, **73**(8):1–26, 2013.

[45] Iu. Karpenko et al. *Computer Physics Communications*, **185**(11):3016–3027, 2014.

[46] C. Shen et al. *Computer Physics Communications*, **199**:61–85, 2016.

[47] R. D. Woods and D. S. Saxon. *Physical Review*, **95**(2):577, 1954.

[48] M. L. Miller et al. *ArXiv Preprint Nucl-ex/0701025*, 2007.

[49] E. Iancu et al. *Nuclear Physics A*, **692**(3):583–645, 2001.

[50] E. Ferreiro et al. *Nuclear Physics A*, **703**(1):489–538, 2002.

[51] R. J. Fries et al. *Nuclear Physics A*, **774**:861 – 864, 2006.

[52] R. J. Fries et al. *ArXiv Preprint Nucl-th/0604054*, 2006.

[53] D. Kharzeev et al. *Nuclear Physics A*, **730**(3):448–459, 2004.

[54] D. Kharzeev et al. *Nuclear Physics A*, **747**(2):609–629, 2005.

[55] B. Schenke et al. *Physical Review Letters*, **108**(25):252301, 2012.

[56] B. Schenke et al. *Physical Review C*, **86**(3):034908, 2012.

[57] F. Cooper and G. Frye. *Physical Review D*, **10**(1):186, 1974.

[58] M. Bleicher et al. *Journal of Physics G: Nuclear and Particle Physics*, **25**(9):1859, 1999.

[59] S. A. Bass et al. *Progress in Particle and Nuclear Physics*, **41**:255–369, 1998.

[60] C. Adler et al. *Physical Review Letters*, **90**(3):032301, 2003.

[61] R. Snellings et al. *Journal of Physics G: Nuclear and Particle Physics*, **38**(12):124013, 2011.

[62] K. Aamodt et al. *Physical Review Letters*, **107**(3):032301, 2011.

[63] R. H. Brown and R. Q. Twiss. *Nature*, **178**(4541):1046–1048, 1956.

[64] S. Chapman and U. Heinz. *Physics Letters B*, **340**(4):250–253, 1994.

[65] S. Chapman et al. *Physical Review Letters*, **74**(22):4400, 1995.

[66] U. Heinz. *Nuclear Physics A*, **610**:264–277, 1996.

[67] C. L. Navier. *Mémoires de lAcadémie Royale des Sciences de lInstitut de France*, **6**:389–440, 1823.

[68] G. Stokes. volume 9. Pitt Press, 1851.

[69] W. A. Hiscock and T. S. Olson. *Physics Letters A*, **141**(3):125–130, 1989.

[70] W. Israel and J. M. Stewart. *Annals of Physics*, **118**(2):341–372, 1979.

[71] L. Euler. *Opera Omnia II*, **12**:54, 1755.

[72] R. Baier et al. *Physical Review C*, **73**(6):064903, 2006.

[73] R. Baier et al. *Journal of High Energy Physics*, **2008**(04):100, 2008.

[74] J. P. Boris and D. L. Book. *Journal of Computational Physics*, **11**(1):38–69, 1973.

[75] A. Kurganov and E. Tadmor. *Journal of Computational Physics*, **160**(1):241–282, 2000.

[76] C. Shu. pages 325–432. Springer Berlin Heidelberg, 1998.

[77] V. Venugopal and S. S. Girimaji. *Communications in Computational Physics*, **17**(05):1127–1150, 2015.

[78] S. T. Zalesak. *Journal of Computational Physics*, **31**(3):335–362, 1979.

[79] B. Van Leer. *Journal of Computational Physics*, **14**(4):361–370, 1974.

[80] C. Shu and S. Osher. *Journal of Computational Physics*, **77**(2):439–471, 1988.

[81] S. Gottlieb and C. Shu. *Mathematics of Computation of the American Mathematical Society*, **67**(221):73–85, 1998.

[82] C. Shu. *SIAM Journal on Scientific and Statistical Computing*, **9**(6):1073–1084, 1988.

[83] B. Gough. Network Theory Ltd., 2009.

[84] J. D. Bjorken. *Physical Review D*, **27**(1):140, 1983.

[85] G. A. Sod. *Journal of Computational Physics*, **27**(1):1–31, 1978.

[86] V. Schneider et al. *Journal of Computational Physics*, **105**(1):92–107, 1993.

[87] W. Broniowski et al. *Computer Physics Communications*, **180**(1):69–83, 2009.

[88] Wolfram Research, Inc. Mathematica 10.3.

[89] S. S. Gubser. *Physical Review D*, **82**(8):085027, 2010.

[90] S. S. Gubser and A. Yarom. *Nuclear Physics B*, **846**(3):469–511, 2011.

[91] H. Marrochio et al. *Physical Review C*, **91**(1):014903, 2015.

[92] K. Morita et al. *Physical Review C*, **61**(3):034904, 2000.

[93] T. Hirano and K. Tsuda. *Physical Review C*, **66**(5):054905, 2002.

[94] G. Chen and R. J. Fries. *Physics Letters B*, **723**(4):417–421, 2013.

[95] R. J. Fries et al. *Physical Review C*, **79**(3):034904, 2009.

[96] L. McLerran and R. Venugopalan. *Physical Review D*, **49**(5):2233, 1994.

[97] L. McLerran and R. Venugopalan. *Physical Review D*, **49**(7):3352, 1994.

[98] C. Gale et al. *Physical Review Letters*, **110**(1):012302, 2013.

[99] A. Bazavov et al. *Physical Review D*, **80**(1):014504, 2009.

[100] K. Dusling et al. *Physical Review C*, **81**(3):034907, 2010.

[101] J. C. Collins et al. *Physical Review Letters*, **34**(21):1353, 1975.

[102] J. Y. Ollitrault. *Physical Review D*, **46**(1):229, 1992.

[103] C. Sasaki. *Nuclear Physics A*, **830**(1):649c–656c, 2009.

[104] H. Song and U. Heinz. *Journal of Physics G: Nuclear and Particle Physics*, **36**(6):064033, 2009.

[105] L. McLerran. *Acta Physica Polonica Series B*, **33**(10):2859–2866, 2002.

APPENDIX A

COORDINATE SYSTEM

A.1 Relations

We are working with the hyperbolic coordinates for our $(3+1)$ hydro code. The relations connecting the hyperbolic coordinates to the Minkowski coordinates are

$$\tau = \sqrt{t^2 - z^2} \tag{A.1}$$

$$\eta = \frac{1}{2}\log\frac{1+\frac{z}{t}}{1-\frac{z}{t}} = arctanh(\frac{z}{t}) \tag{A.2}$$

$$z = \tau\ sinh\eta \tag{A.3}$$

$$t = \tau\ cosh\eta \tag{A.4}$$

A.2 Metric

For the Minkowski space we know the metric $g_{\mu\nu}$ must satisfy

$$g_{\mu\nu}x^\mu x^\nu = 0. \tag{A.5}$$

so that the space-time interval is independent of the choice of inertial frame. The form of metric we are using for this thesis is

$$\begin{bmatrix} 1 & 0 & 0 & 0 \\ 0 & -1 & 0 & 0 \\ 0 & 0 & -1 & 0 \\ 0 & 0 & 0 & -1 \end{bmatrix} \tag{A.6}$$

However, we are mostly working in the hyperbolic coordinates $\{\tau, x, y, \eta\}$, to which we can arrive from transformation on the Minkowski coordinates $\{t, x, y, z\}$.

The Jacobian for transformation from $x^\mu = \{t, x, y, z\}$ to $\widetilde{x}^\mu = \{\tau, x, y, \eta\}$

$$\mathcal{J}^\mu_{\ \nu} = \frac{d\widetilde{x}^\mu}{dx^\nu} = \begin{bmatrix} \frac{\partial\tau}{\partial t} & 0 & 0 & \frac{\partial\tau}{\partial z} \\ 0 & 1 & 0 & 0 \\ 0 & 0 & 1 & 0 \\ \frac{\partial\eta}{\partial t} & 0 & 0 & \frac{\partial\eta}{\partial z} \end{bmatrix} = \begin{bmatrix} \frac{t}{\tau} & 0 & 0 & \frac{-z}{\tau} \\ 0 & 1 & 0 & 0 \\ 0 & 0 & 1 & 0 \\ \frac{-z}{\tau^2} & 0 & 0 & \frac{t}{\tau^2} \end{bmatrix} = \begin{bmatrix} \cosh(\eta) & 0 & 0 & -\sinh(\eta) \\ 0 & 1 & 0 & 0 \\ 0 & 0 & 1 & 0 \\ \frac{-\sinh(\eta)}{\tau} & 0 & 0 & \frac{\cosh(\eta)}{\tau} \end{bmatrix} \tag{A.7}$$

Now derivation of metric $\widetilde{g}_{\mu\nu}$ is straight forward.

$$\begin{bmatrix} dt & dx & dy & dz \end{bmatrix} \begin{bmatrix} 1 & 0 & 0 & 0 \\ 0 & -1 & 0 & 0 \\ 0 & 0 & -1 & 0 \\ 0 & 0 & 0 & -1 \end{bmatrix} \begin{bmatrix} dt \\ dx \\ dy \\ dz \end{bmatrix} = 0 \tag{A.8}$$

$$\equiv \begin{bmatrix} \partial\tau & \partial x & \partial y & \partial\eta \end{bmatrix} \mathcal{J}^\mu_{\ \nu}{}^T \begin{bmatrix} 1 & 0 & 0 & 0 \\ 0 & -1 & 0 & 0 \\ 0 & 0 & -1 & 0 \\ 0 & 0 & 0 & -1 \end{bmatrix} \mathcal{J}^\mu_{\ \nu} \begin{bmatrix} \partial\tau \\ \partial x \\ \partial y \\ \partial\eta \end{bmatrix}$$

Hence, we arrive at

$$\widetilde{g}_{\mu\nu} = \mathcal{J}^{\alpha}_{\ \mu}\, \mathcal{J}^{\beta}_{\ \nu}\, g_{\alpha\beta} \tag{A.9}$$

And more explicitly this is

$$\widetilde{g}_{\mu\nu} = \begin{bmatrix} 1 & 0 & 0 & 0 \\ 0 & -1 & 0 & 0 \\ 0 & 0 & -1 & 0 \\ 0 & 0 & 0 & -\tau^2 \end{bmatrix} \tag{A.10}$$

The differential length element can be written as

$$ds^2 = d\tau^2 - dx^2 - dy^2 - \tau^2 d\eta^2 \tag{A.11}$$

A.3 Covariant Derivatives and Geometrical Terms

While simplifying equations in chapter 2 we encountered covaraiant derivatives. These covariant derivatives introduce geometrical terms. While evaluating some of these terms let's keep in mind that for the metric $\widetilde{g}_{\mu\nu}$, only non-zero christoffel symbols are

$$\Gamma^{\eta}_{\eta\tau} = \Gamma^{\eta}_{\tau\eta} = \frac{1}{\tau} \tag{A.12a}$$

$$\Gamma^{\tau}_{\eta\eta} = \tau \tag{A.12b}$$

A.3.1 Expansion $\partial_{;\rho} u^{\rho}$

The expansion of fluid in hyperbolic coordinates is given by

$$\partial_{;\rho} u^{\rho} = \partial_{\rho} u^{\rho} + \Gamma^{\rho}_{\rho d} u^{d} \equiv \partial_{\rho} u^{\rho} + \frac{1}{\tau} u^{0} \tag{A.13}$$

A.3.2 Source Terms for $\partial_{;\mu} T^{\mu\nu}$

$$\partial_{;\mu} T^{\mu\nu} = \partial_{\mu} T^{\mu\nu} + S^{\nu} \tag{A.14}$$

Here s^{ν} comes from the covariant derivative and is given by

$$S^{\nu} = \Gamma^{\rho}_{\rho d}\, T^{d\nu} + \Gamma^{\nu}_{\rho d}\, T^{\rho d} \tag{A.15}$$

which we can work out to arrive at

$$S^{\nu} = \begin{bmatrix} \frac{T^{\tau\tau} + \tau^2 T^{\eta\eta}}{\tau} \\ \frac{T^{x\tau}}{\tau} \\ \frac{T^{y\tau}}{\tau} \\ \frac{3T^{\eta\tau}}{\tau} \end{bmatrix} \tag{A.16}$$

A.3.3 Geometrical Term $G^{\mu\nu}$

$G^{\mu\nu}$ is the geometric term which comes from contraction of four velocity u^{ρ} with the three index $\partial_{;\rho}\pi^{\mu\nu}$. That is

$$u^{\rho}\partial_{;\rho}\pi^{\mu\nu} = u^{\rho}\partial_{\rho}\pi^{\mu\nu} + G^{\mu\nu} \tag{A.17}$$

$$G^{\mu\nu} = u^{\rho}\Gamma^{\mu}_{\rho d}\, \pi^{d\nu} + u^{\rho}\Gamma^{\nu}_{\rho d}\, \pi^{\mu d} \tag{A.18}$$

On simplifying using the Christoffel symbols we get

$$G^{\mu\nu} = \begin{bmatrix} 2\pi^{\tau\eta}u^{\eta}\tau & \pi^{x\eta}u^{\eta}\tau & \pi^{y\eta}u^{\eta}\tau & \frac{\pi^{\tau\tau}u^{\eta}+\pi^{\tau\eta}u^{\tau}+\tau^2 u^{\eta}\pi^{\eta\eta}}{\tau} \\ \pi^{x\eta}u^{\eta}\tau & 0 & 0 & \frac{\pi^{x\eta}u^{\tau}+\pi^{\tau x}u^{\eta}}{\tau} \\ \pi^{y\eta}u^{\eta}\tau & 0 & 0 & \frac{\pi^{y\eta}u^{\tau}+\pi^{\tau y}u^{\eta}}{\tau} \\ \frac{\pi^{\tau\tau}u^{\eta}+\pi^{\tau\eta}u^{\tau}+\tau^2 u^{\eta}\pi^{\eta\eta}}{\tau} & \frac{\pi^{x\eta}u^{\tau}+\pi^{\tau x}u^{\eta}}{\tau} & \frac{\pi^{y\eta}u^{\tau}+\pi^{\tau y}u^{\eta}}{\tau} & \frac{2(\pi^{\eta\eta}u^{\tau}+\pi^{\tau\eta}u^{\eta})}{\tau} \end{bmatrix} \tag{A.19}$$

- $\partial_{;\rho}u^{\beta} = \partial_{\rho}u^{\beta} + \Gamma^{\beta}_{\rho d}u^{d}$
- $\partial_{;\rho}u_{\beta} = \partial_{\rho}u_{\beta} - \Gamma^{d}_{\rho\beta}u^{d}$
- $\sigma^{\mu\nu} = \Delta^{\mu\nu\alpha\beta}\,\partial_{;\alpha}u_{\beta} \equiv \Delta^{\mu\nu\alpha\beta}\,(\partial_{\alpha}u_{\beta} - \Gamma^{d}_{\beta\alpha}\,u_{d})$
- $Du_{\beta} = u^{\rho}\partial_{;\rho}u_{\beta} \equiv u^{\rho}(\partial_{\rho}u_{\beta} - \Gamma^{d}_{\beta\rho}\,u_{d})$
- $Dg_{\alpha\beta} = u^{\rho}\partial_{;\rho}g_{\alpha\beta} \equiv u^{\rho}(\partial_{\rho}g_{\alpha\beta} - \Gamma^{d}_{\rho\alpha}\,g_{d\beta} - \Gamma^{d}_{\rho\beta}\,g_{\alpha d})$

A.3.4 Four Velocity

Here we will establish the relationship between four velocity in the Minkowski coordinates $\{t, x, y, z\}$ to the hyperbolic coordinates $\{\tau, x, y, \eta\}$. Starting with

$$u^{\mu} = \{\gamma, \gamma\, v_x, \gamma\, v_y, \gamma\, v_z\}, \tag{A.20}$$

$$\gamma = \frac{1}{\sqrt{1 - v_x^2 - v_y^2 - v_z^2}} \tag{A.21}$$

For transforming to hyperbolic coordinates

$$\tilde{u}^{\mu} = \mathcal{J}^{\mu}_{\ \nu}\, u^{\nu} \tag{A.22}$$

is to be computed. The result is

$$\tilde{u}^{\mu} = \mathcal{J}^{\mu}_{\ \nu}\, u^{\nu} \tag{A.23}$$

which on calculation gives

$$\tilde{u}^{\mu} = \left\{ \ (\cosh(\eta) - v_z \sinh(\eta)), \ \ \gamma v_x, \ \ \gamma v_y, \ \ \frac{(v_z \cosh(\eta) - \sinh(\eta)) \ \ \gamma}{\tau} \ \right\} \tag{A.24}$$

Comparing this result with a general structure of four velocity in hyperbolic coordinates

$$u^{\mu} = \{\tilde{\gamma}, \tilde{\gamma}\ \tilde{v}_x, \tilde{\gamma}\ \tilde{v}_y, \tilde{\gamma}\ \tilde{v}_\eta\}, \tag{A.25}$$

$$\tilde{\gamma} = \frac{1}{\sqrt{1 - \tilde{v}_x^2 - \tilde{v}_y^2 - \tau^2 \tilde{v}_\eta^2}} \tag{A.26}$$

we can derive

$$\tilde{\gamma} = \gamma(\cosh(\eta)) - v_z \sinh(\eta) \tag{A.27}$$

$$\tilde{v}_x = \frac{v_x}{\cosh(\eta) - v_z \sinh(\eta)} \tag{A.28}$$

$$\tilde{v}_y = \frac{v_y}{\cosh(\eta) - v_z \sinh(\eta)} \tag{A.29}$$

$$\tilde{v}_\eta = \frac{v_z - \tanh(\eta)}{\tau(1 - v_z \tanh(\eta))} \tag{A.30}$$

Notice that in the case of boost invariance when we have $v_z = \tanh(\eta)$, it turns out $\tilde{v}_\eta = 0$, this is the primary reason we do hydro simulation in hyperbolic coordinates. Finally our results are from hydro are in the hyperbolic coordinate so it would be

convenient to get the reverse relationship

$$\gamma = \frac{\cosh(\eta) + \tilde{v}_\eta \tau \sinh(\eta)}{1 - \tilde{v}_x^2 - \tilde{v}_y^2 - \tau^2 \tilde{v}_\eta^2} \tag{A.31}$$

$$v_x = \frac{\tilde{v}_x}{\cosh(\eta) + \tau\ \tilde{v}_\eta \sinh(\eta)} \tag{A.32}$$

$$v_y = \frac{\tilde{v}_y}{\cosh(\eta) + \tau\ \tilde{v}_\eta \sinh(\eta)} \tag{A.33}$$

$$v_z = \frac{\tau\ \tilde{v}_\eta + \tanh(\eta)}{(1 + \tau\ \tilde{v}_\eta \tanh(\eta))} \tag{A.34}$$

And finally if we run the hydro simulation at only mid-rapidity ($\eta = 0$) then the relation between flow in the two coordinate systems is

$$\{v_x, v_y, v_z\} = \{\tilde{v}_x, \tilde{v}_y, \tau\ \tilde{v}_\eta\} \tag{A.35}$$